IEEE ComSoc IEEE Communications Society
IEEE Open Journal of the Communications Society

Received 15 May 2024; revised 20 June 2024; accepted 22 July 2024. Date of publication 25 July 2024; date of current version 5 August 2024.

Digital Object Identifier 10.1109/OJCOMS.2024.3433502

A Tutorial on Chirp Spread Spectrum Modulation for LoRaWAN: Basics and Key Advances

ALIREZA MALEKI [1], HA H. NGUYEN [1], EBRAHIM BEDEER [1] (Member, IEEE), AND ROBERT BARTON [2]

[1] Department of Electrical and Computer Engineering, University of Saskatchewan, Saskatoon, SK S7N 5A9, Canada

[2] Cisco Systems Inc., Toronto, BC V7X 1A0, Canada

CORRESPONDING AUTHOR: A. MALEKI (e-mail: alireza.maleki@usask.ca)

This work was supported in part by the Cisco Systems Inc., and in part by the Natural Sciences and Engineering Research Council (NSERC) of Canada.

ABSTRACT Chirp spread spectrum (CSS) signal is the heart of long-range (LoRa) modulation, also known as CSS modulation, and is used in long-range wide area network (LoRaWAN) in Internet of things (IoT) scenarios. CSS modulation has drawn much attention from the research and industry communities in recent years. However, to the best of our knowledge, a comprehensive tutorial, investigating the mathematical foundations of CSS modulation in the LoRaWAN application, is missing in the literature. Therefore, in the first part of this paper, we provide a thorough analysis and tutorial of CSS modulation as the physical (PHY) layer of LoRaWAN, discussing various aspects such as signal generation, detection, error performance, and spectral characteristics. Moreover, a summary of key recent advances in the context of CSS modulation modifications and applications in IoT networks is presented in the second part of this paper under four main categories, i.e., transceiver configuration and design, data rate improvement, interference modeling, and synchronization algorithms. Finally, future research directions are also provided to discuss the potential issues and solutions for improving the performance of CSS modulation in LoRaWAN.

INDEX TERMS Chirp spread spectrum (CSS), Internet of Things (IoT), long-range wide area network (LoRaWAN), low-power wide area network (LPWAN), spreading factor (SF).

I. INTRODUCTION

THE INTERNET of things (IoT) has emerged as a groundbreaking technology that enables intelligent sensing and actuation for a wide range of objects. By facilitating information exchange with a core network, IoT empowers individuals and software agents to remotely manage and monitor device behavior from systems located hundreds of kilometers away via the application layer. Its applications include smart homes, intelligent transportation, smart hospitals, and smart cities [1], [2], [3]. These emerging applications lead to the rapid growth of IoT network sizes which results in massive IoT networks. The IoT causes a significant transformation in business and consumer culture and ignites a new industrial revolution, with over 20 billion connected devices in 2020 [1]. More devices or objects were connected to the Internet in 2009 than there were people. Despite the wide variations in the IoT market volume predictions made by various analysts and consulting firms, all of them concur that the market is enormous and expanding quickly. By 2025, there will be more than 30 billion active IoT devices, excluding smartphones, according to IoT Analytics [4]. With a compound annual growth rate (CAGR) of 25.4%, the IoT industry is predicted to increase from 381.3 billion USD in 2021 to 1, 854.76 billion USD in 2028 [5].

The proliferation of IoT devices and the increasing demands for connectivity necessitate addressing several challenges in developing efficient IoT systems. As the number of devices continues to surge, the ability to manage and maintain seamless connectivity becomes crucial. Additionally, meeting the diverse requirements of different applications within the IoT ecosystem poses a significant challenge. The design and implementation of intelligent, adaptable, energy-efficient, and cost-effective systems that can handle massive data transmissions, which are not delay sensitive, and ensure reliable communication in the face of scalability

constraints is a complex task. To address these needs, low-power wide area network (LPWAN) technology has emerged as the favored connectivity option for IoT networks due to its extensive communication range, energy efficiency, and cost-effectiveness. It is particularly suitable for delay-tolerant applications with limited device throughput, making it an ideal choice for low-power battery-operated devices. LPWAN protocols include modulations such as differential phase-shift keying (DPSK) in SigFox, $\frac{\pi}{2}$-binary PSK ($\frac{\pi}{2}$-BPSK) and $\frac{\pi}{2}$-quadrature PSK ($\frac{\pi}{2}$-QPSK) in narrowband-IoT (NB-IoT), BPSK, QPSK, 16 and 64 quadrature amplitude modulation (QAM) in long-term evolution for machines (LTE-M), and long-range (LoRa) modulation, also known as chirp spread spectrum (CSS) modulation, in LoRaWAN to ensure robust transmission over long distances by tolerating interference and noise [2].

Among all LPWAN technologies, the main characteristics of long-range communication, low-power consumption, and resistance to interference or simultaneous transmission collisions of LoRaWAN have made it highly regarded for creating a wide range of IoT applications such as space-to-ground communications, localization systems, smart buildings, and environmental monitoring [2]. LoRaWAN functions as a media access control (MAC) layer protocol that operates over CSS modulation. Serving as a software layer, it governs the utilization of LoRa hardware by devices, dictating actions such as transmission and message formatting [6]. By using the terminology of LoRaWAN medium access control (MAC) and LoRaWAN physical (PHY) layers, here in this tutorial, our full focus is on CSS modulation as the core of LoRaWAN PHY [7]. Due to the extensive surveys existing in the literature on LoRaWAN MAC [2], [3], [8], [9], [10], we briefly discuss the LoRaWAN MAC main features such as channel allocation, device classes, and regions of operations in the following subsection, leaving the details out of the scope of this tutorial.

A. LORAWAN MEDIUM ACCESS CONTROL (MAC) LAYER

Since technologies based on LoRa have to be very energy efficient, LoRaWAN MAC tries to avoid overhead in signaling as much as possible since it can cost more energy and latency. Consequently, the channel allocation strategy of LoRaWAN is very simple adopting ALOHA-based protocol with additional acknowledgment (ACK) mechanisms so end-devices (EDs) do not need to peer with specific gateways [11].

LoRaWAN has three main classes of transmitter EDs, i.e., Class A, Class B, and Class C. All the protocols specified for Class A are mandatory and should be implemented in all LoRa devices [11]. The downlink (DL) is controlled by the ED in Class A, and after each uplink (UL) transmission, only two DL receive windows will become active. Any packets sent from the gateway (GW) to the node must wait for the next UL message. As a result, Class A EDs consume the least amount of energy. The battery consumption is efficient with DL control in Class B EDs as they operate with slotted communication synchronized with beacon frames. Regarding Class C EDs, it should be noted that they are the least efficient in energy consumption as a typical Class C ED receiving window is always open except during the transmission period. However, this results in lower DL latency compared to Class A and B EDs.

Finally, the operating frequency band of LoRaWAN devices is selected based on the region of operation and its defined frequency band in [12]. Accordingly, 12 frequency channel plans for LoRaWAN communications are summarized in Table 1.

B. LORAWAN PHYSICAL (PHY) LAYER

At the PHY layer, LoRaWAN exploits a proprietary modulation, i.e., CSS modulation. The CSS modulation technique is patented [13] and has lacked a theoretical description until the publication of the work [7]. The patent referenced does not delve into specifics regarding equations and signal processing. For LoRaWAN, CSS modulation is essential to enable its standout characteristics of long-range communication and low power consumption. Through the use of a broad frequency spectrum, CSS enables long-distance communication between LoRaWAN devices with low signal deterioration and strong interference resistance. This resilience is crucial in urban settings when several devices are in use at the same time. Additionally, CSS facilitates scalable network installations by permitting multiple devices to interact with minimal cross-talk by efficiently distinguishing signals using various spreading factors. Additionally, CSS enables LoRaWAN's adaptive data rate (ADR) mechanisms, which balance performance, battery consumption, and range by altering data rates based on network conditions and signal quality. Because of its efficiency, IoT devices' batteries last longer, allowing for long-term deployments. Furthermore, signal propagation guarantees regulatory power density compliance of LoRaWAN communications. Overall, LoRaWAN's key advantages–reliability, scalability, and appropriateness for low-power, wide-area IoT applications–are supported by CSS.

While the work of [14] offers a broad overview of CSS modulation and presents some fundamental equations, it relies on the reader's intuition for decoding. The works of [15], [16] provide more detailed insights into the signal, modulation, and demodulation aspects. Yet, they also lack a mathematical foundation rooted in signal theory for these processes, partly due to their focus on the analog domain. Vangelista presented the first complete mathematically rigorous description of CSS modulation in [7]. Since its publication, [7] has served as the foundation for numerous research works conducted in academia and industry, focusing on this modulation type. For the rest of this tutorial, with a full focus on LoRaWAN PHY, we aim to provide a comprehensive mathematical foundation for CSS modulation, its characteristics, and recent key works in the literature modifying CSS modulation to benefit LoRaWAN communication performance.

TABLE 1. Regional operating frequency channels for LoRa communications [12].

Channel Plan	Common Name	Region
EU863-870	EU868	For any region where the radio spectrum use is defined by the European telecommunications standards institute (ETSI) [EN300.220] standard
US902-928	US915	For the USA, Canada, and all other countries in international telecommunication union (ITU) Region 2 adopting the entire federal communications commission (FCC) code of federal regulations (CFR) Part 15 regulations in $902-928$ MHz industrial, scientific, and medical (ISM) band
CN779-787	CN779	For China $779-787$ MHz band
EU443	EU443	For the $433.05-434.79$ MHz ISM band in ITU Region 1 (Europe, Africa, the Commonwealth of Independent States, Mongolia, and the Middle East west of the Persian Gulf, including Iraq)
AU915-928	AU915	For Australia and all other countries whose band extends from 915 to 928 MHz spectrum
CN470-510	CN470	For China $470-510$ MHz band
AS923-1	AS923	For countries having available frequencies in the $915-928$ MHz range with common channels in the $923-923.5$ MHz sub-band
AS923-2	AS923	For countries having available frequencies in the $915-928$ MHz range with common channels in the $921.4-922$ MHz sub-band
AS923-3	AS923	For countries having available frequencies in the $915-928$ MHz range with common channels in the $916.5-917$ MHz sub-band
KR920-923	KR920	For South Korea radio-frequency identification (RFID) and ubiquitous sensor network (USN) frequency band defined by the Korean Government, which has allocated LPWA-based IoT networks the channel center frequencies from 920.9 to 923.3 MHz.
IN865-867	IN865	For India $865-867$ MHz frequency band
RU864-870	RU864	For Russia $864-870$ MHz frequency band

As mentioned, there are multiple comprehensive surveys on LoRaWAN in the literature [2], [3], [8], [9], [10]. However, these works are comprehensive investigations of the LoRa/LoRaWAN mechanism and barely include any equations for providing insights into the mathematical foundation of CSS modulation, which is the main objective of this tutorial paper. Apart from the existing surveys on LoRaWAN, several works in the literature focus on one aspect of CSS modulation. For example, the work in [7] discusses the CSS modulation and its error performance, the work in [18] deals with the spectral characteristics of CSS modulation, and most recently, the work in [22] surveys existing CSS waveform designs with the aim of data rate improvement. That said, our paper can be considered as the first mathematically-supported tutorial on CSS modulation along with a discussion on the recent key advances of the subject. A comparison between the existing works and the presented paper is provided in Table 2. As can be seen, there is a lack of work in the existing literature that covers all important aspects of CSS modulation along with an investigation of key recent works. To address this issue, the followings are presented as the main contributions of this paper:

1) There are multiple surveys on LoRaWAN MAC characteristics and features in the literature [2], [3], [8], [9], [10]. As mentioned, the present work focuses only on CSS modulation and provides a mathematically-supported tutorial on how the CSS technique is modified and used in different LoRaWAN communication scenarios as there is no such work existing in the literature to the authors' best knowledge.
2) We shed light on the basic foundations of this modulation and its signal-generation procedures. Also, we discuss the analytical process of the corresponding signal detection at the receiver exploring the dechirping operation. Additionally, we evaluate the analytical expressions provided in the literature for the error performance of CSS modulation in the presence of noise and fading channels. Moreover, detailed power spectral characteristics of CSS waveforms are presented. Also, a mathematical-based orthogonality analysis of CSS signals is provided.
3) We provide a detailed analysis of the state-of-the-art research works that focus on CSS modulation by dividing them into four main categories, i.e., transceiver configuration and design, data rate improvements, interference modeling, and synchronization algorithms.
4) We provide future research directions on improving the performance of CSS modulation in the presence of the Doppler effect in mobile scenarios and in the presence of interference resulting from coexistence with other wireless technologies.

TABLE 2. Summary of recent works focusing on CSS modulation and LoRaWAN.

Article	Error performance	Interference	Spectral characteristics	Synchronization	Data rate improvement	Comprehensive Discussion on LoRa/LoRaWAN
Sinha *et al.* [8]	–	–	–	–	–	✓
Sun *et al.* [9]	–	–	–	–	–	✓
Jouhari *et al.* [2]	–	–	–	–	–	✓
Pagano *et al.* [10]	–	–	–	–	–	✓
Milarokostas *et al.* [3]	–	–	–	–	–	✓
Vangelista [7]	✓	–	–	–	–	–
Passolini [17]	✓	–	–	–	–	–
Chiani *et al.* [18]	–	–	✓	–	–	–
Elshabrawy *et al.* [19]	✓	✓	–	–	–	–
Benkhelifa *et al.* [20]	✓	✓	–	–	–	–
Nguyen *et al.* [21]	✓	–	–	–	–	–
Azim *et al.* [22]	✓	–	–	–	✓	–
Presented paper	✓	✓	✓	✓	✓	–

To the best of our knowledge, this work is the first one focusing on providing a tutorial on CSS modulation and discussing the recent key advances of the subject in IoT networks. We hope the tutorial serves as a solid foundation for future researchers in the context of this transmission technique providing an integrated CSS signal introduction discussing the most relevant research topics.

Terminology: In the literature, CSS modulation patented in [13] which is the main focus of this paper, is being referred to with various terminology. Here in the following, to clarify the terminology used in this tutorial paper, we provide the most used terminologies throughout the literature:

- Chirp: A sinusoidal signal whose frequency varies with time linearly.
- CSS: A spread spectrum technique that uses wideband linear frequency modulated chirp pulses to encode information.
- Chirp modulation: A digital communication modulation technique in which the slope of the chirp is the information-bearing element, e.g., positive slope represents binary one, and negative slope represents binary zero [23]. It is also known as slope shift keying (SSK) and frequency-modulated (FM) chirp [24].
- CSS modulation: A patented modulation [13] that embeds the information data in the starting frequency of a chirp [21]. It is also known as LoRa modulation [25], frequency shift chirp modulation [7], and frequency shift CSS (FSCSS) [26].

Accordingly, throughout this paper, we use the terms "CSS modulation" and "LoRa modulation" interchangeably.

For the convenience of the readers, Table 3 is provided to contain all acronyms used in this paper. In the remainder of this paper, we present an analytical representation of CSS modulation basics along with a categorization of the key advances related to this modulation in LoRaWAN-based IoT scenarios in Section II. Recent key advances in transceiver configuration and design of CSS transmission systems are investigated in Section III. Key recent research works with the aim of data rate improvement of CSS modulation are discussed in Section IV. In Section V, the key works related to interference modeling of a CSS communication system are analyzed. Section VI contains the discussion on CSS systems synchronization and the operations performed on the received CSS signals to recover time and frequency offsets. Future research directions are provided in Section VII and the paper is concluded in Section VIII. The outline of the paper is illustrated in Figure 1.

II. CSS MODULATION: BASIC MATHEMATICAL CONCEPTS

In this section, we provide a background on chirp signals followed by a detailed analysis of CSS modulation basic concepts. First, we will discuss the background of the chirp signal and its applications in radar systems and early digital communication schemes. Then, we introduce an end-to-end communication system for which the CSS modulation is the main core. By going through the transmitter, the procedure of modulating data bit sequences into the CSS signal is investigated analytically. Then, on the receiver side, the unique implementation of CSS signal detection is presented as the result of deriving the optimum detector. The error performance of CSS modulation in noise and fading channels is provided via analytical expressions and simulation results. Finally, the spectral characteristics of CSS signal waveform and the orthogonality conditions between different CSS modulation chirps are investigated.

A. CHIRP BACKGROUND

While the focus of this paper is on CSS modulation application in LoRaWAN, it is worth noting that chirp signals have originally found applications in military radar/radar [27], [28], [29]. Additionally, chirp signals when integrated with slope shift keying (SSK) modulation, found applications in other communication systems such as high

TABLE 3. Acronyms used in this paper.

Acronym	Description	Acronym	Description
AWGN	Additive white Gaussian noise	IoT	Internet of things
AF	Ambiguity function	LoRaWAN	Long-range wide area network
ADC	Analog-to-digital converter	LUT	Look-up table
ACS	Asymmetry chirp signal	LEO	Low Earth orbit
BPSK	Binray phase-shift keying	LPWAN	Low power wide area network
BER	Bit error rate	MF	Matched filter
CFO	Carrier frequency offset	ML	Maximum likelihood
CSI	Channel state information	MPC	Multi-path channel
CSS	Chirp spread spectrum	MAI	Multiple access interference
CAGR	Compound annual growth rate	MIMO	Multiple-input multiple-output
CDF	Cumulative distribution function	OCG	Orthogonal chirp generator
DCSS	Differential CSS	OFDM	Orthogonal frequency-division multiplexing
DDS	Direct digital synthesis	PLL	Phase-locked loop
DCRK-CSS	Discrete chirp rate keying CSS	PSK-LoRa	Phase-shift keying LoRa
DFT	Discrete Fourier transform	SFO	Sampling frequency offset
DFS	Doppler frequency shift	STO	Sampling time offset
EICS-LoRa	Enhanced ICS-LoRa	SIR	Signal-to-interference ratio
ePSK-LoRa	Enhanced PSK-LoRa	SSK-LoRa	Slope-shift keying LoRa
FFT	Fast Fourier transform	SDR	Software-defined radio
FCW	Folded chirp waveform	STBC	Space-time block coding
FCrSK	Folded chirp-rate shift keying	SE	Spectral efficiency
FPAR	Frequency peak average rate	SF	Spreading factor
FSCSS	frequency shift chirp spread spectrum	SFD	Start frame delimiter
FBI-LoRa	Frequency-bin-index LoRa	SIC	Successive interference cancellation
FSK	Frequency-shift keying	SER	Symbol error rate
FF	Fundamental frequencies	SCS	Symmetry chirp signal
IM	Index modulation	SC-MCR	Symmetry chirp with multiple chirp rates
IQCIM	In-phase and quadrature chirp index modulation	TDM-LoRa	Time domain multiplexed LoRa
IQCSS	In-phase and quadrature CSS	TDM SC-MCR	Time domain multiplexed SC-MCR
ICS-LoRa	Interleaved chirp spreading LoRa	WSS	Wide-sense stationary

frequency (HF) data transmission [30]. Therefore, a discussion of the early applications of chirp signals is given below before investigating CSS modulation.

Chirp refers to a sinusoidal signal whose frequency varies with time. For the case in which this variation is linear, the chirp is called a linear chirp. Such signals (also called linear frequency modulated) have been extensively used in military radar/radar systems [27], [28], [29]. The advantages of chirp radar compared to the conventional pulse radar include improvements in range, range resolution, the ability to achieve similar performance with lower peak input power, increased resistance to noise, lower power supply voltage requirements, and a radar architecture that offers somewhat better resistance to jamming.

In addition to wide applications in radar systems, chirp signals found their way to digital communication through integration with SSK as the linear frequency modulation (LFM) scheme [24], [31]. Several researchers have suggested the use of chirp signals to represent binary data by assigning positive and negative dispersive slopes for ones and zeros [32], [33], [34]. For example, consider that the sinusoidal signal frequency increases linearly with time as illustrated in Figure 2(a). This results in a positive frequency-time slope referred to as an up-chirp. On the other hand, if the frequency decreases with time, the slope has a negative sign resulting in a down-chirp as in Figure 2(b). That said, in binary SSK, the up-chirp and the down-chirp represent binary 1 and binary 0, respectively. Moreover, various applications, including high-frequency (HF) data transmission [30] and air-to-ground communication via satellites [35], [36], have been investigated and performance evaluations of linear FM modulation are discussed extensively in comparison with other binary modulations in the literature, e.g., see [23], [37], [38]. All these works show the inherent ability to reject interference making this modulation scheme suitable for spread spectrum communication systems [39].

Although the use of chirp signals for transmission purposes in digital communication systems has existed since the early 20th century and is not proprietary, CSS modulation, on the other hand, is patented [13] and later, became a Semtech corporation proprietary modulation [21] in which the information-bearing element is the frequency shift of the chirp signal. This modulation is the main focus of our tutorial paper and is discussed in detail in the following sections.

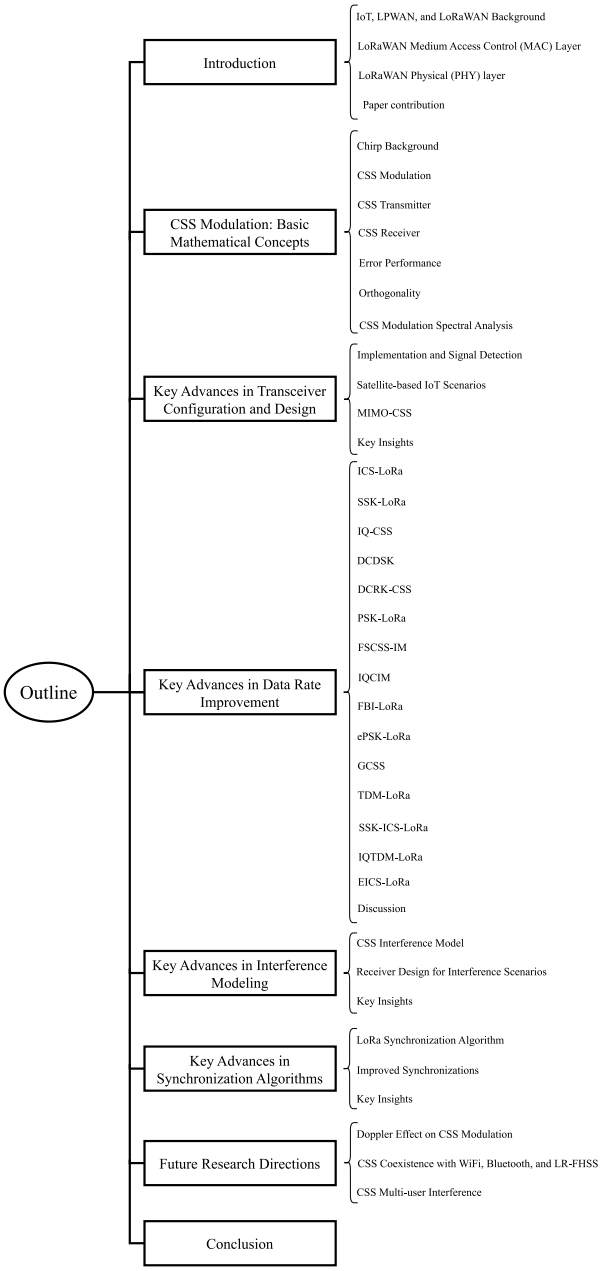

FIGURE 1. Outline of the paper.

B. CSS MODULATION

We consider CSS modulation as a set of M orthogonal chirps, each is used to modulate a binary data sequence of the length equal to the spreading factor (SF). Therefore, we have $M = 2^{\mathrm{SF}}$. The CSS modulation embeds each information data symbol (decimal equivalent of the binary data sequence of the length SF) into the aforementioned chirp signal in which the signal frequency increases (up-chirp) or decreases (down-chirp) with time over the bandwidth (BW). The main feature of this up-chirp is that when the symbol frequency reaches its maximum (minimum in down-chirp), it will wrap over and start from the minimum frequency (maximum in down-chirp) and keep on sweeping until it sweeps the BW

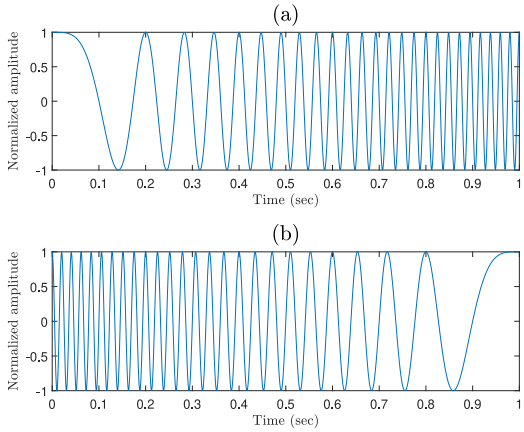

FIGURE 2. Time domain illustration of (a) up-chirp sinusoidal and (b) down-chirp sinusoidal signals.

once. Note that hereinafter, by chirp, LoRa, and CSS signals, we refer to up-chirp unless otherwise stated. Figure 3 is presented to illustrate an end-to-end communication system with CSS modulation. In the following parts of this section, we will go through each block of the CSS transmitter and receiver supported by mathematical equations and intuitive discussion on how the modulation works. However, before going through the CSS modulation, a detailed analytical discussion on the CSS signal waveform is provided next.

The CSS signal is a constant amplitude complex sinusoidal signal with a time-varying phase. This time-varying phase is expressed as [18]:

$$\phi(t) = 2\pi \int_{t_0}^{t} f(\rho)\mathrm{d}\rho + \phi_0, \quad t_0 \le t \le t_0 + T_{\mathrm{sym}}, \qquad (1)$$

where t_0, $f(t)$, ϕ_0, and T_{sym} represent the starting time of the chirp, the instantaneous frequency at time t, initial phase, and chirp duration (symbol duration), respectively. Without loss of generality, we assume that f_0 is the center of available BW, i.e., $[f_0 - \mathrm{BW}/2, f_0 + \mathrm{BW}/2]$, and the starting time and the initial signal phase are set to zero. Then we have:

$$\phi(t) = 2\pi f_0 t + 2\pi \int_{0}^{t} \Delta f(\alpha)\mathrm{d}\alpha, \ \ 0 \le t \le T_{\mathrm{sym}}, \qquad (2)$$

where $\Delta f(t)$ is the instantaneous frequency-offset at time t. With CSS modulation, the frequency at the beginning of the symbol serves as the information-carrying component, and the chirp resembles a certain type of carrier, according to [7]. Consequently, if the BW is divided into M equal frequency bands, each frequency band (also known as frequency bin in the context of LoRaWAN) represents a specific binary sequence of the length SF. So, generating a CSS signal with a starting frequency that falls into a certain frequency bin is the basis of CSS modulation signaling.

Now, defining a symbol set $\mathcal{S} = \{0, 1, \ldots, M-1\}$, the starting frequency-offset as the information-bearing element of CSS modulation for the symbol $s \in \mathcal{S}$ is equal to $-\mathrm{BW}/2 + \mathrm{BW} \times s/M$ [17]. This is the foundation of generating the mentioned M orthogonal chirps as the basis

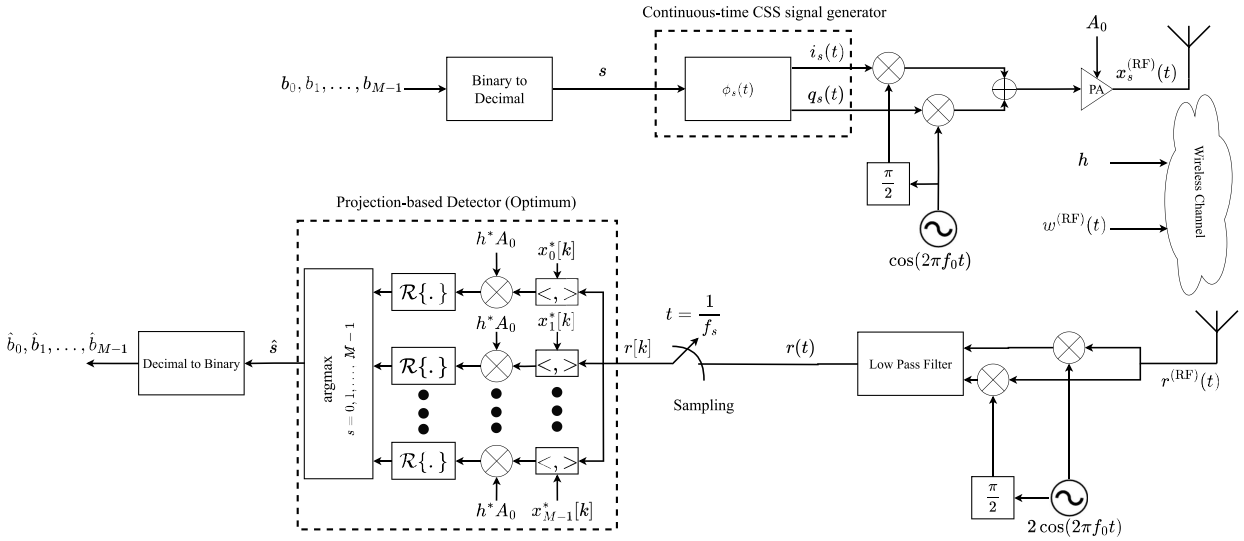

FIGURE 3. End-to-end communication system with CSS modulation for LoRaWAN applications.

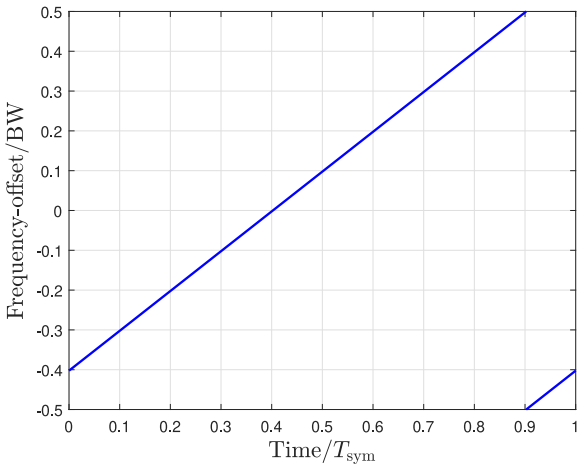

FIGURE 4. Instantaneous frequency-offset for $s = 50$, SF = 9, BW = 250 kHz, and $T_{\text{sym}} = 2.048$ ms.

of CSS modulation. The CSS modulation configuration presented by Semtech has a set of specific values of BW and SF for being exploited in IoT applications, i.e., BW $\in \{125, 250, 500\}$ kHz and SF $\in \{7, 8, 9, 10, 11, 12\}$ [40]. Figure 4 shows the chirp frequency-offset for $s = 50$, SF = 9, and BW = 250 kHz.

The time instant T_w is introduced as the wrap-around time and is related to the symbol duration as $T_w = T_{\text{sym}} - T_{\text{sym}} \times s/M$. Based on this, the instantaneous frequency offset of the CSS signal modulating the symbol s can be formulated as [17]:

$$\Delta f_s(t) = \begin{cases} -\frac{\text{BW}}{2} + \frac{\text{BW}}{M}s + \frac{\text{BW}}{T_{\text{sym}}}t, & 0 \le t < T_w, \\ -\frac{3\text{BW}}{2} + \frac{\text{BW}}{M}s + \frac{\text{BW}}{T_{\text{sym}}}t, & T_w \le t \le T_{\text{sym}}. \end{cases} \tag{3}$$

The chirp rate is defined as the rate at which the chirp frequency varies over time and is formulated as:

$$R_{\text{chirp}} = \frac{\text{BW}}{T_{\text{sym}}} = \frac{\text{BW}^2}{M}, \ (\text{Hz/s}), \tag{4}$$

where $T_{\text{sym}} = M/\text{BW}$. As proved in [17], the following equation holds for all values of s:

$$\int_0^{T_{\text{sym}}} \Delta f_s(\alpha) \mathrm{d}\alpha = 0, \tag{5}$$

and considering (2) as a function of s, i.e., $\phi_s(t)$:

$$\phi_s(t) = 2\pi f_0 t + 2\pi \int_0^t \Delta f_s(\alpha) d\alpha, \tag{6}$$

we obtain $\phi_s(T_{\text{sym}}) = \phi_s(0) = 0$ which means that the starting and final phases of each symbol are equal [17].

Now, by obtaining the general expression of the CSS signal phase in the continuous time, which is a function of s and consequently, a function of the input data bit sequence, we will go through the data transmission procedure of the CSS modulation-based transmitter shown in Figure 3.

C. CSS TRANSMITTER

Considering the input data sequence of $b_0, b_1, \ldots, b_{\text{SF}-1}$, the output of the binary to decimal block can be written as:

$$s = \sum_{i=0}^{\text{SF}-1} b_i 2^i. \tag{7}$$

Then, the continuous-time phase $\phi_s(t)$ is generated according to the equation (6) which results in the in-phase term $i_s(t)$ and quadrature term $q_s(t)$ as:

$$i_s(t) = \cos\left[\phi_s(t)\right] g_{T_{\text{sym}}}(t), \tag{8}$$

and

$$q_s(t) = \sin\left[\phi_s(t)\right] g_{T_{\text{sym}}}(t), \tag{9}$$

where $g_{T_{\text{sym}}}(t) = 1$ for $0 \le t \le T_{\text{sym}}$ and $g_{T_{\text{sym}}}(t) = 0$ elsewhere. However, the CSS is implemented in a more simple way in practice. In particular, the symbol s is fed to

a digital CSS modulator which is based on a look-up table (LUT) design and then, using digital-to-analog converters, the continuous-time in-phase term $i_s(t)$ and quadrature term $q_s(t)$ are generated. We discuss the procedure that leads to such implementation next.

Assume that $s = 0$. With this assumption, we achieve the CSS modulation basic up-chirp, also known as the reference up-chirp phase, for which the frequency starts from the minimum value of $-\mathrm{BW}/2$ and it is the basis of CSS modulation for generating M symbols for a given data bit stream. Accordingly, the continuous-time phase $\phi_0(t)$ is obtained by substituting (3) into (6) as:

$$\phi_0(t) = 2\pi\left[-\frac{\mathrm{BW}}{2}t + \frac{\mathrm{BW}}{2T_{\mathrm{sym}}}t^2\right],\ 0 \le t \le T_{\mathrm{sym}}. \quad (10)$$

For the digital implementation of CSS signal generation, the expression in (10) can be rewritten as:

$$\left\{\phi_0^{(\mathrm{SF})}[k]\right\}_{k=0}^{M-1} = \left\{k\pi\left[-1 + \frac{k}{2^{\mathrm{SF}}}\right]\right\}_{k=0}^{M-1}. \quad (11)$$

which is obtained as M samples forming the discrete-time phase of the CSS basic up-chirp stored in the LUT.[1] We also add the superscript (SF) in the sampled version of the phase for the notional simplicity of the following analysis. As proved in [17], with the help of the reference up-chirp phase denoted as $\{\phi_0^{(12)}[k]\}_{k=0}^{2^{12}-1}$, it is possible to obtain the phase samples for any SF and any symbol s using the following equation:

$$\left\{\phi_s^{(\mathrm{SF})}[k]\right\} = \frac{1}{C}\left\{\phi_0^{(12)}\left[C \times \left((k+s) \mod 2^{\mathrm{SF}}\right)\right]\right\} - \frac{1}{C}\phi_0^{(12)}[sC], \quad (12)$$

where $C = 2^{12-\mathrm{SF}}$. Also, the term $-\frac{1}{C}\phi^{(12)}[sC]$ is due to phase continuity as mentioned before. Therefore, the procedure that takes place in the CSS digital implementation can be summarized as following steps:

- Taking the value of s as the input, the phase samples are calculated using the LUT and equation (12).
- The discrete-time in-phase and quadrature signals, i.e., $i_s[k]$ and $q_s[k]$, are generated as follows:

$$i_s[k] = \cos\left[\phi_s^{(\mathrm{SF})}[k]\right], \quad (13)$$

and

$$q_s[k] = \sin\left[\phi_s^{(\mathrm{SF})}[k]\right], \quad (14)$$

for $k = 0, 1, \ldots, M-1$.

Afterward, using digital-to-analog (DAC) blocks and pulse shaping, the continuous-time in-phase and quadrature signals, i.e., $i_s(t)$ and $q_s(t)$, same as obtained in (8) and (9). Based on the presented discussion, the LUT-based CSS signal generation procedure is illustrated in Figure 5, which can be replaced as the CSS signal generation block of Figure 3.

[1]It is equivalent to sample the continuous-time phase in (10) with a sampling frequency of $f_s = 1/T_s = \mathrm{BW} = 2^{\mathrm{SF}}/T_{\mathrm{sym}}$ [7], [18], [21]. The logic behind this sampling frequency selection is discussed in Remark 3.

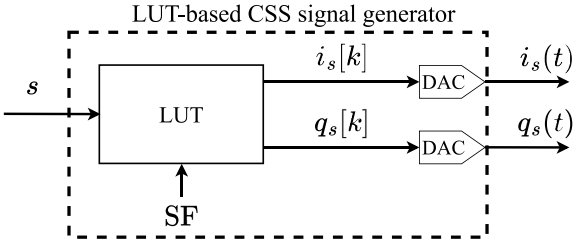

FIGURE 5. LUT-based CSS signal generator.

Then, after up-converting the generated baseband CSS signal and allocating the transmission power A_0, the final high-pass CSS signal is formulated as:

$$x_s^{(\mathrm{RF})}(t) = A_0 i_s(t)\cos(2\pi f_0 t) + A_0 q_s(t)\sin(2\pi f_0 t). \quad (15)$$

D. CSS RECEIVER

Similar to any other communication system, after receiving a LoRa frame at the receiver, one of the main steps is to perform synchronization. Synchronization is vital for aligning incoming data symbols with the receiver's demodulation window. In LoRaWAN protocol, the preamble part of the LoRa frame consists of consecutive basic up-chirps, which undergo channel delays and arrive at the receiver as repeated symbols. Time-delayed CSS symbols shift to adjacent frequency bins, allowing the receiver to retroactively align the subsequent stream of data symbols based on previously sent known symbols. Hence, for LoRa communication synchronization, the first main task is to identify the preamble section. This is only a brief explanation of the LoRaWAN synchronization. The detailed synchronization process which is based on CSS modulation features will be discussed in detail in Section VI of this paper. For the rest of this section, we assume that perfect synchronization is achieved.

At the receiver side, the received signal $r(t)$ can be expressed as follows:

$$r^{(\mathrm{RF})}(t) = h x_s^{(\mathrm{RF})}(t) + w^{(\mathrm{RF})}(t), \quad (16)$$

where $w^{(\mathrm{RF})}(t)$ is the thermal noise of the band-pass signal and $h = \alpha\exp(j\psi)$ represents the complex channel coefficient (in which α denotes the channel attenuation and ψ represents the phase shift). It is assumed that the channel gain is constant during the transmission of a CSS signal. It is worth noting that the transmitter generates the chirp signal with a specific SF parameter known to the receiver.

According to Figure 3, the terms $r_{i,s}(t)$ and $r_{q,s}(t)$ can be obtained as follows:

$$\begin{aligned} r_{i,s}^{(\mathrm{RF})}(t) &= r(t) \times 2\cos(2\pi f_0 t) \\ &= hA_0 i_s(t)\left[1 + \cos(4\pi f_0 t)\right] + hA_0 q_s(t)\sin(4\pi f_0 t) \\ &\quad + 2w^{(\mathrm{RF})}\cos(2\pi f_0 t). \quad (17) \\ r_{q,s}^{(\mathrm{RF})}(t) &= r(t) \times 2\sin(2\pi f_0 t) \ = hA_0 i_s(t)\sin(4\pi f_0 t) \end{aligned}$$

$$+ hA_0 q_s(t)\big[1 - \cos(4\pi f_0 t)\big] + 2w^{(\mathrm{RF})} \sin(2\pi f_0 t). \quad (18)$$

Then, using the low pass filter (LPF), the high-frequency components are canceled and the analytical complex envelope of the received signal can be formulated as:

$$r(t) = hA_0 i_s(t) + jhA_0 q_s(t) + w(t) = hx_s(t) + w(t), \quad (19)$$

where $x_s(t) = A_0 i_s(t) + jA_0 q_s(t)$ is the continuous-time complex envelope of the baseband CSS signal. At this stage, the received signal is then ready to perform the sampling. However, selecting the proper sampling frequency for the CSS receiver is not based on complying with the well-known Nyquist sampling theorem, i.e., selecting the sampling frequency $f_s = 2\mathrm{BW}$. Otherwise, in CSS receiver, we select $f_s = \mathrm{BW}$. The reason for this selection will be discussed in detail in **Remark 3** after the discussion on the maximum likelihood (ML) receiver and the dechirping concept. Now, the sampled baseband received CSS signal is fed into the projection-based receiver to find an estimation of the transmitted CSS symbol, i.e., $\hat{s}$. To this end, we rewrite the discrete-time received CSS signal as:

$$r[k] = hx_s[k] + w[k]. \quad (20)$$

where $w[k]$ is the AWGN with $w[k] \sim \mathcal{CN}(0, \sigma^2)$.

Before starting the derivation of the CSS ML detector, we present some discrete-time CSS signal expressions resulting from the sampling process of the baseband continuous-time CSS signal $x_s(t)$ with $f_s = \mathrm{BW}$. Using (11), (12), (8), and (9), it is straightforward to show that the discrete-time baseband CSS waveform can be formulated as follows [18]:

$$x_s[k] = A_0 \exp\left(2\pi j \frac{k^2 + 2ks - kM}{2M}\right), \quad (21)$$

for $k = 0, 1, \ldots, M-1$.

Remark 1 (Continuous-Phase vs Non-Continuous Phase Versions of CSS Modulation): The equation of CSS waveform in (21) is obtained for continuous-phase CSS in which the starting phase and end phase of each CSS signal, regardless of the symbol s, are equal. However, in the literature, several works, e.g., [41], [42], [43], exploit the non-continuous phase form of CSS modulation which can be obtained as:

$$x_s^{(\mathrm{NC})}[k] = A_0 \exp\left[2\pi j \frac{(k+s)^2 - M(k+s)}{2M}\right]. \quad (22)$$

For the purpose of illustration, in Figure 6, the discontinuity between the phases of three different CSS signals obtained by substituting $s_1 = 1$, $s_2 = 20$, and $s_3 = 100$ into (22) is highlighted with the red ellipses. However, it can be seen that there are no phase jumps for the same CSS symbols using (21). Note that according to the above-mentioned discussion, there are two versions of CSS modulation existing in the literature. However, the continuous-phase version has better power spectral characteristics (lower out-of-band emissions [21]) and the corresponding receiver is simpler to implement in terms of power amplifiers. We adopt the continuous-phase CSS signal for the discussions provided in the rest of this section. Also, note that this Remark is presented with the aim of clarifying the difference between CSS signal waveform expression in various works existing in the literature.

To continue with the detector derivation, assume that the channel information is available at the receiver. Therefore, the coherent detection rule is based on finding the ML estimate of s that maximizes the log-likelihood function. The likelihood function is obtained as:

$$f(s|\mathbf{r}, h) = \frac{1}{(\pi\sigma^2)^M} \exp\left(-\sum_{k=0}^{M-1} \frac{|r[k] - hx_s[k]|^2}{\sigma^2}\right), \quad (23)$$

where $\mathbf{r} = [r[0], r[1], \ldots, r[M-1]]$. After some mathematical simplifications, we obtain

$$f(s|\mathbf{r}, h) = \zeta \exp\left(\sum_{k=0}^{M-1} 2 \times \mathcal{R}\big\{h^* r[k] x_s^*[k]\big\}\right), \quad (24)$$

where $\mathcal{R}\{.\}$ is the real part and ζ is a constant term expressed as:

$$\zeta = \frac{1}{(\pi\sigma^2)^M} \exp\left(\frac{-A_0^2 - \sum_{k=0}^{M-1} |r[k]|^2}{\sigma^2}\right). \quad (25)$$

Taking the logarithm of both sides in (23), the ML estimate of the transmitted CSS symbol is:

$$\hat{s} = \underset{s=0,1,\ldots,M-1}{\arg\max} \mathcal{R}\left\{h^* \sum_{k=0}^{M-1} r[k] x_s^*[k]\right\}. \quad (26)$$

The summation term in (26) is the equivalent of finding the projection of $r[k]$ onto the CSS signal $x_s[k]$ [7]. This implementation of CSS signal detection requires calculating all possible projections, i.e., M possible CSS signal waveform, and finding the one that maximizes the result. Note that in Figure 3, in the projection-based detector block which corresponds to (26), $<,>$ is the inner product operation between two vectors $\mathbf{r}$ and $\mathbf{x}_s^* = [x_s^*[0], x_s^*[1], \ldots, x_s^*[M-1]]$.

In practice, the CSS signal detection is performed using a simpler scheme. For the sake of this discussion and simplicity of notation, we use the following definitions:

1) Down-chirp continuous-phase CSS signal as $x_{s,\mathrm{D}}[k] = A_0 \exp\left(-2\pi j \frac{k^2+2ks-kM}{2M}\right)$.
2) Down-chirp non-continuous phase CSS signal as $x_{s,\mathrm{D}}^{(\mathrm{NC})}[k] = A_0 \exp\left[-2\pi j \frac{(k+s)^2 - M(k+s)}{2M}\right]$.
3) Basic up-chirp CSS signal (in which $s = 0$) as $x_0[k]$.
4) Basic down-chirp CSS signal (in which $s = 0$) as $x_{0,\mathrm{D}}[k]$.

By carefully looking at the expression of $x_s[k]$ in (21), and also by setting $s = 0$, it can be observed that there is a

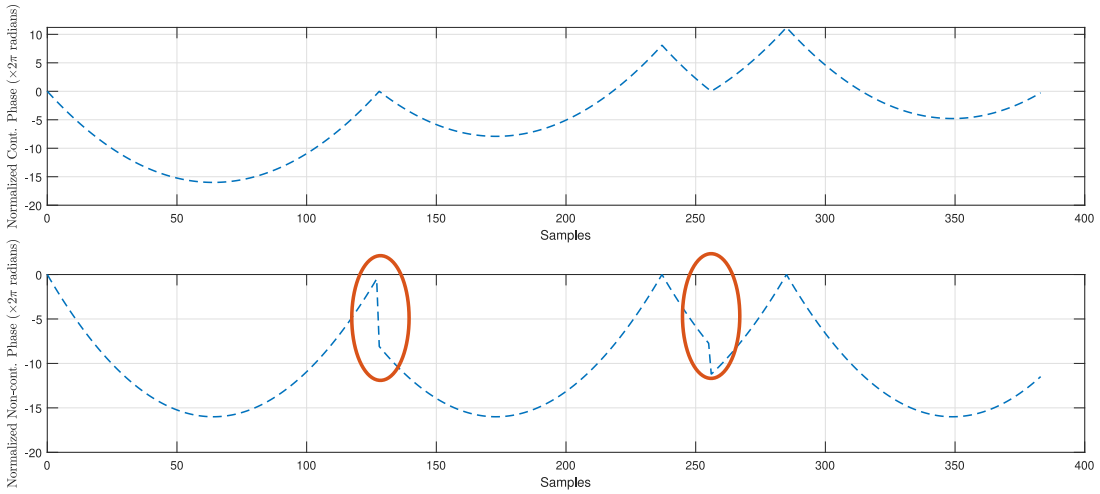

FIGURE 6. Illustration of the phase property of continuous and non-continuous phase CSS waveforms.

relation between a discrete-time CSS signal modulating the CSS symbol s and the basic up-chirp $x_0[k]$ as:

$$x_s[k] = A_0 x_0[k] \exp\left(2\pi j \frac{ks}{M}\right). \tag{27}$$

Substituting (27) in (26) yields:

$$\hat{s} = \underset{s=0,1,\ldots,M-1}{\arg\max} \mathcal{R}\Big\{h^* A_0 \sum_{k=0}^{M-1} \underbrace{r[k]x_0^*[k]}_{r^{(\text{dech.})}[k]} \times \exp\left(-2\pi j \frac{ks}{M}\right)\Big\}. \tag{28}$$

Considering the expression (28), it can be seen that instead of performing the correlation for all M possible values of the CSS symbols and finding the maximum, if we calculate the term $r^{(\text{dech.})}[k]$ after the sampling and perform an M-point discrete Fourier transform (DFT) on the results, the estimation of $\hat{s}$ is the maximum value of the DFT output. In fact, this is the CSS detection procedure that is implemented in practical systems. The operation of multiplication of the received signal $r[k]$ with the complex conjugate of the basic up-chirp $x_0^*[k]$ is called dechirping [7], [21]. Hence, we can replace our projection-based detector in Figure 3 with the detector illustrated in Figure 7. Just note that the DFT is implemented as a fast Fourier transform (FFT) block.

Remark 2 (Intuition About the Dechirping Process): The dechirping process in CSS modulation holds significant importance as it facilitates the recovery of transmitted information. By analyzing the received chirp signal, the dechirping process enables the extraction of the original data which is a crucial step for accurate data retrieval, noise reduction, and enhancing the resilience of CSS modulation in various real-world scenarios. Note that to illustrate the effect of the dechirping and Fourier transform in the detector, we carry out the operations in the continuous time domain in this remark. As mentioned, the dechirping includes the multiplication of a CSS signal by the complex conjugate of

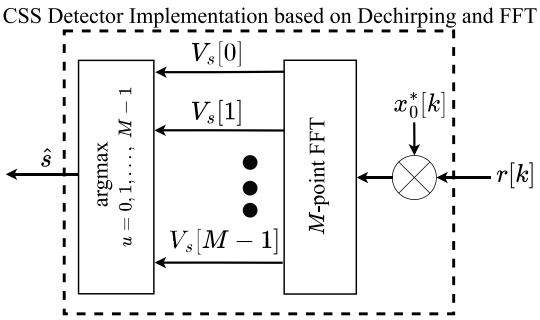

FIGURE 7. Practical implementation of CSS signal detection based on dechirping and FFT.

the basic up-chirp to obtain the dechirped CSS signal as follows:

$$x_s^{(\text{dech.})}(t) = x_s(t) \times x_0^*(t), \tag{29}$$

which yields (30) at the bottom of the next page after next where $T_{\hat{w}}$ is the residual chirp duration after folding, i.e., $T_{\hat{w}} = T_{\text{sym}} - T_w$. Note that here we do not consider noise and fading for the ease of explanation of the demodulation process and their effects will be discussed in detail in Section II-E. By taking the continuous-time Fourier transform (CTFT) of (14) and computing its modulus [17], we obtain (31) as indicated at bottom of the next page, where $f_0^{(1)} = s\text{BW}/M$ and $f_0^{(2)} = -\text{BW} + s\text{BW}/M$. As depicted in Figure 8, the resulting peaks at two frequencies of $f_0^{(1)}$ and $f_0^{(2)}$. Therefore, one can find the transmitted symbol s by finding the peak value of the dechirped signal and the corresponding frequency bins. The two peaks at the frequency domain of the dechirped CSS signal are non-symmetric in general. However, in [44] and [45], the detection is performed based on a single peak in the frequency domain. It is important to note that in discrete time domain operations, the positive frequency peak will indicate the location of the frequency peak corresponding to the CSS symbol s (the frequency bins are equally spaced frequency ranges obtained by dividing the BW to M).

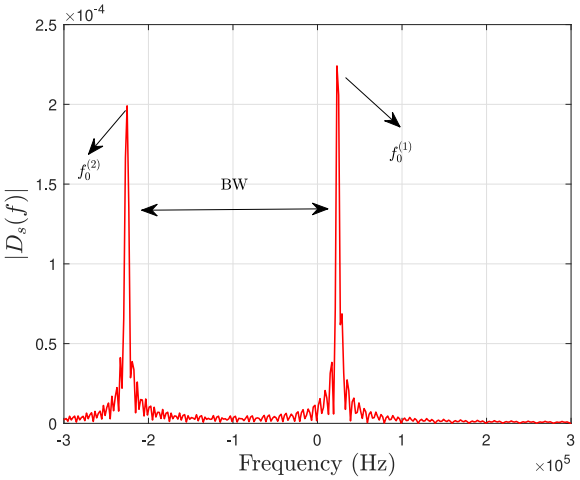

FIGURE 8. Amplitude spectrum for $s = 50$, $SF = 10$ and $BW = 250$ kHz.

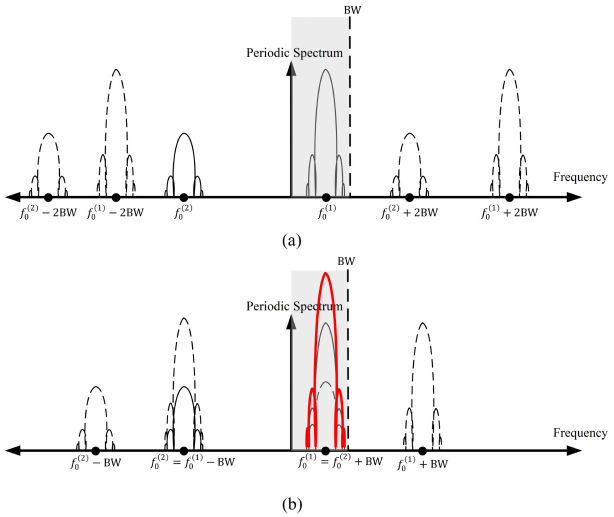

FIGURE 9. Periodic spectrum of discrete-time dechirped CSS signal for (a) $f_s \approx 2$BW, and (b) $f_s = $ BW.

Remark 3 (Sampling Frequency Selection): Here, we intend to briefly discuss the resulting single peak that was investigated thoroughly in [17]. Considering the CTFT of the dechirped signal $r_{\text{cont.}}^{(\text{dech.})}(t)$ as $R_{\text{cont.}}^{(\text{dech.})}(f)$, the discrete-time signal with the sampling frequency of f_s has a periodic spectrum of [46]:

$$R_{\text{disc.}}^{(\text{dech.})}(f) = f_s \sum_{i=-\infty}^{\infty} R_{\text{cont.}}^{(\text{dech.})}(f - if_s). \tag{32}$$

The key point here is to explain the proper selection of f_s as $f_s = $ BW instead of complying with the sampling theorem requirement which suggests $f_s \geq 2$BW. It is obvious that this under-sampling results in aliasing in the frequency domain. If we sample the signal $r_{\text{cont.}}^{(\text{dech.})}(t)$, the resulting spectrum would be periodic with the period of the selected f_s. If we comply with the sampling theorem and select our sampling frequency as $f_s \approx 2$BW, we obtained the period spectrum as in Figure 9 (a). However, in the case of $f_s = $ BW, and as can be seen in Figure 9 (b), due to the fact that the difference between $f_0^{(1)}$ and $f_0^{(2)}$ is equal to BW, we will have constructive aliasing (red diagram in Figure 9 (b)) at the processing BW. This results in a higher peak at the desired frequency bin and improves the detection performance. Note that this cannot result in multiple frequency peaks in the BW that can distort the signal and interrupt the detection. Also, it has been shown in [17] that this useful peak is an increasing function of SF and therefore, we can achieve better performances for higher SFs in terms of communication reliability.

Taking above discussion into account, and considering the equation (20), the dechirping process for demodulation of the received signal can be expressed as follows:

$$\begin{aligned} r^{(\text{dech.})}[k] &= r[k] \times x_0^*[k] = hx_s[k] \times x_0^*[k] + \hat{w}[k] \\ &= hA_0^2 \exp\left[j2\pi \frac{k(s+M)}{M}\right] + \hat{w}[k], \end{aligned} \tag{33}$$

where $\hat{w}[k]$ is the dechirped version of AWGN signal ($\hat{w}[k] \sim \mathcal{CN}(0, \sigma^2)$). Now, by taking an M-point discrete Fourier transform (DFT) of $r^{(\text{dech.})}[k]$, the frequency domain signal

$$\begin{aligned} x_s^{(\text{dech.})}(t) &= \begin{cases} A_0 \exp\left[j2\pi \frac{\text{BW}}{M} s\big(t - nT_{\text{sym}}\big)\right], & nT_{\text{sym}} \leq t < nT_{\text{sym}} + T_w \\ A_0 \exp\left[j2\pi \big(-\text{BW} + \frac{\text{BW}}{M} s\big)\big(t - nT_{\text{sym}}\big)\right], & nT_{\text{sym}} + T_w \leq t < (n+1)T_{\text{sym}} \end{cases} \\ &= A_0 \exp\left[j2\pi \frac{\text{BW}}{M} s\big(t - nT_{\text{sym}}\big)\right] \times g_{T_w}(t - nT_{\text{sym}}) \\ &\quad + A_0 \exp\left[j2\pi \left(-\text{BW} + \frac{\text{BW}}{M} s\right)\big(t - nT_{\text{sym}}\big)\right] \times g_{T_{\hat{w}}}(t - nT_{\text{sym}} - T_w). \end{aligned} \tag{30}$$

$$\begin{aligned} \big|D_s(f)\big| &= \Big|A_0 T_w \text{sinc}\Big[\big(f - f_0^{(1)}\big)T_w\Big] \exp\left[-j2\pi \big(f - f_0^{(1)}\big)\left(nT_{\text{sym}} + \frac{T_w}{2}\right)\right] \exp\left(-j2\pi f_0^{(1)} nT_{\text{sym}}\right) \\ &\quad + A_0 T_{\hat{w}} \text{sinc}\Big[\big(f - f_0^{(2)}\big)T_{\hat{w}}\Big] \exp\left[-j2\pi \big(f - f_0^{(2)}\big)\left(nT_{\text{sym}} + T_w + \frac{T_{\hat{w}}}{2}\right)\right] \exp\left(-j2\pi f_0^{(2)} nT_{\text{sym}}\right)\Big| \\ &= A_0 T_w \text{sinc}\Big[\big(f - f_0^{(1)}\big)T_w\Big] + A_0 T_{\hat{w}} \text{sinc}\Big[\big(f - f_0^{(2)}\big)T_{\hat{w}}\Big]. \end{aligned} \tag{31}$$

is obtained as:

$$\begin{aligned} V_s[u] &= \frac{1}{\sqrt{M}} \sum_{k=0}^{M-1} r^{(\text{dech.})}[k] \exp\left(-\frac{j2\pi uk}{M}\right) \\ &= \frac{1}{\sqrt{M}} \sum_{k=0}^{M-1} \left\{ hA_0^2 \exp\left[j2\pi \frac{k(s+M)}{M}\right] + \hat{w}[k] \right\} \\ &\quad \times \exp\left(-\frac{j2\pi uk}{M}\right) \\ &= \frac{1}{\sqrt{M}} hA_0^2 \sum_{k=0}^{M-1} \underbrace{\exp\left\{j2\pi \frac{k(s+M-u)}{M}\right\}}_{\text{is periodic with the period of } M} + W[u] \\ &= \begin{cases} \sqrt{M}\alpha e^{j\psi} A_0^2 + W[u], & \text{if } u = s, \\ W[u], & \text{otherwise.} \end{cases} \end{aligned} \tag{34}$$

From above results, one can obtain the detected symbol $\hat{s}$ using coherent detection as:

$$\hat{s}^{(\text{coh.})} = \underset{u=0,1,\ldots,M-1}{\arg\max} \; V_s[u] \times \exp(-j\psi). \tag{35}$$

Moreover, the non-coherent detection rule is formulated as follows:

$$\hat{s}^{(\text{non-coh.})} = \underset{u=0,1,\ldots,M-1}{\arg\max} \; |V_s[u]|. \tag{36}$$

It is noteworthy that in the radar systems working based on the chirp signals, the same structure as Figure 7 is used, i.e., the dechirping is performed on the received signal bounced back from the target, and then, FFT is applied on the results. However, in radar systems, this reveals the difference between the time of the transmission and the reception of this chirp signal, helping to estimate the parameters such as the distance between the transmitter and the target.

E. ERROR PERFORMANCE

Here in this section, a thorough analysis of CSS modulation performance in terms of bit error rate (BER) is provided for AWGN and fading channel conditions.

First, assuming $h = 1$ in (20), our channel reduces to an AWGN channel. Several works exist in the literature that obtain closed-form expressions for CSS modulation performance in terms of BER and symbol error rate (SER) under AWGN condition [7], [21], [47], [48], [49], [50], [51]. As a few examples, in [21], the theoretical BER under coherent detection of CSS modulation in AWGN channels is expressed as:

$$\begin{aligned} P_{b,\text{c}}^{(\text{AWGN})} &= \frac{M}{2(M-1)} \\ &\quad \left[1 - \frac{1}{\sqrt{2\pi}} \int_{-\infty}^{\infty} \left(\frac{1}{\sqrt{2\pi}} \int_{-\infty}^{y} \exp\left\{\frac{-x^2}{2}\right\} \text{d}x\right)^{M-1} \right. \\ &\quad \left. \times \exp\left\{-\frac{1}{2}\left(y - \sqrt{\frac{2\log_2 ME_b}{N_0}}\right)^2\right\} \text{d}y\right], \end{aligned} \tag{37}$$

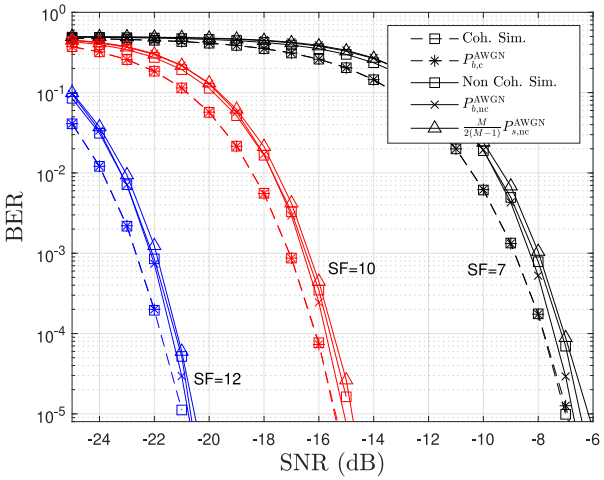

FIGURE 10. BER performance of the CSS modulation under AWGN condition for SF values of 7, 10, and 12.

where $E_b/N_0 = \text{SNR} \times M/\text{SF}$. Moreover, in [47] an approximation of the bit error probability of CSS modulation under non-coherent detection is provided. In particular, the authors exploit Monte Carlo approximation for generating N_{MC} noise samples denoted by $W^{(i)}$ $(i = 1, 2, \ldots, N_{\text{MC}})$ following Gaussian distribution (because of the mathematical limitations in obtaining a closed-form expression for the error probability) and obtain the symbol error probability as:

$$\begin{aligned} P_{s,\text{nc}}^{(\text{AWGN})} &\approx \frac{1}{N_{MC}} \\ &\quad \times \sum_{i=1}^{N_{MC}} 1 - \left[F_{\chi^2}\left(\frac{\left|\sqrt{N} + W^{(i)}\right|^2}{N_0/2}\right)\right]^{N-1}, \end{aligned} \tag{38}$$

where $F_{\chi^2}(.)$ is the cumulative distribution function (CDF) of the Chi-square distribution. Another BER expression is also presented in [48] based on multiple approximations as follows:

$$P_{b,\text{nc}}^{(\text{AWGN})} \approx 0.5\mathcal{Q}\left(\sqrt{\text{SNR} \times 2^{\text{SF}+1}} - \sqrt{1.386\text{SF} + 1.154}\right). \tag{39}$$

Figure 10 is presented to show the CSS modulation performance under AWGN conditions for different values of SF and also to compare the above BER expressions with simulation results. As can be seen, the BER curve corresponding to the approximation (39) is more accurate than (38). Moreover, by decreasing the value of SF from 12 to 7, CSS modulation experiences performance degradation in terms of BER.

Next, we consider the Rayleigh flat fading channel for evaluating the BER performance of CSS modulation. We assume $h = \alpha \exp(j\psi)$ in which α and ψ have Rayleigh and Uniform (in $[0, 2\pi]$) distributions, respectively. Since it is a challenging task to obtain perfect channel state information (CSI) in practical IoT networks, coherent detection can be achieved with extra training overhead which reduces the

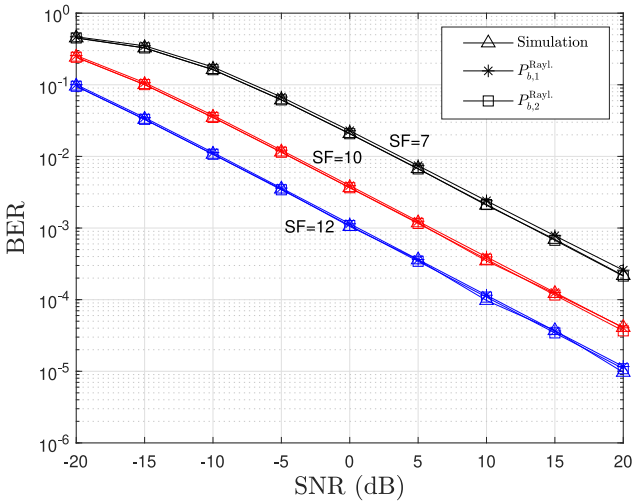

FIGURE 11. BER performance of the CSS modulation in Rayleigh channel for non-coherent detectors.

spectral efficiency (SE). Consequently, here we investigate non-coherent signal detection. As mathematically derived in [52], the symbol error probability for the CSS modulation in the Rayleigh fading channel is formulated as:

$$P_{b,1}^{(\text{Rayl.})} = \frac{M}{2M-2} \times \left[1 - \int_0^{\infty} \frac{1}{1+\overline{\gamma_c}} \exp\left(-\frac{y}{1+\overline{\gamma_c}}\right) \times (1-\exp(y))^{M-1} \text{dy}\right], \tag{40}$$

where $\overline{\gamma_c} = M \times \text{SNR}$. In addition to this expression, a tight closed-form approximation of bit error probability for the Rayleigh fading scenario is derived in [48] as:

$$P_{b,2}^{(\text{Rayl.})} \approx 0.5 \times \left[Q(-\sqrt{2H_{M-1}}) - \sqrt{\frac{\overline{\gamma_c}}{\overline{\gamma_c}+1}} \times \exp\left(-\frac{2H_{M-1}}{2(\overline{\gamma_c}+1)}\right) \times Q\left(\sqrt{\frac{\overline{\gamma_c}}{\overline{\gamma_c}+1}}\left[-2\sqrt{2H_{M-1}} + \frac{\sqrt{2H_{M-1}}}{\overline{\gamma_c}+1}\right]\right)\right], \tag{41}$$

where $H_m \approx \ln(m) + 1/(2m) + 0.57722$. BER curves for the Rayleigh fading scenario are presented in Figure 11. As can be seen, the BER curves for all three cases of simulation, numerical based on the equation (40) and approximation based on the equation (41) match.

In the following subsections, we investigate two of the most important CSS modulation characteristics, i.e., orthogonality and power spectral features.

F. ORTHOGONALITY

Recognizing circumstances in which CSS modulation may be vulnerable to interference or interception requires a thorough grasp of its orthogonality characteristics. That is because of the channel access protocol of LoRaWAN which is based on unslotted ALOHA and uses industrial, scientific, and medical (ISM) frequency bands. Therefore, simultaneous reception of multiple CSS signals at a single LoRaWAN gateway would be expected. The main aim of this subsection is to provide a better understanding of CSS modulation orthogonality and its corresponding conditions inspired by the work of [20] to quantify how orthogonal is CSS modulation. Note that by investigating the orthogonality of CSS modulation in this subsection, our aim is to shed light on the behavior of different CSS signals received by a single LoRaWAN GW, and not the orthogonality between the chirps that can be sent by a single ED.

Considering the cross-correlation function as the main measure of orthogonality between two signals, here in this subsection, the orthogonality of CSS modulation is measured and quantified using the cross-correlation function for four types of CSS signals, i.e., the continuous-time CSS, the continuous-time dechirped CSS, the discrete-time CSS, and the discrete-time dechirped CSS. We focus on calculating the cross-correlation between two CSS waveforms that transmit symbols s_1 and s_2. Without the loss of generality, symbol s_1 is transmitted using SF_1, while symbol s_2 is transmitted using SF_2. The respective bandwidths for the transmissions are BW_1 and BW_2. The symbol transmission times are denoted as $T_{\text{sym},1} = 2^{\text{SF}_1}/\text{BW}_1$ and $T_{\text{sym},2} = 2^{\text{SF}_2}/\text{BW}_2$, corresponding to s_1 and s_2, respectively. The starting frequencies of symbols s_1 and s_2 are f_1 and f_2, respectively. Moreover, without the loss of generality, we assume that SF_1 is less than SF_2, i.e., $\xi = \text{SF}_2 - \text{SF}_1$, where ξ can be any integer from 1 to 5.

The cross-correlation function between two continuous-time waveforms $x_{s_1}(t)$ and $x_{s_2}(t)$ can be defined as:

$$\mathcal{C}_{s_1,s_2}^{(\text{cont.})}(\tau, f_1, f_2) = \int_{t_0+T_{\text{sym},1}}^{t_0+\tau} x_{s_1}(t) x_{s_2}^*(t-\tau)\text{d}t, \tag{42}$$

where τ is the time delay. The closed-form expression for this cross-correlation is calculated as (43) at the bottom of the next page, where we have [20]:

$$\mathcal{K}_{a_{12}}(b_{s_1,s_2}, t_1, t_2) = \begin{cases} \frac{e^{2j\pi c_{s_2}} e^{-j\pi \frac{b_{s_1,s_2}^2}{a_{12}}}}{\sqrt{T_{\text{sym},1} T_{\text{sym},2}}} \times \left[\text{erf}\left(\sqrt{\frac{\pi a_{12}}{j}}\left(t_0 + t_2 + \frac{b_{s_1,s_2}}{a_{12}}\right)\right) - \text{erf}\left(\sqrt{\frac{\pi a_{12}}{j}}\left(t_0 + t_2 + \frac{b_{s_1,s_2}}{a_{12}}\right)\right)\right], & \text{if } a_{12} \neq 0, \\ e^{2j\pi c_{s_2}} e^{j\pi b_{s_1,s_2}(2t_0+t_1+t_2)} \times \frac{\text{sinc}\left[\pi b_{s_1,s_2}(t_2-t_1)\right](t_2-t_1)}{\sqrt{T_{\text{sym},1} T_{\text{sym},2}}}, & \text{if } a_{12} = 0. \end{cases} \tag{44}$$

with $\mu_n = 1/T_{\text{sym},n}$ for $n = 1, 2$, $a_{12} = \mu_1 \text{BW}_1 - \mu_2 \text{BW}_2$, $b_{s_1,s_2} = f_1 + \mu_1 s_1 - f_2 - \mu_2 s_2 + \mu_2 \tau \text{BW}_2$, $c_{s_2} = (f_2 + \mu_2 s_2 - 0.5\mu_2 \tau \text{BW}_2)\tau$, $m_{s_1,s_2}(\tau) = \min(t_{s_1}, \tau + t_{s_2})$, $M_{s_1,s_2}(\tau) = \max(t_{s_1}, \tau + t_{s_2})$, and $\text{BW}_c = \text{BW}_1 U(t_{s_2} + \tau -$

$t_{s_1}) - \mathrm{BW}_2 U(t_{s_1} - t_{s_2} - \tau)$. Also, note that $U(.)$ is the step function as $U(t) = 1$ for $t \geq 0$ and $U(t) = 0$ otherwise and $\mathbb{1}(.)$ is the indicator function as $\mathbb{1}(t \neq a) = 1$ for $t \neq a$ and $\mathbb{1}(t \neq a) = 0$ otherwise. Moreover, we have $\mathrm{erf}(z) = (2/\sqrt{\pi}) \int_0^z e^{-t^2} \mathrm{d}t$ and $\mathrm{sinc}(z) = \sin(z)/z$.

The cross-correlation between two continuous-time dechirped CSS waveforms $x_{s_1}(t) \times x_0^*(t)$ and $x_{s_2}(t) \times x_0^*(t)$ can be obtained using (43) with two substitutions as $\tilde{c}_{s_1,s_2} = (2f_2 + \mathrm{BW}_2) + \mu_2 s_2)\tau$ and $\tilde{b}_{s_1,s_2} = \mu_1 s_1 - \mu_2 s_2 + 2f_1 - 2f_2 + \mathrm{BW}_1 - \mathrm{BW}_2$ [20].

Let us assume that we use an identical sampling time T_d for both continuous-time CSS waveforms $x_{s_1}(t)$ and $x_{s_2}(t)$. Based on this, we define parameters $\xi_n = \log_2 \mathrm{BW}_n T_d$ for $n = 1, 2$. Moreover, we define $m_0 = t_0/T_d$ and $m_1 = \tau/T_d$. Accordingly, the cross-correlation function between two discrete-time CSS waveforms $x_1[kT_d]$ and $x_2[kT_d]$ can be formulated as (45) at the bottom of the page [20].

Finally, the cross-correlation between two discrete-time dechirped CSS waveforms can be written as [20]:

$$\mathcal{C}_{s_1,s_2}^{(\text{dechirped disc.})}(\tau, f_1, f_2) = \begin{cases} \frac{e^{2j\pi\tilde{c}_{s_2}} e^{2j\pi\tilde{b}_{s_1,s_2}\tau}}{\sqrt{2^{\mathrm{SF}_1} 2^{\mathrm{SF}_2}}} e^{j\pi(2^{\mathrm{SF}_1} - \xi_1 - m_1 - 1)\tilde{b}_{s_1,s_2} T_d} \\ \times \sin\left[\pi(2^{\mathrm{SF}_1} - \xi_1 - m_1)\tilde{b}_{s_1,s_2} T_d\right] \\ \times \mathrm{cosec}(\pi \tilde{b}_{s_1,s_2} T_d), & \text{if } \tilde{b}_{s_1,s_2} \neq 0, \\ \frac{e^{2j\pi\tilde{c}_{s_2}}}{\sqrt{2^{\mathrm{SF}_1} 2^{\mathrm{SF}_2}}} \frac{T_{\mathrm{sym},1} - \tau}{T_d}, & \text{if } \tilde{b}_{s_1,s_2} = 0. \end{cases} \tag{46}$$

Based on these equations and the data provided in [20], we present Figure 12 in which the maximum of the cross-correlation functions of (43), its dechirped version (45), and (46) are plotted with respect to the symbols s_1 and s_2 with $\tau = 0$ and $f_1 = f_2$. Based on these results, several important insights regarding the cross-correlation functions and orthogonality features of CSS modulation can be listed as follows:

- From equations (43) and (45), we can interpret that the maximum cross-correlation between the same SFs in both continuous and discrete time domains is more significant compared to the case with different SFs. Moreover, this difference is particularly prominent prior to down-chirping. Therefore, one can conclude that the interference at the receiver is more significant when the end devices belong to the same LoRa network exploiting the same value of SF.
- Before down-chirping, lower SF_2 values than SF_1 have a greater impact on the value of cross-correlation than higher ones, as their maximum cross-correlations are higher. Additionally, SFs that are closer to each other have a stronger influence on the maximum cross-correlation. This also can be shown numerically from (43) and (45).
- The maximum cross-correlation between different SFs after down-chirping is larger than the one before down-chirping. Moreover, this maximum cross-correlation does not depend on the time domain (discrete or continuous).

Table 4 provides several useful orthogonality conditions for CSS modulation obtained from equations (43), (45), and (46).

G. CSS MODULATION SPECTRAL ANALYSIS

Spectral analysis of CSS modulation is of profound significance as it provides insights into the power distribution of the transmitted signal across the frequency. By examining the spectral characteristics, such as the spread of energy across different frequencies, one can assess the modulation's efficiency and bandwidth utilization. This is important when implementing CSS modulation under a specific regulatory

$$\mathcal{C}_{s_1,s_2}^{(\text{cont.})}(\tau, f_1, f_2) = \begin{cases} \mathcal{K}_{a_{12}}(b_{s_1,s_2} - \mathrm{BW}_1, \tau, T_{\mathrm{sym},1}), & \text{if } t_{s_1} \leq \tau < T_{\mathrm{sym},1} \leq \tau + t_{s_2}, \\ \mathcal{K}_{a_{12}}(b_{s_1,s_2} - \mathrm{BW}_1, \tau, \tau + t_{s_2}) + e^{-2j\pi \mathrm{BW}_2 \tau} \mathcal{K}_{a_{12}}(b_{s_1,s_2} - \mathrm{BW}_1 & \\ + \mathrm{BW}_2, \tau + t_{s_2}, T_{\mathrm{sym},1}), & \text{if } t_{s_1} \leq \tau < \tau + t_{s_2} \leq T_{\mathrm{sym},1}, \\ \mathcal{K}_{a_{12}}(b_{s_1,s_2}, \tau, t_{s_1}) + \mathcal{K}_{a_{12}}(b_{s_1,s_2} - \mathrm{BW}_1, t_{s_1}, T_{\mathrm{sym},1}), & \text{if } \tau < t_{s_1} < T_{\mathrm{sym},1} \leq \tau + t_{s_2}, \\ \mathcal{K}_{a_{12}}(b_{s_1,s_2}, \tau, m_{s_1,s_2}(\tau)) & \\ + e^{-2j\pi \mathrm{BW}_2 \tau U(t_{s_1} - \tau - t_{s_2})} \mathcal{K}_{a_{12}}(b_{s_1,s_2} - \mathrm{BW}_c, m_{s_1,s_2}(\tau), M_{s_1,s_2}(\tau)) & \\ \times \mathbb{1}(t_{s_1} - \tau \neq t_{s_2}) + e^{-2j\pi \mathrm{BW}_2 \tau} \times \mathcal{K}_{a_{12}}(b_{s_1,s_2} - \mathrm{BW}_1 + \mathrm{BW}_2, M_{s_1,s_2}(\tau), T_{\mathrm{sym},1}), & \text{if } \tau < t_{s_1} \,\&\, \tau + t_{s_2} < T_{\mathrm{sym},1}. \end{cases} \tag{43}$$

$$\mathcal{C}_{s_1,s_2}^{(\text{disc.})}(\tau, f_1, f_2) = \begin{cases} \frac{e^{2j\pi c_{s_2}} e^{-j\pi a_{12}\left(\frac{b_{s_1,s_2}}{a_{12}}\right)^2}}{\sqrt{2^{\mathrm{SF}_1} 2^{\mathrm{SF}_2}}} \sum_{n'=m_1}^{2^{\mathrm{SF}_1} - \xi_1 - 1} e^{j\pi a_{12}\left(n' T_d + \frac{b_{s_1,s_2}}{a_{12}}\right)^2}, & \text{if } a_{12} \neq 0, \\ \frac{e^{2j\pi c_{s_2}} e^{2j\pi b_{s_1,s_2} T_d m_1} e^{j\pi(2^{\mathrm{SF}_1} - \xi_1 - m_1 - 1) b_{s_1,s_2} T_d}}{\sqrt{2^{\mathrm{SF}_1} 2^{\mathrm{SF}_2}}} \mathrm{cosec}(\pi b_{s_1,s_2} T_d) \sin\left[\pi(2^{\mathrm{SF}_1 - \xi_1} - m_1) b_{s_1,s_2} T_d\right], & \text{if } a_{12} \neq 0 \,\&\, b_{s_1,s_2} \neq 0, \\ \frac{e^{2j\pi c_{s_2}}}{\sqrt{2^{\mathrm{SF}_1} 2^{\mathrm{SF}_2}}} \frac{T_{\mathrm{sym},1} - \tau}{T_d}, & \text{if } a_{12} = 0 \,\&\, b_{s_1,s_2} = 0. \end{cases} \tag{45}$$

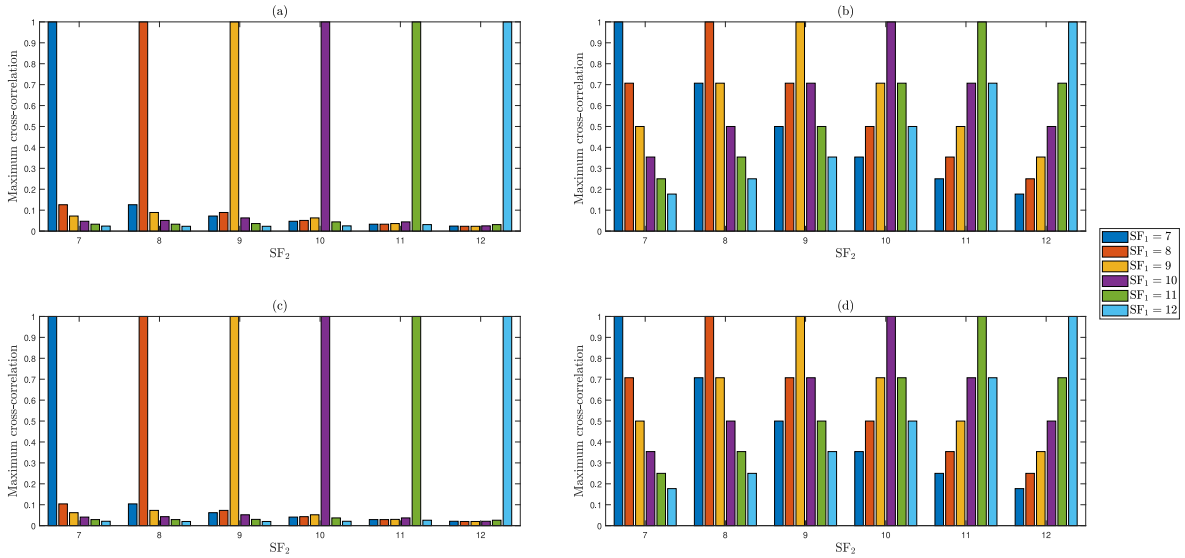

FIGURE 12. Maximum of cross-correlation with respect to the symbols s_1 and s_2 with $\tau = 0$ and $f_1 = f_2$ for two CSS signals in forms of (a) continuous-time, (b) dechirped continuous time, (c) discrete-time, and (d) dechirped discrete-time.

TABLE 4. Orthogonality conditions of CSS modulated waveforms [20].

	SF	BW	τ	$f_d = f_2 - f_1$	Orthogonality conditions ($\omega = 0$ for SF even and $\omega = 1$ for SF odd)
Cont.	$\mathrm{SF}_1 = \mathrm{SF}_2$	$\mathrm{BW}_1 = \mathrm{BW}_2$	$\tau = 0$	$f_d = 0$	$\lvert s_1 - s_2\rvert \propto \sqrt{2^{\mathrm{SF}+\omega}}$
				$f_d \neq 0$	$f_d \propto \frac{\mathrm{BW}}{2^{\mathrm{SF}}}$, and $\lvert s_1 - s_2 - \frac{f_d 2^{\mathrm{SF}}}{\mathrm{BW}}\rvert \propto \sqrt{2^{\mathrm{SF}+\omega}}$
			$\tau \neq 0$	$f_d = 0$	$\tau \propto \frac{1}{\mathrm{BW}}$, and $\lvert s_1 - s_2 + \mathrm{BW}\tau\rvert \propto \sqrt{2^{\mathrm{SF}+\omega}}$
				$f_d \neq 0$	$\tau \propto \frac{1}{\mathrm{BW}}$, $f_d \propto \frac{\mathrm{BW}}{2^{\mathrm{SF}}}$, and $\lvert s_1 - s_2 + \mathrm{BW}\tau - \frac{f_d 2^{\mathrm{SF}}}{\mathrm{BW}}\rvert \propto \sqrt{2^{\mathrm{SF}+\omega}}$
Disc.	$\mathrm{SF}_1 = \mathrm{SF}_2$	$\mathrm{BW}_1 = \mathrm{BW}_2$	$\tau = 0$	$f_d = 0$	$s_1 - s_2 \neq 0$
				$f_d \neq 0$	$f_d \propto \frac{\mathrm{BW}_1}{2^{\mathrm{SF}_1}}$ and $s_1 - s_2 - f_d \frac{2^{\mathrm{SF}_1}}{\mathrm{BW}_1} \neq 0$
			$\tau \neq 0$	$f_d = 0$	$(2^{\mathrm{SF}_1} - \mathrm{BW}_1\tau)(s_1 - s_2 + \mathrm{BW}_1\tau) \propto 2^{\mathrm{SF}_1}$
				$f_d \neq 0$	$f_d \propto \frac{\mathrm{BW}_1}{2^{\mathrm{SF}_1}}$, and $(2^{\mathrm{SF}_1} - \mathrm{BW}_1\tau)(s_1 - s_2 + \mathrm{BW}_1\tau - f_d \frac{2^{\mathrm{SF}_1}}{\mathrm{BW}_1}) \propto 2^{\mathrm{SF}_1}$
Dechir.	$\mathrm{SF}_1 = \mathrm{SF}_2$	$\mathrm{BW}_1 = \mathrm{BW}_2$	$\tau = 0$	$f_d = 0$	$s_1 - s_2 \neq 0$
				$f_d \neq 0$	$f_d \propto \frac{\mathrm{BW}_1}{2^{\mathrm{SF}_1}}$ and $s_1 - s_2 - 2f_d \frac{2^{\mathrm{SF}_1}}{\mathrm{BW}_1} \neq 0$
			$\tau \neq 0$	$f_d = 0$	$(2^{\mathrm{SF}_1} - \mathrm{BW}_1\tau)(s_1 - s_2) \propto 2^{\mathrm{SF}_1}$
				$f_d \neq 0$	$f_d \propto \frac{\mathrm{BW}_1}{2^{\mathrm{SF}_1}}$ and $(2^{\mathrm{SF}_1} - \mathrm{BW}_1\tau)(s_1 - s_2 - 2f_d \frac{2^{\mathrm{SF}_1}}{\mathrm{BW}_1}) \propto 2^{\mathrm{SF}_1}$
	$\mathrm{SF}_2 = \mathrm{SF}_1 + \xi$	$\mathrm{BW}_2 = 2^{\xi}\mathrm{BW}_1$	$\tau = 0$	$f_d = 0$	$f_d \propto \frac{\mathrm{BW}_1}{2^{\mathrm{SF}_1}}$ and $(s_1 - \frac{s_2}{2^{\xi}} + (1 - 2^{\xi})2^{\mathrm{SF}_1}) \neq 0$
				$f_d \neq 0$	$f_d \propto \frac{\mathrm{BW}_1}{2^{\mathrm{SF}_1}}$ and $(s_1 - \frac{s_2}{2^{\xi}} - 2f_d \frac{2^{\mathrm{SF}_1}}{\mathrm{BW}_1} + (1 - 2^{\xi})2^{\mathrm{SF}_1}) \neq 0$
			$\tau \neq 0$	$f_d = 0$	$(2^{\mathrm{SF}_1} - \mathrm{BW}_1\tau)(s_1 - \frac{s_2}{2^{\xi}} + (1 - 2^{\xi})2^{\mathrm{SF}_1}) \propto 2^{\mathrm{SF}_1}$
				$f_d \neq 0$	$f_d \propto \frac{\mathrm{BW}_1}{2^{\mathrm{SF}_1}}$ and $(2^{\mathrm{SF}_1} - \mathrm{BW}_1\tau)(s_1 - \frac{s_2}{2^{\xi}} - 2f_d \frac{2^{\mathrm{SF}_1}}{\mathrm{BW}_1} + (1 - 2^{\xi})2^{\mathrm{SF}_1}) \propto 2^{\mathrm{SF}_1}$
	$\mathrm{SF}_1 \neq \mathrm{SF}_2$	$\mathrm{BW}_1 \neq \mathrm{BW}_2$	$\forall\tau$	$\forall f_d$	$f_d \propto \frac{\mathrm{BW}_1}{2^{\mathrm{SF}_1}}$ and $(2^{\mathrm{SF}_1} - \mathrm{BW}_1\tau)\Big[s_1 - \frac{\mathrm{BW}_2 2^{\mathrm{SF}_1}}{\mathrm{BW}_1 2^{\mathrm{SF}_2}} s_2 - 2f_d \frac{2^{\mathrm{SF}_1}}{\mathrm{BW}_1} + (1 - \frac{\mathrm{BW}_2}{\mathrm{BW}_1})2^{\mathrm{SF}_1}\Big] \propto 2^{\mathrm{SF}_1}$

requirement in terms of allowable out-of-band emission and spectral limitations. The maximum spectral power density is defined as the highest level in Watts per Hertz generated by the transmitter within the power envelope. As an example, in the European region, there are several requirements of ETSI regulation for adjacent band emissions. These constraints impose a spectral mask on every modulation to be used in the 800 MHz band. Moreover, in the North American region, these limitations are provided by the FCC for the 915 MHz band. Accordingly, one can implement CSS modulation within these bands by carefully taking into account the corresponding constraints. Therefore, obtaining the power spectral density of CSS modulation for different values of BW and SF is of value in the context of LoRaWAN implementation. In the following, the power spectral density of CSS modulation is investigated based on the derivation of [18]. Moreover, an interesting feature is also observed, i.e., the DC component of the CSS signal, based on which we

can conclude that there is a level of inherent transmission power waste associated with CSS modulation.

Assume that we have an information source that generates an infinite sequence of random and independent CSS symbols s_n where $s_n \in \mathcal{S}$ with a probability of $1/M$. Each symbol s_n results in a CSS signal output $x_{s_n}(t)$ and the sequence can be represented by a stochastic process as:

$$P(t) = \sum_{n=-\infty}^{\infty} x_{s_n}(t - nT_{\text{sym}}) g_{T_{\text{sym}}}(t - nT_{\text{sym}}). \quad (47)$$

As provided in [18], [46], the power spectra of this stochastic can be written as the sum of a continuous term and a discrete term as:

$$S(f) = S_c(f) + S_d(f), \quad (48)$$

where [18], [46]

$$S_c(f) = \frac{1}{T_{\text{sym}} M} \times \left[\sum_{s=0}^{M-1} |X_s(f)|^2 - \frac{1}{M} \left| \sum_{s=0}^{M-1} X_s(f) \right|^2 \right], \quad (49)$$

and

$$S_d(f) = \frac{1}{T_{\text{sym}}^2 M^2} \times \sum_{n=-\infty}^{\infty} \left| \sum_{s=0}^{M-1} X_s\left(n \frac{\text{BW}}{M}\right) \right|^2 \delta\left(f - n \frac{\text{BW}}{M}\right), \quad (50)$$

in which $\{X_s(f)\}_{s=0}^{M-1}$ are the CTFT of the continuous-time CSS signals $\{x_s(t)\}_{s=0}^{M-1}$. To find the CTFT $\{X_s(f)\}_{s=0}^{M-1}$, one can exploit Fresnel functions [53] and obtain the following equation [18]:

$$X_s(f) = W\left[\text{BW}\left(\frac{s}{M} - \frac{1}{2}\right) - f; \frac{\text{BW}^2}{2M}; 0; \frac{M-s}{\text{BW}} \right] + W\left[\text{BW}\left(\frac{s}{M} - \frac{3}{2}\right) - f; \frac{\text{BW}}{2M}; \frac{M-s}{\text{BW}}; \frac{M}{\text{BW}} \right], \quad (51)$$

where

$$W(x; y; t_1; t_2) = \frac{1}{\sqrt{y}} e^{-\frac{j2\pi x^2}{4y}} \left[K\left(2\sqrt{y}\left(t_2 + \frac{x}{2y}\right)\right) - K\left(2\sqrt{y}\left(t_1 + \frac{x}{2y}\right)\right) \right], \quad (52)$$

in which $K(.) \triangleq C(.) + jS(.)$ and $C(.)$ and $S(.)$ are Fresnel integrals [53].

The discrete spectrum in (48) is due to the non-zero mean value of the signal. This means that the value of $\mathbb{E}\{x_{s_n}(t)\} \neq 0$ and the CSS signal has a DC component. This results in having a discrete power spectrum at frequencies equal to n/T_{sym} [18], [21] which does not carry any information. The total power of the discrete spectrum is exactly equal to $1/M$ of the total signal power [18]. As an example for the total power of the discrete spectrum, for the case of SF = 7 which yields $M = 128$, 0.78125% of the signal power is carried in the discrete spectrum. Therefore, for CSS modulation, a fraction of $1/M$ of the total power is always wasted.

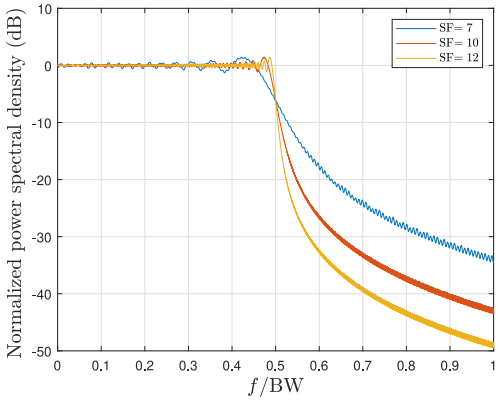

FIGURE 13. Continuous spectrum of the complex envelope for CSS modulation with different values of SF.

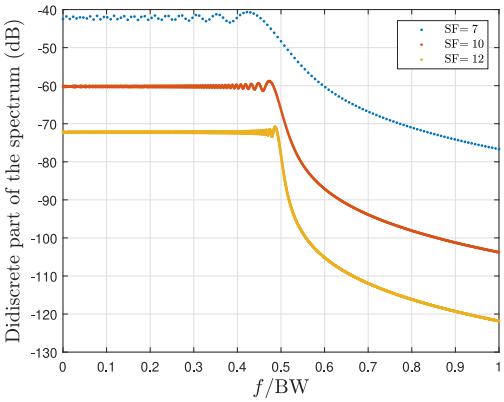

FIGURE 14. Discrete spectrum of the complex envelope for CSS modulation with different values of SF.

In Figure 13 and Figure 14, the normalized power spectral density, $10\log_{10}(S_c(f)\text{BW})$, and the discrete part of the spectrum of the CSS modulation, i.e., the power $10\log_{10}[|\sum_{s_n=0}^{M-1} X_{s_n}(k\frac{\text{BW}}{M})|^2/T_{\text{sym}}^2 M^2]$, are plotted, respectively for different values of SFs. As can be seen, by increasing the value of M, the out-of-band radiation will be reduced.[2]

Given the results provided in [18], it can be observed that CSS modulation meets the requirements of ETSI regulations in terms of maximum power limits for adjacent band emissions. Considering the discussion in this section, one can select the proper values for BW and SF to adjust the power spectra of CSS modulation and make it compatible with the regulatory specifications of the region of implementations. For example, as indicated in [54], the emission level should be:

[2]Please note that in Figure 14 as the SF increases, the distance between the samples decreases, causing the discrete power spectrum to not appear as a discrete-time curve, however, as can be seen, for SF = 7, these sample points are perfectly distinguishable.

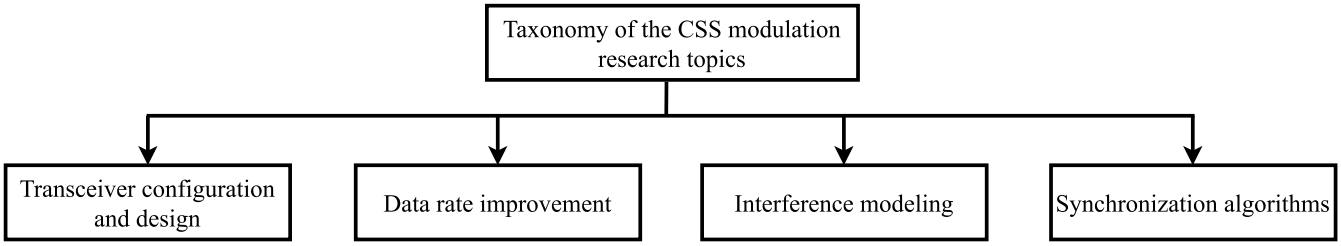

FIGURE 15. Research topics taxonomy of the CSS modulation with IoT application.

- -30 dBm per 1 kHz lower than the inband power for f_0 (kHz) + BW/2 kHz to f_0 (kHz) + BW/2 kHz + 200 kHz,
- -36 dBm per 1 kHz lower than the inband power for f_0 (kHz) + BW/2 kHz to f_0 (kHz) + BW/2 kHz + 200 kHz,
- -36 dBm per 10 kHz lower than the inband power for f_0 (kHz) + BW/2 kHz + 200 kHz to f_0 (kHz) + BW/2 kHz + 400 kHz,
- -36 dBm per 100 kHz lower than the inband power for f_0 (kHz) + BW/2 kHz + 400 kHz to f_0 (kHz) + BW/2 kHz + 1000 kHz.

It is noteworthy that by increasing the value of SF, the spectrum becomes more compact and the number of potential channels within a specific frequency band can be increased.

So far, we have discussed the basic mathematical foundation related to CSS modulation and shed light on its SE characteristics, as well as its BER performance in different channel conditions. In the following section, we investigate recent key advances existing in the literature related to the applications of CSS modulation in the IoT industry. A categorization has been made, as indicated in Figure 15, based on which these existing research studies are divided into four main groups, each of which will be briefly discussed in the following.

1) *Transceiver configuration and design:* By using equation (12), it can be observed that CSS transmission is based on a look-up table (LUT) design that stores the phase samples of the reference up-chirp for SF = 12. However, despite its seemingly straightforward design, the flexibility requirement of CSS modulation would result in more expensive transceivers, as additional hardware resources are required to enable higher SF and BW settings. Generally, the size of the LUT grows exponentially as SF increases. While this may not be a major issue for the currently used SF = 12, which is supported by market LoRa transceivers, the LUT design will become prohibitively expensive if greater SF values are sought in the future. To tackle this issue, a novel receiver structure is presented in [21] which will be discussed in detail in Section III. Furthermore, due to the increasing need for deploying a vast number of IoT devices, traditional terrestrial LoRa networks may become highly dense, and in some regions (such as across oceans), they may not be deployable. Therefore, researching the CSS modulation performance for low Earth orbit (LEO) satellite IoT communication applications is imperative. Moreover, the performance of CSS modulation in fading channels significantly degrades, and it remains a challenging task to exploit CSS modulation for these environments. To overcome this problem, a novel approach integrating CSS modulation with multiple-input multiple-output (MIMO) configuration has been recently proposed which will be discussed in more detail in Section III.
2) *Data rate improvement:* The bit rate of the LoRa transmission scheme is calculated using the following equation:

$$r_b = \mathrm{SF} \times \frac{\mathrm{BW}}{M}. \tag{53}$$

Due to the limited number of orthogonal chirps available in a given bandwidth and symbol duration, long-range communication provided by CSS modulation techniques comes at the cost of very low data rates in the order of a few hundred to a few thousand bits per second [55]. The values of SF and BW are the two main factors that influence the data rate of CSS modulation. For example, for SF = 7 and BW = 500 kHz, the highest data rate is 37.5 kbps [56]. Although this is suitable for most smart city applications in IoT networks, many other potential applications, such as smart home/building, image transmission, and indoor IoT, cannot be supported. Therefore, efforts have been made to improve the data rate of CSS-based transmission schemes. One approach to address the low data rate issue presented in [56] is to exploit multiple transceivers in a device. However, this adds complexity, as several transceivers in a device require more hardware and software resources, particularly at the receiver end. Hence, the research trend in this area tends to modify CSS modulation to improve the data rate. Several works exist in the literature modifying traditional CSS modulation to embed more information bits in the transmitting symbol by combining it with other modulation schemes. These works are comparatively presented and discussed in Section IV.

3) *Interference modeling:* Decoding the received CSS signals in the presence of interference has been addressed in the literature, as packet collisions are common due to the extended transmission times of LoRa packets and the ALOHA-based protocol. As the number of LoRa devices grows in the future, this problem will worsen, putting the scalability of LoRa networks at risk as they become interference-constrained. In existing works discussing the interference in LoRa networks, it is assumed that destructive collisions occur when two or more signals are received in the same frequency band and with the same SF because CSS signals with different spreading factors are practically orthogonal since the rejection gain ranges from 16 to 36 dB [57]. On the other hand, as discussed in Section II, the authors in [20] have thoroughly discussed the orthogonality of CSS modulation based on mathematically derived cross-correlation functions and it has been confirmed that CSS modulation orthogonality relies on many factors such as the value of the SF, bandwidth, and time delay. We will review several works discussing the interference in LoRa networks and investigate their proposed solutions in Section V.
4) *Synchronization algorithms:* Considering that a LoRa frame has a specific pattern of CSS symbols before the payload part, after receiving a LoRa frame at the receiver, the first step is to detect the preamble part and perform synchronization. In most practical cases, a CSS receiver must compensate for carrier frequency offsets (CFO) and sampling time offsets (STO). Inexpensive crystal oscillators inherently exhibit a discrepancy from their intended frequency value. As a result, the process of down-conversion takes place using a frequency different from that used for up-conversion. In the context of CSS signals, this results in CFO and is revealed as a shift in the swept BW of the CSS signal regenerated at the receiver and can be introduced as a multiply of a CSS signal frequency bin, e.g., a shift of 4.1 frequency bins [58]. On the other hand, when the receiver's clock for sampling the received signal is not perfectly synchronized with the transmitter's clock, it leads to misalignment in the sampling instants. So the regenerated CSS signal at the receiver experiences a shift in the time domain compared to the transmitted version. The STO can be measured as a shift equal to the multiply of a CSS sample, e.g., a shift of 4.1 samples [58]. Large synchronization errors can cause significant interference between chirps, resulting in unreliable detection performance. Currently, there is limited research on synchronization in the context of CSS modulation. In Section VI, we review the effects of each of the mentioned factors on the CSS signal and review the current synchronization procedure during a LoRa packet transmission. Moreover, existing key works on various proposed synchronization algorithms are discussed.

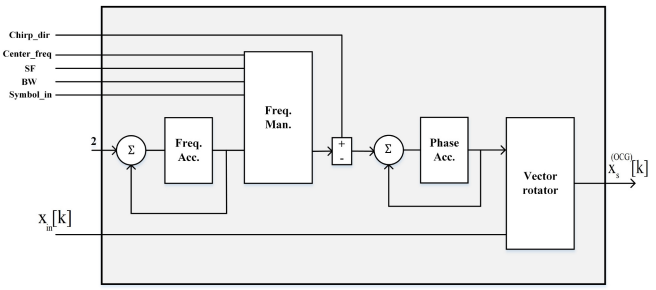

FIGURE 16. Orthogonal chirp generator of [21].

III. KEY ADVANCES IN TRANSCEIVER CONFIGURATION AND DESIGN

In this section, we review key works that aim to improve the implementation and signal detection of CSS-based communication systems [21], [52], redesign CSS signal transmission for adoption in satellite-based IoT scenarios [59], [60], [61], [62], [63], and propose a new MIMO-CSS configuration [64], [65].

A. IMPLEMENTATION AND SIGNAL DETECTION

Nguyen et al. in [21] present the orthogonal chirp generator (OCG), a low-cost CSS transmitter architecture that supports various SF and BW settings. Because of the flexibility of the OCG, it may be used to not only generate complex baseband or real pass-band signals at the transmitter but also to demodulate the chirp signal at the receiver. The expression for the phase function allowing the OCG to generate the CSS signal is:

$$\phi_s^{(\mathrm{OCG})}[k] = \frac{1}{2ML^2}\sum_{n=0}^{k}[(2n+1+2sL) \mod (2ML)] - ML, \quad k = 0, 1, \ldots, ML-1 \tag{54}$$

where L is the up-sampling factor, i.e., $f_s^{(\mathrm{up})} = L \times \mathrm{BW}$. The OCG block diagram is shown in Figure 16. As can be seen, the frequency accumulator, frequency manipulator, phase accumulator, and vector rotator are the four primary components. The first three components generate the phase function as in (34). The frequency accumulator generates a ramp, i.e., a frequency that increases linearly over time. According to the input symbol s, the selected BW, and SF, the frequency manipulator introduces jumps into the frequency ramp at the symbol boundaries. To provide phase samples for the created chirp symbol, the phase accumulator conducts discrete integration of the frequency samples. Eventually, the vector rotator rotates an input vector $x_{\mathrm{In}}[k]$ by an amount of $\phi_s^{(\mathrm{OCG})}[k]$ as follows:

$$x_s^{(\mathrm{OCG})}[k] = x_{\mathrm{In}}[k]\exp\left(j2\pi\phi_s^{(\mathrm{OCG})}[k]\right). \tag{55}$$

To obtain a continuous phase CSS signal, $x_{\mathrm{In}}[k]$ is set to a scalar determined by the CSS signal transmitting power.

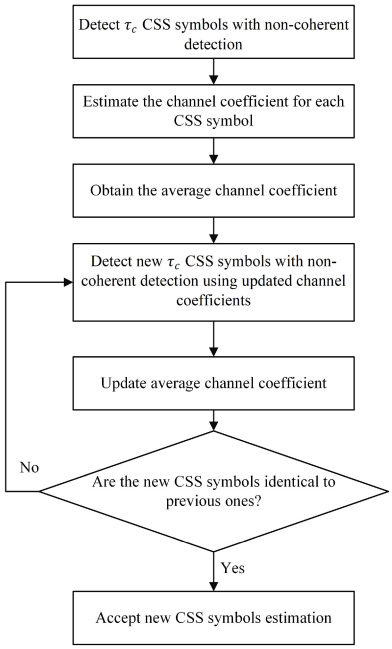

FIGURE 17. Semi-coherent detection algorithm flowchart of [52].

Otherwise, in a case that the continuous phase is not required between two adjacent CSS symbols, $x_{\text{In}}[k]$ can carry extra information as its phase. To upconvert the CSS signal to the passband, the OCG can be used in conjunction with a quadrature modulator. Also, direct digital synthesis (DDS) technology can be utilized to lower the cost of the up-converter. Moreover, an OCG-based receiver structure is presented which by means of simulation, is shown to have a much better performance than Semtech's receiver. The SNR enhancement ranges from 0.9 dB at SF $= 6$ to a remarkable 2.5 dB at SF $= 12$ for a packet error rate (PER) of 10^{-2}.

Using signal combining and semi-coherent detection, Nguyen et al. in [52] offer a performance improvement strategy for CSS modulation. In their system model, the gateway is assumed to have multiple antennas rather than a single antenna. According to BER results of signal combining methods at LoRa gateways, appropriately integrating diverse incoming signals at the gateway can considerably improve CSS modulation performance, resulting in reduced transmit power and/or improved coverage for EDs. The authors also present a novel iterative semi-coherent detection strategy that outperforms non-coherent detection, especially as the number of antennas at the gateway increases. The term "semi-coherent" is used due to the fact that there is no extra overhead used for channel estimation, i.e., the channel is estimated using different versions of the same CSS signal all carrying information. The flowchart of the semi-coherent detection algorithm is indicated in Figure 17. It is assumed that the fading channel has a coherence time equal to τ_c times a single CSS symbol duration. When the system operates over AWGN (coherent) and Rayleigh fading (non-coherent) channels, simulation results show that increasing the number of antennas at the gateway from 1 to 4 results in approximately 8 and 29 dB savings in transmit power of the IoT ED (which translates to 2.5 times and 27 times larger distances for the same transmit power of the device). Moreover, the results show that the semi-coherent detection BER performance is close to the coherent case (the difference is smaller than 1 dB).

B. SATELLITE-BASED IOT SCENARIOS

For the application of the CSS modulation in satellite-based IoT, there are several challenges such as the effect of the Doppler shift, and the interference rejection if the network becomes dense (due to the high coverage of the satellites). Doroshkin et al. present an experimental study of CSS modulation in [59] to evaluate its robustness against the Doppler effect in LEO satellite IoT scenarios. The laboratory experiments conducted in this paper showed that the CSS modulation has high resistance to static Doppler shift (the value of the shift does not vary with time) for all SF values, while its robustness against dynamic Doppler shift (the value of the shift varies with time) highly depends on the SF value. As the SF increases, the maximum tolerable Doppler rate decreases. The outdoor experiments, where the CSS receiver was installed in a moving car, fully confirmed the results of the laboratory experiments. Finally, the experiments showed that the CSS modulation can be used in radio communication between the ground station and a satellite in a circular orbit of more than 550 km in height without any restrictions associated with the Doppler effect.

Qian et al. in [60] modify the CSS modulation and propose symmetry chirp signal (SCS) to be more compatible with dense satellite-base IoT deployment in which the interference at the CSS receiver may be much larger than terrestrial scenarios. It is shown that when the difference between the starting frequency offsets of two chirps tends to zero or BW, the cross-correlation of the two chirps is large with a value close to CSS signal energy and its maximum value cannot be lower than half of CSS signal energy. Based on the fact that the cross-correlation between chirps with negative and positive rates is relatively small, the authors introduce SCS in which T_{sym} is divided into two equal periods consisting of up- and down-chirp signals respectively. Based on this modification, the resulting instantaneous frequency offset of Figure 4 changes to the curve in Figure 19. After evaluation of the SCS cross-correlation features, it can be seen that the SCS can obtain a maximum cross-correlation of less than half of the signal energy. Also, the authors investigate the effect of the Doppler frequency shift (DFS) on the SCS modulation scheme in [61] which results in a high ambiguity function (AF) value. Therefore, an asymmetry chirp signal (ACS) is obtained as a solution for the optimization of AF. Using simulation, it has been shown that ACS can achieve better BER and acquisition performance compared to SCS in the presence of DFS.

Roy et al. [62] design a new set of chirps namely symmetry chirp with multiple chirp rates (SC-MCR) to reduce the

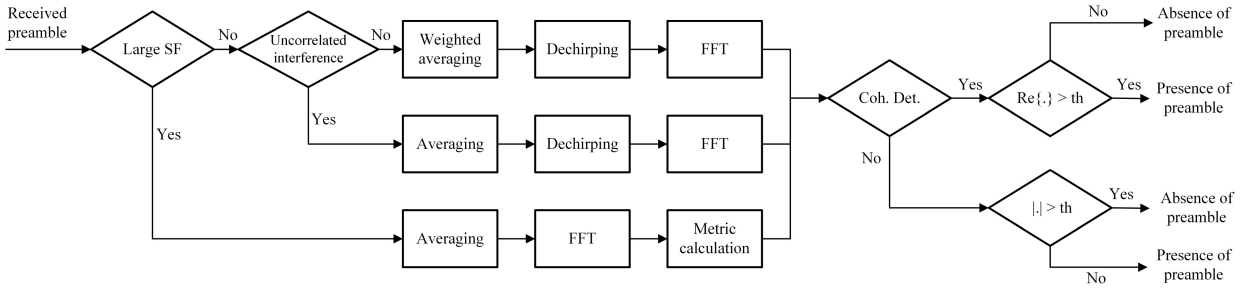

FIGURE 18. Preamble detection algorithm of [66].

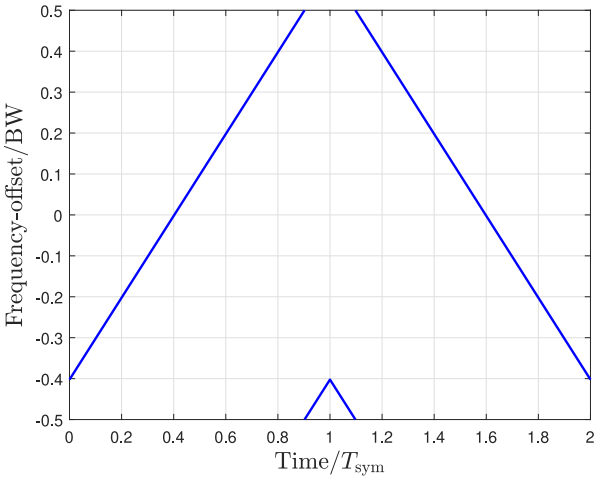

FIGURE 19. SCS instantaneous frequency-offset for $s = 50$, SF = 9, BW = 250 kHz, and $T_{sym} = 2.048$ ms.

overall cross-correlation level caused by possible delays in LEO satellite communication. The main difference between SC-MCR and SCS is to use different chirp rates for each half of the $T_{sym}/2$ period. It is shown that the cross-correlation of SC-MCR is lower than the SCS method. Thus, for a multiuser communication scenario, SC-MCR provides less multiple access interference (MAI) compared to SCS. Further, the combination of up-SC-MCR and down-SC-MCR through time domain multiplexed SC-MCR (TDM SC-MCR) is presented which allows an increase in the overall system data rate without much degradation in performance. Thus, SC-MCR waveforms are able to provide a more reliable LEO satellite IoT communication and maintain a higher data rate compared to that of SCS waveforms.

Yang et al. in [63] introduce folded chirp-rate shift keying (FCrSK) modulation for the application in satellite-based IoT networks. The authors discuss two common problems existing in chirp-rate shift keying systems. First, for chirp signals with identical T_{sym}, different chirp rates can be achieved using different BWs which results in different spreading gains. To avoid sampling distortion, the sampling rate must be set to handle the largest rate existing among chirp signals. This translates to an increase in the burden on analog-to-digital converter (ADC). Second, identical signals with chirp rates resulted in different T_{sym}s making the symbol synchronization a challenging task at the receiver. To deal with these issues, folded chirp waveform (FCW) is proposed as:

$$x^{(\mathrm{FCW})}(t) = A_0 \sum_{n=0}^{n_c-1} \exp\left(j\pi \frac{\mathrm{BW}}{T_c} t^2 - 2j\pi n \mathrm{BW} t\right) \times g_{T_c}(t - nT_c), \tag{56}$$

where the complete FCW is combined of n_c chirp-chips each has a duration of T_c ($n_c T_c = T_{sym}$). The block diagram of the complete FCrSK system is indicated in Figure 20. After converting the binary data into the decimal value of $s \in \mathcal{S}$ similar to CSS modulation, the results are mapped into one FCW out of M possible waveforms using the following equation:

$$x^{(\mathrm{FCW})}(t, s) = A_0 \sum_{n=0}^{n_c-1} \exp\left(j\pi s \frac{\mathrm{BW}}{T_{sym}} t^2 - 2j\pi n \mathrm{BW} t\right) \times g_{T_c}(t - nT_c). \tag{57}$$

Followed by dechirping and M-point DFT procedures, the decision is made based on frequency peak average rate (FPAR) which is insensitive to the Doppler effect. Due to the interference between distinct chirp rates, FCrSK performs somewhat worse than the CSS modulation without Doppler shift, however, FCrSK outperforms CSS modulation against large Doppler shift or large Doppler rate, as demonstrated by simulation and experimental data. Moreover, it can maintain a sufficient BER without frequency synchronization even when Doppler is very large and Doppler variation is very fast making it appropriate for satellite-based IoT applications.

C. MIMO-CSS

To tackle the issue of poor performance of CSS modulation in the presence of fading, Ma et al. in [64] propose a novel MIMO configuration exploiting space-time block coding (STBC). The authors consider a $N_t \times N_r$ MIMO system in which the CSS symbols are coded with a complex orthogonal STBC transmission $U_c \times N_t$ matrix. Note that this matrix is utilized to encode J_c input symbols ($J_c \geq 2$) into an N_t-dimensional vector sequence of U_c time slots, with the transmission rate of J_c/U_c. The encoding algorithm for STBC-MIMO CSS is summarized in the following steps:

1) Initializing N_t and SF.
2) Performing CSS modulation on information data bits.

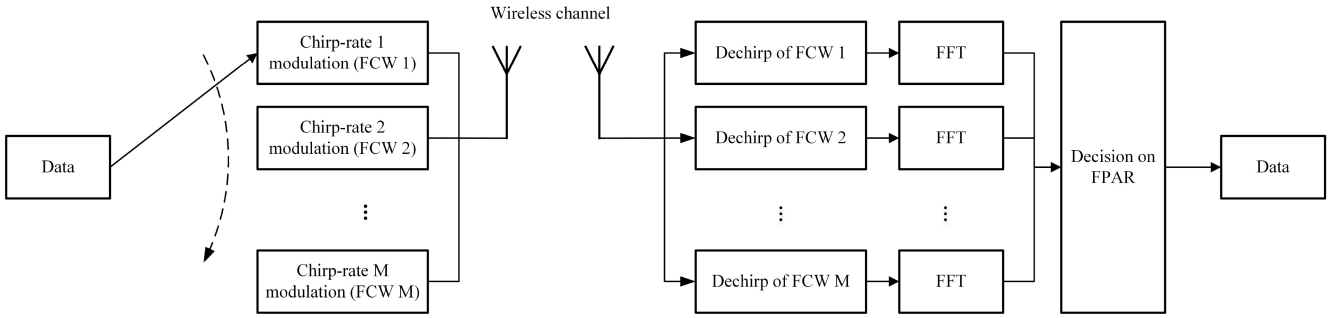

FIGURE 20. FCrSK transceiver block diagram [63].

3) Selecting the STBC transmission matrix $(U_c \times N_t)$ and generating the matrix $\Im_{U_c \times N_t M}$ which its entries are linear combinations of transmitted CSS symbols and their conjugates.
4) Transmitting CSS signals in the u_cth row, $[(n_t-1)M+1]$th column to $n_t M$th column of $\Im$ via n_tth antenna $(1 \leq n_t \leq N_t)$, for each time-slot $1 \leq u_c \leq U_c$

At the receiver end, the decoding algorithm consists of the following steps:

1) Initializing N_r and SF.
2) Performing channel estimation exploiting CSS preamble (the authors assume both cases of perfect and imperfect CSI).
3) Canceling the channel effect from the received signal in each time slot for each antenna in a symbol-by-symbol manner.
4) Summing up the resulted signals over all time-slots and antennas for each symbol.
5) Performing CSS demodulation.

From the simulation results provided in [64], it can be seen that the use of the STBC-MIMO scheme can considerably improve the diversity gain of the CSS-based communication system. Moreover, as an example, the STBC-MIMO CSS with 2 transmit antennas and one receiver antenna outperforms conventional CSS modulation by 16 dB at the BER of 10^{-4} in the perfect CSI scenario.

Kang in a short paper [65] present the concepts and precoding design for MIMO-based CSS modulation with the application in high data rate IoT scenarios. Figure 21 depicts the proposed configuration. A CSS signal is carried by each transmit antenna with different SF to prevent interference among the CSS signals. Considering that conventional CSS modulation can carry SF bits in each symbol, the MIMO-CSS configuration conveys $\sum_{i=1}^{N_t} \mathrm{SF}_i$ bits. In the second part of the paper, the authors also present a precoding design by maximizing the received SNR with total and peak transmit power constraints. Based on this scheme, the number of information bits slightly reduces precoding. The suggested MIMO-CSS system greatly outperforms the standard CSS modulation in terms of BER and effective data rate, according to simulation results. Moreover, Kang and Choi [67] provide effective demodulation techniques, both

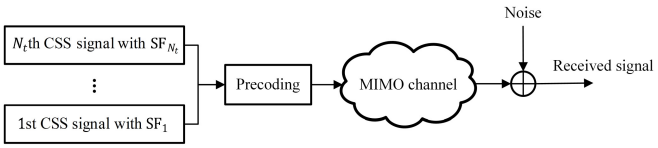

FIGURE 21. MIMO-CSS system model of [65].

coherent and non-coherent, for the MIMO-LoRa system by leveraging the advantageous properties of modulated chirps over multiple antennas. In addition, the authors evaluate the computational difficulties of these algorithms and demonstrate their usefulness using numerical simulations.

D. KEY INSIGHTS

So far in this section, we investigated the recent key works regarding the advances in transceiver configurations for CSS modulation. The followings are the key insights inferred from the existing works:

- Despite having the highest value for SF as 12 in today's LoRaWAM specifications, the LUT-based design of the CSS transmitter can result in high memory consumption in the near future. As an example, for SF = 16, the size of the required LUT would be 65536×65536. Therefore, the OCG design presented in [21] seems like an interesting low-cost replacement at the industrial level as it eliminates the need for CSS signal generation based on an LUT.
- Exploiting multiple antennas at the gateway improves the BER performance of CSS modulation due to spatial diversity at the receiver. As an example, for SF = 10 and BER of 10^{-4}, this improvement equals to almost 6 dB for AWGN channel and coherent detection. Moreover, with the help of multiple antennas at the receiver, the channel estimation can be performed without additional signal overhead resulting in a better performance than non-coherent detection schemes [52].
- Application of CSS modulation in its current for satellite-based IoT networks may not result in favorable performance due to the massive number of IoT EDs served by a single satellite [60]. Compared to CSS and SCS modulations, ACS modulation can deliver better

BER performance in the presence of DFS which is the case in satellite-based IoT scenarios [61].

- SC-MCR modulation provides more reliable LEO satellite IoT communication and achieves higher data rates compared to SCS [62]. Modified chirp-rate modulation of FCrSK outperforms CSS modulation in the presence of large Doppler shifts or large Doppler rate [63].
- The Concept of MIMO communication can be integrated with CSS modulation to overcome challenges such as poor fading performance and low data rate transmission of conventional CSS modulation [64], [65]. This can unlock various applications for CSS modulation in the context of high data rate IoT, Moreover, the multiple antennas at the receiver can significantly improve the BER and increase the communication range of LoRaWAN resulting in a more suitable communication scheme for remote areas.

IV. KEY ADVANCES IN DATA RATE IMPROVEMENT

As mentioned, long-range communication provided by CSS modulation techniques comes with the cost of very low data rates in the order of a few hundred to a few thousand bits per second. Although this is suitable for most of the smart city applications in IoT networks, efforts have been made to improve the data rate of CSS-based transmission schemes. In the following, recent key advances [25], [26], [41], [42], [43], [68], [69], [70], [71], [72], [73], [74], [75] on this topic are discussed in detail.

Elshabrawy and Robert [68] propose a technique called interleaved chirp spreading LoRa (ICS-LoRa) with the aim of improving data rates in LoRa networks. This approach results in doubling the size of the signal set, i.e., adding 1 additional bit per symbol compared to the conventional encodable information data with the same BW. The interleaved version of the CSS signal discrete-time frequency-offset $\Delta f_s[k]$ can be formulated as follows:

$$\Delta f_s^{(\mathrm{I})}[k] = \begin{cases} \Delta f_s[k], & 0 \le k < 2^{\mathrm{SF}-2}, \\ \Delta f_s[k + 2^{\mathrm{SF}-2}], & 2^{\mathrm{SF}-2} \le k < 2^{\mathrm{SF}-1}, \\ \Delta f_s[k - 2^{\mathrm{SF}-2}], & 2^{\mathrm{SF}-1} \le k < 3 \times 2^{\mathrm{SF}-2}, \\ \Delta f_s[k], & 3 \times 2^{\mathrm{SF}-2} \le k < 2^{\mathrm{SF}}. \end{cases} \quad (58)$$

Figure 22 illustrates these interleaving performed on the discrete-time version of the same CSS signal frequency offset of Figure 4. Based on this technique, the transmitter input is a bit vector of the length $\mathrm{SF}+1$. That is because instead of M possible CSS waveforms in conventional LoRa, there are also M interleaved versions of CSS waveforms and $\log 2M = \log M + \log 2 = \mathrm{SF}+1$. This extra bit (considered a less significant bit of the input vector [68]) is used at the transmitter to decide whether a conventional CSS signal or the interleaved version should be used to transmit the remaining SF bits. By applying the SE formula as $\eta = r_b/\mathrm{BW}$ (r_b is the bit rate), the SE of ICS-LoRa is $\eta^{(\mathrm{ICS-LoRa})} = (\mathrm{SF}+1)/M$ bit/s/Hz. At the receiver end, the received samples and the interleaved samples undergo signal dechirping. Subsequently, both dechirped signals are fed into DFT blocks to produce two resulting vectors. The ICS-LoRa detector then generates an estimated bit indicating whether the normal CSS or interleaved version is sent, along with an estimated non-binary symbol. The results of the BER performance indicate that for an SF of 7, the increased capacity of interleaved CSS comes with a slight degradation in BER performance, equivalent to a 0.8 dB gap. However, for higher SFs, the capacity advantages can be achieved with minimal impact on BER performance compared to the standard CSS modulation. Inspired by ICS-LoRa, Liu et al. in [76] propose a maximum limit for approximating CSS signaling BER and present a Block ICS-LoRa (BCIS-LoRa) strategy to improve BER performance over Multi-Path Channels (MPCs). Experimental results show that BICS-LoRa can significantly improve performance and is simple to deploy with minimum complexity, making it suited for channels with high multipath interference due to short delay times or large SF values.

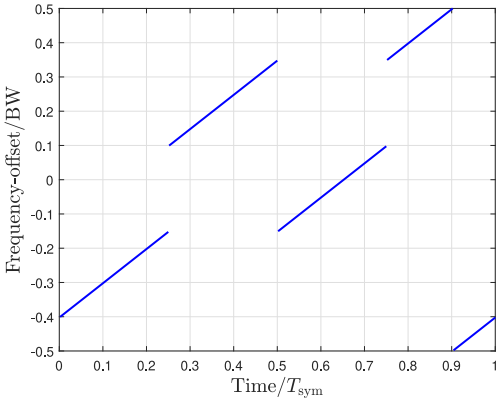

FIGURE 22. ICS-LoRa instantaneous frequency offset of CSS signal for $s = 50$, $\mathrm{SF} = 9$, $\mathrm{BW} = 250$ kHz, and $T_{\mathrm{sym}} = 2.048$ ms.

Hanif and Nguyen [25] propose slope-shift keying LoRa (SSK-LoRa) in which down-chirps are used instead of interleaved ones. It is indicated in [25] that because of the non-orthogonality between the interleaved chirps and the conventional ones, the ICS-LoRa scheme hurts the performance in terms of BER. The SSK-LoRa is performed by using M up-chirps and M down-chirps for a symbol. Therefore, one more bit can be carried by this method similar to the ICS-LoRa approach. Similar to the ICS-LoRa, the SE of SSK-LoRa is $\eta^{(\mathrm{SSK-LoRa})} = (\mathrm{SF}+1)/M$ bit/s/Hz. It should be noted that the sets of chirps used in SSK-LoRa are not also perfectly orthogonal and therefore, BER is slightly degraded compared to conventional CSS. But, as provided in the simulation part of this paper, the achievable rate is high enough to be able to neglect this degradation.

Almeida et al. propose an in-phase and quadrature (IQ) CSS technique in [41]. IQ-CSS exploits both IQ axes to convey two superposed CSS signals. This enables encoding 2SF total bits, SF bits in the in-phase component, and SF bits

in the quadrature component. The IQ-CSS symbol waveform is formed as

$$x^{(\mathrm{IQ})}[k] = \frac{1}{\sqrt{2}}\left(x_{s_\mathrm{I}}^{(\mathrm{NC}))}[k] + jx_{s_\mathrm{Q}}^{(\mathrm{NC})}[k]\right), \tag{59}$$

in which $x_{s_\mathrm{I}}^{(\mathrm{NC}))}[k]$ (in-phase component) and $x_{s_\mathrm{Q}}^{(\mathrm{NC})}[k]$ (quadrature component) are non-continuous phase CSS signals encoding two information symbols s_I and s_Q, respectively. The M^2 resulting waveforms from (59) are not orthogonal, but it is shown that the two symbols s_I and s_Q can be independently decoded using coherent detection, each one similar to an orthogonal LoRa system. Clearly, the bit rate of IQ-CSS is doubled with respect to LoRa, at the same bandwidth. Thus, the SE of IQ-CSS is $\eta^{(\mathrm{IQ-CSS})} = 2\mathrm{SF}/M$ bits/s/Hz.

Xie et al. propose dual chirp direction shift keying (DCDSK) [77]. According to this scheme, the transmitted waveform is a superposition of dual CSS up-chirps or dual CSS-down chirps as:

$$x^{(\mathrm{DCDSK})}[k] = \begin{cases} x_{s_1}^{(\mathrm{NC}))}[k] + x_{s_2}^{(\mathrm{NC})}[k], \text{ if } s_1 \le s_2, \\ x_{\mathrm{D},s_1}^{(\mathrm{NC}))}[k] + x_{\mathrm{D},s_2}^{(\mathrm{NC})}[k], \text{ if } s_1 > s_2, \end{cases} \tag{60}$$

where s_1 and s_2 are the decimal equivalent of first and second SF bits of a bit sequence with the length $2 \times \mathrm{SF}$ bits, respectively. Hence, the SE of DCDSK is $\eta^{(\mathrm{IQ-CSS})} = 2\mathrm{SF}/M$ bits/s/Hz.

Discrete chirp rate keying CSS (DCRK-CSS), proposed by de Almeida et al. [70] further extends the waveform set of IQ-CSS using multiple up-chirps and down-chirps via IQ structure with different chirp rates. This scheme uses N_c additional bits to encode 2^{N_c} different chirp rates as $R' \in \{\pm 1, \pm 2, \ldots, \pm 2^{N_c-1}\}$. Hence, the DCRK-CSS waveform can be written as:

$$x^{(\mathrm{DCRK})}[k] = A_0 \exp\left[2\pi j \frac{R'(k+s)^2 - M(k+s)}{2M}\right]. \tag{61}$$

Therefore, the SE of DCRK-CSS is $\eta^{(\mathrm{DCRK\text{-}CSS})} = (\mathrm{SF} + N_c)/M$ bit/s/Hz. It should be noted that the received DCRK-CSS signal goes through a bank of dechirping modules with different chirp rates in order to estimate R' used in the transmitter.

Phase shift keying-LoRa (PSK-LoRa), as proposed by Bomfin et al. [69], aims to improve the SE of LoRa by modifying its waveform assignment. In PSK-LoRa, instead of using only SF bits for each waveform, $\mathrm{SF} + N_p$ bits are assigned, where N_p represents the number of phase-shift bits. The concept involves extending the existing set of M LoRa waveforms by introducing an additional set of $(2^{N_p} - 1)M$ waveforms that share the same chirps but have a phase shift that is a multiple of $\pi/2^{N_p-1}$. The bit rate in PSK-LoRa is then equal to $r_b = (\mathrm{SF} + N_p)f_s/M$, while the bandwidth remains unchanged compared to LoRa. The SE of PSK-LoRa can be calculated as:

$$\eta^{(\mathrm{PSK\text{-}LoRa})} = \frac{\mathrm{SF} + N_p}{M} \quad \text{bits/s/Hz}. \tag{62}$$

By choosing $N_p = 1$, PSK-LoRa is reduced to BPSK-LoRa which has a waveform as follows:

$$x^{(\mathrm{BP})}[k] = A_0 A_{\mathrm{BP}} \exp\left[2\pi j \frac{(k + \lfloor \frac{s}{2} \rfloor)^2 - M(k + \lfloor \frac{s}{2} \rfloor)}{2M}\right], \tag{63}$$

where $A_{\mathrm{BP}} = [1 - 2(s \mod 2)]$ and $(s \mod 2)$ is the bit that determines the sign of the up-chirp. Similarly, for $N_p = 2$, we will achieve the QPSK-LoRa waveform as:

$$x^{(\mathrm{QP})}[k] = A_0 A_{\mathrm{QP}} \exp\left[2\pi j \frac{(k + \lfloor \frac{s}{4} \rfloor)^2 - M(k + \lfloor \frac{s}{4} \rfloor)}{2M}\right], \tag{64}$$

where $A_{\mathrm{QP}} = A_{\mathrm{BP}} + j[1 - 2(\lfloor s/2 \rfloor \mod 2)]$. The detection of PSK-LoRa is performed in two steps, i.e., first, using a conventional CSS detector, the information embedded in CSS part is decoded, and in the second step, the phase estimate is obtained by applying the ML PSK estimator. After derivation of the approximate BER for PSK-LoRa in AWGN and Rayleigh channels, the results in [69] show that in certain scenarios, PSK-LoRa offers the capability to transmit an equivalent amount of data as LoRa, but in a more efficient manner that saves time resources. Consequently, implementing PSK-CSS modulation in LPWAN can be advantageous in reducing energy consumption, which is a significant issue for these systems.

The index modulation (IM) technique is considered as one of the most recent approaches deployed in various modulation techniques for data rate improvement purposes [78]. A similar approach to use IM in CSS modulation is presented in Zhang and Liu's work [79] and Yoon et al. work [80]. In these works, basic time-delayed up-chirps are transmitted in multiple manners with the basic up-chirp, and the information bits are embedded in the phase and/or the amplitude. The difference between these schemes and IM-based methods is that in IM, information bits are encoded in the signal indices, which, in the case of CSS modulation, correspond to the initial phase and frequency of up-chirps. In [26], Hanif and Nguyen propose integrating IM with CSS resulting in a technique called frequency shift chirp spread spectrum with index modulation (FSCSS-IM). In FSCSS-IM, IM is integrated with CSS modulation similar to the case of IM application in the frequency bins of orthogonal frequency-division multiplexing (OFDM) [81]. However, in OFDM-IM, a fraction of BW is allocated to each symbol, but in FSCSS-IM, each symbol occupies the whole available BW. The FSCSS-IM waveform is formed as the summation of W different CSS waveforms, each encoding the information symbols s_w ($w = 0, 1, \ldots W$). Therefore, the waveform of FSCSS-IM can be formulated as:

$$x^{(\mathrm{IM})}[k] = \frac{1}{\sqrt{W}} \sum_{w=0}^{W-1} x_w[k]. \tag{65}$$

Based on this, the number of bits that can be carried by a single FSCSS-IM signal is $N_b^{(\mathrm{IM})} = \lfloor \log_2 \binom{M}{W} \rfloor$. It is

worth noting that two FSCSS-IM symbols are orthogonal if the CSS orthogonality conditions hold for any one-by-one combination of their individual CSS signals. Moreover, the SE of FSCSS-IM is $\eta^{(\mathrm{IM})} = N_b^{(\mathrm{IM})}/M$ bits/s/Hz. When multiple chirps are combined and utilized for signal transmission to enhance the data rate, the optimal receiver would necessitate searching through all the patterns employed by the transmitter. There is also a suboptimal receiver proposed in [26] to overcome this issue. From the simulation results provided in [26], it can be observed that FSCSS-IM has an acceptable performance compared to CSS in terms of BER.

As an extended approach resulting from the combination of FSCSS-IM and IQ-CSS methods, Baruffa and Rugini in [42] present an approach to enhance CSS waveforms called in-phase and quadrature chirp index modulation (IQCIM). In fact, the IQCIM waveform is formed as the sum of two FSCSS-IM signals as in-phase and quadrature parts. Hence, the waveform of IQCIM can be written as:

$$x^{(\mathrm{IQCIM})}[k] = \frac{1}{\sqrt{2}}\left(x_{\mathrm{NC}}^{(\mathrm{IM,I})}[k] + jx_{\mathrm{NC}}^{(\mathrm{IM,Q})}[k]\right). \tag{66}$$

The bit rate of IQCIM is double the bit rate of FSCSS-IM with the same value of W and for the same bandwidth. Thus, the SE in IQCIM is $2\eta^{(\mathrm{IM})}$ bits/s/Hz. Based on the performance analysis, it has been observed that the IQCIM offers a notable improvement in SE compared to CSS while maintaining a similar level of complexity. This enhanced efficiency comes at a marginal energy cost of approximately 0.9 dB.

Ma et al. in [71] propose frequency-bin-index LoRa (FBI-LoRa) via two schemes for data rate improvement of CSS modulation. In scheme I, the CSS symbol set $\mathcal{S}$ is divided into g_{num} groups where the number of CSS symbols in each group is $N_g = M/g_{\mathrm{num}}$. Then, the summation of N_{sum} symbols, which are equally taken from each group, is selected to shape the CSS waveform. Therefore, the number of selected symbols from each group is $f_{\mathrm{num}} = N_{\mathrm{sum}}/g_{\mathrm{num}}$. Based on these, the waveform of the FBI-LoRa scheme I can be written as:

$$x^{(\mathrm{FBI_I})}[k] = \sum_{i=0}^{g_{\mathrm{num}}-1}\sum_{i'=0}^{f_{\mathrm{num}}-1} A0\sqrt{\frac{M}{f_{\mathrm{num}}g_{\mathrm{num}}}} \times \exp\left[2\pi j\frac{(k+s_{i,i'})^2 - M(k+s_{i,i'})}{2M}\right], \tag{67}$$

where $s_{i,i'}$ represent the i'th CSS symbol in ith group. The SE of FBI-LoRa scheme I can be obtained as $\eta^{\mathrm{FBI_I}} = g_{\mathrm{num}}\lfloor \log_2\binom{N_g}{f_{\mathrm{num}}}\rfloor/M$ bit/s/Hz. In scheme II, the groups are indexed, and g'_{num} groups out of total g_{num} groups are selected ($1 \le g'_{\mathrm{num}} < g_{\mathrm{num}}$). Therefore, the number of symbols in each selected group is $f'_{\mathrm{num}} = N_{\mathrm{sum}}/g'_{\mathrm{num}}$ and the vector of selected groups is denoted as $\{\mathrm{Grp}(0), \mathrm{Grp}(1), \ldots, \mathrm{Grp}(g'_{\mathrm{num}} - 1)\}$. Therefore, the waveform of FBI-LoRa scheme II can be formulated as:

$$x^{(\mathrm{FBI_{II}})}[k] = \sum_{i=0}^{g'_{\mathrm{num}}-1}\sum_{i'=0}^{f'_{\mathrm{num}}-1} A0\sqrt{\frac{M}{f'_{\mathrm{num}}g'_{\mathrm{num}}}} \times \exp\left[2\pi j\frac{(k+s'_{i,i'})^2 - M(k+s'_{n,i,i'})}{2M}\right], \tag{68}$$

where $s'_{i,i'}$ is the i'th CSS symbol in group $\mathrm{Grp}(i)$. The SE of the FBI-LoRa scheme II is then

$$\eta^{\mathrm{FBI_{II}}} = \frac{1}{M}\left(g'_{\mathrm{num}}\left\lfloor \log_2\binom{N_g}{f'_{\mathrm{num}}}\right\rfloor + \left\lfloor \log_2\binom{g_{\mathrm{num}}}{g'_{\mathrm{num}}}\right\rfloor\right) \text{ bit/s/Hz.} \tag{69}$$

Additionally, the theoretical analyses and simulations show that the FBI-LoRa system surpasses conventional CSS, ICS-LoRa, SSK-LoRa, and PSK-LoRa systems, albeit with a minor compromise in the BER performance.

To improve the PSK-LoRa scheme, Azim et al. in [72] propose enhanced PSK-LoRa (ePSK-LoRa) to increase the CSS modulation data rate and make it more energy efficient. Based on this approach, the BW of CSS modulation is divided into N_{sub} subbands, where, each one contains M/N_{sub} CSS symbols (it is equivalent to dividing the set $\mathcal{S}$ into N_{sub} subsets). Calling the starting frequencies of CSS modulation in the first subband as fundamental frequencies (FF), one can encode $\log_2(M/N_{\mathrm{sub}})$ bits by selecting an FF. Then, the redundancy is generated by selecting the harmonics of the selected FF (f_{sel}) in all N_{sub} subbands as $f_{\mathrm{sel}} + M/N_{\mathrm{sub}}$, $f_{\mathrm{sel}} + 2M/N_{\mathrm{sub}}$, $\ldots$, and $f_{\mathrm{sel}} + (N_{\mathrm{sum}} - 1)M/N_{\mathrm{sum}}$. After this, FF and its harmonics are multiplied by a phase shift coefficient as $\exp(2\pi jpl/2^{N_{\mathrm{PS}}})$ where N_{PS} is the number of bits encoded into the phase shifts and $l \in [[0, N_{\mathrm{sum}} - 1]]$ is the index of the subband. Based on these, the ePSK-LoRa waveform can be formulated as:

$$x^{(\mathrm{ePSK})}[k] = \sum_{l=0}^{N_{\mathrm{sub}}-1} \exp\left(\frac{2\pi j[f_{\mathrm{sel}} + l(M/N_{\mathrm{sub}})]k}{M}\right) \times \exp\left(\frac{2\pi jpl}{2^{N_{\mathrm{PS}}}}\right)x_0[k]. \tag{70}$$

Therefore, the SE of ePSK-LoRa is $\eta^{(\mathrm{ePSK})} = (1/M)[\log_2(M/N_{\mathrm{sub}}) + N_{\mathrm{sub}}N_{\mathrm{PS}}]$ bit/s/Hz. Based on the provided results, ePSK-LoRa offers appealing characteristics compared to traditional alternatives, including satisfactory resilience to both phase offset and frequency offset.

Yu et al. present a group-based CSS (GCSS) modulation in [73] in order to improve the SE of CSS modulation. Based on this approach, the set of $\mathcal{S}$ is divided into GN groups resulting in $K = \log_2(M/GN)$ transmittable information bits per group. Therefore, the total number of $N_s = GN \times K$ bits can be modulated for all GN groups. Based on this, every N_s information bits are divided into groups of $b^{(m)} =$

$[b_0^{(m)}, b_1^{(m)}, \ldots, b_{K-1}^{(m)}]$ where $m \in \{1, 2, \ldots, GN\}$ and the mapping symbol $s^{(m)}$ is generated as:

$$s^{(m)} = (m-1)\frac{M}{GN} + \sum_{i=0}^{K-1} b_i^{(m)} 2^i. \tag{71}$$

Finally, the GCSS waveform can be formulated as:

$$x^{(\mathrm{GCSS})}[k] = A_0 \sqrt{\frac{1}{GN}} \times \sum_{m=1}^{GN} \exp\left[2\pi j \frac{(k+s^{(m)})^2 - (k+s^{(m)})}{2M}\right]. \tag{72}$$

The SE of GCSS is then obtained as $\eta^{(\mathrm{GCSS})} = GN \times K/M$ bit/s/Hz.

Time domain multiplexed LoRa (TDM-LoRa) is another data rate improvement technique proposed by An et al. in [43]. The basic idea of this approach is to form the TDM-LoRa waveform based on a CSS up-chirp and a CSS down-chirp as:

$$x^{(\mathrm{TDM})}[k] = \sqrt{\frac{1}{2}}\left(x_{s_1}^{(\mathrm{NC})}[k] + x_{s_1,\mathrm{D}}^{(\mathrm{NC})}[k]\right). \tag{73}$$

Hence, the SE of TDM-LoRa is $\eta^{(\mathrm{TDM})} = 2\mathrm{SF}/M$ bit/s/Hz. Moreover, an IQTDM-LoRa is also proposed in which in-phase and quadrature components are TDM-LoRa waveforms. The SE of IQTDM LoRa can be written as $\eta^{(\mathrm{IQTDM})} = 4\mathrm{SF}/M$.

Inspired by ICS-LoRa and SSK-LoRa, Mondal et al. propose SSK-ICS-LoRa in which the signal set includes CSS up-chirps, down-chirps, interleaved up-chirps, and interleaved down-chirps. Building upon this, the SSK-ICS-LoRa waveform has the following form:

$$x_s^{(\text{SSK-ICS})}[k] = \begin{cases} x_s^{(\mathrm{NC})}[k], & 0 \le s < M, \\ x_{s,\mathrm{D}}^{(\mathrm{NC})}[k], & M \le s < 2M, \\ x_s^{(\mathrm{I})}[k], & 2M \le s < 3M, \\ x_{s,\mathrm{D}}^{(\mathrm{I})}[k], & 3M \le s < 4M, \end{cases} \tag{74}$$

where $x_s^{(\mathrm{I})}[k]$ and $x_{s,\mathrm{D}}^{(\mathrm{I})}[k]$ are ICS-LoRa and down-chirp ICS-LoRa waveforms generated according to (58). Consequently, the SE of SSK-ICS-LoRa is $\eta^{(\text{SSK-ICS})} = (\mathrm{SF}+2)/M$ bit/s/Hz.

In another work based on ICS-LoRa, Shi et al. [75] introduce the enhanced ICS-LoRa (EICS-LoRa) by generating random interleavers for ICS-LoRa. As mentioned, the interleaved version of the CSS in ICS-LoRa consists of four segments. Based on EICS-LoRa, the transmission order of these four segments can be used to carry more information bits. Therefore, in this case, $4! = 24$ possible interleavers can be used. However, because of the increasing complexity and degradation of BER, the authors assumed a random 32 possible interleavers for an eight-segment CSS signal. Hence, the SE of this method at the best scenario is $\eta^{\mathrm{EICS}} = (\mathrm{SF}+5)/M$.

A. DISCUSSION

Table 5 includes the SE formula for all discussed data rate improvement methods. It should be noted that the parameters for each method are set in a way that an acceptable receiver complexity and BER performance can be achieved. Based on this, the FBI-LoRa scheme I provides the largest SE improvement compared to the conventional CSS modulation It should be noted that the parameter setting for Table 5 are selected based on the values of the original works for which the BER performance is near the conventional CSS modulation.

V. KEY ADVANCES IN INTERFERENCE MODELING

In this section, we review the existing key works in the literature corresponding to the performance of CSS modulation in the presence of interference [19], [20], [51], [81], [82], [83], [84], [85], [86] and investigate the proposed solutions.

Before proceeding with the literature review of CSS signal interference, we briefly present the interference model and discuss the BER performance of CSS modulation in the presence of the same SF interference. According to [87], whereas the signal-to-interference ratio (SIR) threshold for same-SF interference is 0 dB, interferers with different SF have an average rejection SIR threshold of −16 dB. Therefore, we assume that the CSS signal transmission is being performed in the presence of the same SF interference from another LoRa ED. Hence, equation (20) can be modified as:

$$r[k] = h x_s[k] + h_{\mathrm{Int}} x_{\mathrm{Int}}[k] + w[k], \tag{75}$$

where h_{Int} is the channel gain between the interferers and the LoRa gateway and $x_{\mathrm{Int}}[k]$ is the interfering signal. Also, due to the lack of complete synchronization between LoRa transmitters, we can assume that the interfering part is due to two different CSS symbols in such a way that:

$$x_{\mathrm{Int}}[k] = \begin{cases} x_{s_1}[k] & 0 \le k < \tau_{\mathrm{Int}} \\ x_{s_2}[k] & \tau_{\mathrm{Int}} \le k < M, \end{cases} \tag{76}$$

where τ_{Int} is the number of sample shift between two EDs. Based on this model, an approximate expression for the BER performance of CSS modulation under the same SF interference and AWGN channel condition is obtained in [19] as:

$$P_b^{(\mathrm{Int})} = 0.5 \times [P_{\mathrm{N}} + (1 - P_{\mathrm{N}}) P_{\mathrm{I}}], \tag{77}$$

where we have:

$$P_{\mathrm{N}} = \int_0^{\infty} \left\{1 - \left[1 - \exp\left(-\frac{\beta^2}{2\sigma^2}\right)\right]^{M-2}\right\} \times \frac{1}{\sqrt{2\pi\sigma^2}} \exp\left[-\frac{(\beta-1)^2}{2\sigma^2}\right] \mathrm{d}\beta, \tag{78}$$

and

$$P_{\mathrm{I}} \approx \frac{1}{M/2+1} \sum_{\tau_{\mathrm{Int}}=0}^{M/2} \left[\frac{1}{M} \sum_{z_1=0}^{M-1} \mathcal{Q}\left(\frac{1 - \mathcal{U}_0(\tau_{\mathrm{Int}}, z_1)}{\sqrt{2\sigma^2}}\right)\right], \tag{79}$$

TABLE 5. SE comparison of various CSS data improvement schemes.

Method	SE (bit/s/Hz)	Improvement percentage compared to CSS (for $\mathrm{SF}=8$)
Conventional CSS	$\frac{\mathrm{SF}}{M}$	–
ICS-LoRa [68]	$\frac{\mathrm{SF}+1}{M}$	112.5%
SSK-LoRa [25]	$\frac{\mathrm{SF}+1}{M}$	112.5%
IQ-CSS [41]	$\frac{2\mathrm{SF}}{M}$	200%
DCDSK [77]	$\frac{2\mathrm{SF}}{M}$	200%
DCRK-CSS [70]	$\frac{\mathrm{SF}+N_c}{M}$	125%
PSK-LoRa [69]	$\frac{\mathrm{SF}+N_p}{M}$	112.5% (for $N_p=1$) and 125% (for $N_p=2$)
FSCSS-IM [26]	$\frac{1}{M}\left\lfloor \log_2\binom{M}{W} \right\rfloor$	262.5% (for $W=3$)
IQCIM [42]	$\frac{2}{M}\left\lfloor \log_2\binom{M}{W} \right\rfloor$	525% (for $W=3$)
FBI-LoRa (I) [71]	$\frac{g_{\mathrm{num}}}{M}\left\lfloor \log_2\binom{N_g}{f_{\mathrm{num}}} \right\rfloor$	800% (for $g_{\mathrm{num}}=8$ and $f_{\mathrm{num}}=2$)
FBI-LoRa (II) [71]	$\frac{1}{M}\left(g'_{\mathrm{num}}\left\lfloor \log_2\binom{N_g}{f'_{\mathrm{num}}} \right\rfloor + \left\lfloor \log_2\binom{g_{\mathrm{num}}}{g'_{\mathrm{num}}} \right\rfloor\right)$	250% (for $g_{\mathrm{num}}=8$, $g'_{\mathrm{num}}=2$, and $f'_{\mathrm{num}}=2$)
ePSK-LoRa [72]	$\frac{1}{M}\left\lfloor \log_2\left(\frac{M}{N_{\mathrm{sub}}}\right)+N_{\mathrm{sub}}N_{\mathrm{PS}} \right\rfloor$	112.5% (for $N_{\mathrm{sub}}=2$ and $N_{\mathrm{PS}}=1$) and 137.5% (for $N_{\mathrm{sub}}=2$ and $N_{\mathrm{PS}}=2$)
GCSS [73]	$\frac{GN}{M}\log_2\left(\frac{M}{GN}\right)$	500% (for $GN=8$)
TDM-LoRa [43]	$\frac{2\mathrm{SF}}{M}$	200%
IQTDM-LoRa [43]	$\frac{4\mathrm{SF}}{M}$	400%
SSK-ICS-LoRa [74]	$\frac{\mathrm{SF}+2}{M}$	125%
EICS-LoRa [75]	$\frac{\mathrm{SF}+5}{M}$	162.5%

in which

$$\mathcal{U}_0(\tau_{\mathrm{Int}},z_1)=\frac{1}{M\sqrt{\gamma_{\mathrm{Int}}}}\left[M-\tau_{\mathrm{Int}}+\left|\frac{\sin(-\pi z_1\tau_{\mathrm{Int}}/M)}{\sin(-\pi z_1/M)}\right|\right], \tag{80}$$

where γ_{Int} is the SIR value.

Based on the numerical evaluation of equation (77) and computer simulations of the same SF interference model for CSS modulation with non-coherent detection, Figure 23 indicates the BER performance of the CSS modulation in such scenarios. As can be seen, compared to Figure 10, a nearly 1 to 2 dB degradation in performance can be observed.

The discussed interference model is based on Elshabrawy and Robert work in [19]. By means of the results provided in this work, it can be observed that in the presence of shadowing, the EDs experiencing the same SF interference can benefit from diversity resulting from shadowing to achieve a better performance compared to the ideal case of no shadowing in terms of coverage probability. Moreover, Afisiadis et al. in [51], extend the same SF interference model by assuming not only integer values of τ_{Int}, but also the fractional values which can be the case in practical situations. The SER and frame error rate (FER) expressions are also derived for this case.

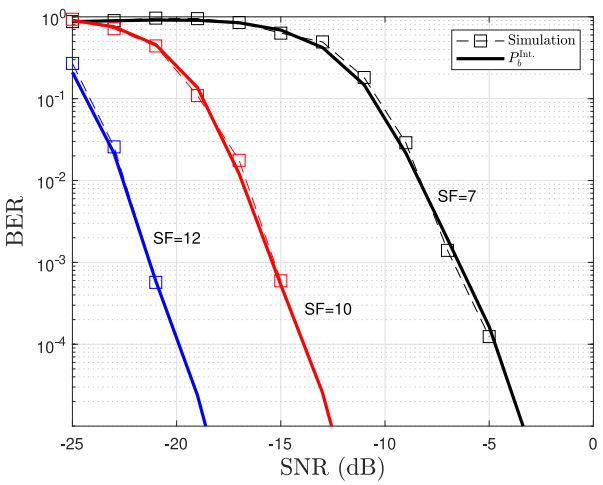

FIGURE 23. BER performance of the CSS modulation under same SF interference and AWGN channel for SF values of 7, 10, and 12 and SIR of $\gamma_{\mathrm{Int}}=6$ dB.

In [81], Edward et al. present another interference model similar to [19], with this difference that instead of CSS signals, the desired CSS signal is being interfered from two ICS-LoRa signals. The authors propose a simple receiver structure to retrieve both CSS and ICS-LoRa signals. Based on their proposed structure, at the receiver gateway, the

intended CSS signal is demodulated and detected using dechirping and DFT methods. To recover the interfering ICS-LoRa signals, the detected CSS signal is re-modulated and then subtracted from the combined received signal. However, to accurately eliminate the re-modulated CSS signal, a delay compensation process is necessary. The subtracted outcome is demodulated using the ICS-LoRa demodulation technique, which begins with the de-interleaver to convert the ICS-LoRa chirp signal back into the corresponding CSS chirp signal. Simulation results indicate that the BER performance is not almost affected in the presence of ICS-LoRa interference.

Edward et al. propose an enhanced receiver to detect superposed CSS signals [82]. This work deals with the case of receiving multiple CSS signals with the same SF in a gateway simultaneously with the aim of decoding these unsynchronized signals in the presence of frequency offset. In the proposed interference model, it is assumed that multiple LoRa frames each consisting of different CSS signals (generated according to LoRa specifications [88]) arrive at the GW taking into account the time desynchronization, and the frequency offset. There are three main steps toward decoding these superposed LoRa frames:

1) Detection of the strongest CSS signal.
2) Decoding the information embedded in the strongest CSS signal.
3) Regenerating the complex envelope of the strongest CSS signal and subtracting it from the received signal exploiting successive interference cancellation (SIC).

In the simulation section, the immunity of the proposed detection algorithm against the same SF interference has been proved. As a matter of fact, from the findings, it can be inferred that this receiver has the ability to successfully decode three overlapping signals with a SF $= 12$, as long as a minimum power ratio of 6 dB between the interfering CSS signals is maintained. Moreover, the authors provide experimental results to further validate the performance of their proposed receiver structure.

In [84], Garlisi et al. investigate the effect of the same SF interference in CSS-modulated LoRa frames and derive error rate expressions for SER and FER. The interference modeling is similar to [19], but the results are explored for coherent and non-coherent CSS detection. Based on the findings, it can be deduced that the performance difference between coherent and non-coherent detection in AWGN and no interference conditions is nearly 0.7 dB. On the other hand, this difference is shown to be around 10 dB when the SIR is 0 dB. According to this observation, dense LoRa networks with a high likelihood of same-SF packet collisions are a good fit for coherent CSS signal detection.

Afisiadis et al. present an analysis for CSS modulation error performance in the MPC along with the same SF interference [85]. Based on the proposed model for MPC, and assuming the receiver's perfect synchronization to the desired CSS signal, the effect of MPC at the receiver can be translated to the detection of a single CSS waveform in the presence of time-shifted versions of the same CSS signal and its previous one. This is also the case in the same SF interference model with some modification of the SIR value. The authors provide SER expressions for the MPC effect as well as two colliding CSS signals for both coherent and non-coherent detection schemes. Based on the provided results, the CSS signal appears to be less susceptible to the other lower path gains and just sensitive to the first path of the exponential decay channel. This makes it possible to estimate basic LoRa equalization schemes that just take into account a small number of channel pathways (or the strongest path gain). Moreover, it is shown that in the case of the same SF interference, the error performance is at its best when τ_{In} is around half of the CSS symbol interval.

A CSS receiver scheme is presented in [86] by Demeslay et al. In this work, to eliminate the effect of MPC, authors first investigate the performance of an ideal matched filter (MF) based on the MPC which depends on the transmitted CSS symbol. However, it is not practical because the CSS symbol is not known at the receiver. One way is to search over all possible CSS symbols and select the one that maximizes the DFT output of the MF which results in very high complexity. Therefore, the authors present fixed candidate MF in which they select N_{peak} highest peak values of M-point DFT of the received signal. But this requires a sorting algorithm which again results in high complexity. To deal with this issue, a variable candidate MF in which a threshold is used to select the candidates is proposed in which the search domain is generated from a list of the most probable candidate symbols. This threshold can be designed as a fraction of the maximum value of the M-point DFT output. Finally, by presenting the equivalent RAKE receiver model of the MF receiver, it is shown that the RAKE approach is by far preferred to MF in practice as its complexity outperforms MF in all cases.

A. KEY INSIGHTS

In this section, we investigated the recent key works regarding interference modeling and its effect in CSS-modulated LoRa networks. We can infer the following from the reviewed works:

- In the presence of the same SF CSS interference, the EDs benefit from the diversity created by the shadowing in the sense that they can achieve a better coverage probability than the case of having no shadowing effect [19].
- Co-existence of a network with CSS modulation and a network with ICS-LoRa is shown to have a mild effect on the BER performance of each network while exploiting SIC for joint detection. As a result, one can implement both techniques in the same region for multiple IoT applications [81].
- An SIC approach can also be used to detect three overlapping CSS signals with a minimum of 6 dB power difference between interfering parts. This type of receiver can be exploited in dense LoRaWAN networks

as it can deal with packet collision to some degree and increase the network capacity. Moreover, by being able to simultaneously decode multiple CSS signals, the burden of retransmission will be decreased resulting in EDs' lower battery consumption [82].

- The gap between coherent and non-coherent detection schemes in the presence of interference is notably larger than this gap for the case of having AWGN and no interference. Therefore, it is of more importance to investigate the semi-coherent detection techniques for CSS signal demodulation in the presence of interference [84].
- In the presence of interference due to MPC, CSS modulation is affected mostly by the first path of the channel with reduced performance degradation due to the other lower path gains. RAKE receiver in this channel condition results in the best error performance with the cost of high complexity. Therefore, it is recommended to implement a RAKE-based detector at the gateway. Moreover, the candidate-based RAKE can be used at the ED side of the network as it provides a performance close to the RAKE but in significantly lower complexity [85].

VI. KEY ADVANCES IN SYNCHRONIZATION ALGORITHMS

It is a known fact that in practice, any transmission technique experiences time and frequency offsets and CSS modulation is no exception. It is necessary to provide an accurate estimation scheme in the synchronization procedure to have a reliable signal recovery at the receiver end. The primary offsets to compensate for in the CSS receiver synchronization procedure are CFO and STO [58], [88]. The foundation of the synchronization algorithm for LoRa receiver is based on several features of up-chirp and down-chirp CSS signals which we discuss in detail in the following.

First, to see the effect of CFO and STO on a CSS signal at the receiver, let us assume that we have an ideal channel without noise and fading which only captures the effects of CFO and STO, i.e., $h = 1$ and $w(t) = 0$. Therefore we have:

$$r_s^{\text{off}}(t) = x_s(t+\tau) \times \exp(j2\pi t \Delta f_0), \tag{81}$$

where τ and Δf_0 represent STO and CFO, respectively. As shown in [58], the CFO and STO can be divided into integer and fractional parts, i.e., I_{CFO}, F_{CFO}, I_{STO}, and F_{STO}, respectively, as they introduce different effects on the received CSS signal. Based on this, we can define the followings [89]:

$$\Delta f_0 = \frac{\text{BW}}{M} \times (\text{I}_{\text{CFO}} + \text{F}_{\text{CFO}}), \tag{82}$$

$$\tau = \frac{\text{I}_{\text{STO}} + \text{F}_{\text{STO}}}{\text{BW}}. \tag{83}$$

To illustrate the effect of both integer and fractional parts of CFO and STO on the received CSS signal after dechirping and DFT, Figure 24 present the value of $|V_s^{\text{off}}[u]|$ as the amplitude of DFT output of the dechirped signal $r_s^{\text{off}}(t)$. Note that here we assume that SF = 9 and $s = 100$. As can be seen, compared to the case of having no CFO and STO, integer parts of CFO and STO shift the peak frequency bin originally located at the $s = 100$, while the fractional parts scatter the peak on several frequency bins.

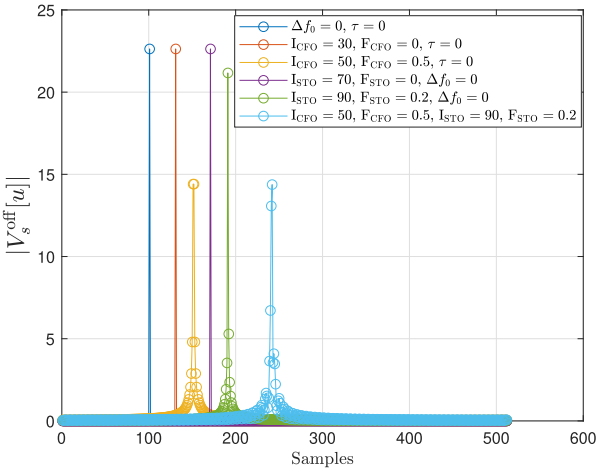

FIGURE 24. Effect of CFO and STO on CSS signals at the receiver side for SF = 9 and $s = 100$.

The LoRa frame is made of a sequence of CSS signals in a specific format including a part for synchronization purposes before the payload part as shown in Figure 25. As can be seen, the payload is preceded by multiple basic up-chirps as the preamble followed by two specific CSS signals as the sync word modulating s_{sync} (known to the receiver) and 2.25 basic down-chirps as the start frame delimiter (SFD). With the help of [58], [89], [90], we present the foundation for LoRa frame synchronization including the offset cancellation procedure. To this end, let us consider two consecutive basic up-chirps with unit amplitude ($A_0 = 1$) in the time duration of $[0, 2T_{\text{sym}}]$ as:

$$\tilde{x}_0(t) = e^{j2\pi \times \text{BW}\left[\frac{t^2}{2T_{\text{sym}}} - \frac{t}{2} - t \times U(t - T_{\text{sym}})\right]}. \tag{84}$$

After the transmission in channel conditions similar to (81), the received signal in time duration of $[0, T_{\text{sym}}]$ can be formulated as the product of a basic up-chirp, CFO, and STO effects as [89]

$$\begin{aligned}\tilde{r}(t) &= \tilde{x}_0(t+\tau) \times \exp(j2\pi t \Delta f_0) \\ &= x_0(t) \times \exp(j2\pi t \Delta f_0) \\ &\quad \times e^{j\left[2\pi \times \text{BW}\left(\frac{t\tau}{T_{\text{sym}}} - (t+\tau) \times U(t+\tau-T_{\text{sym}})\right) + \theta\right]},\end{aligned} \tag{85}$$

where θ denotes the constant phase contribution of the STO. Note that since it does not affect the non-coherent demodulation of the CSS signal, all constant phase offsets can be neglected in the LoRa synchronization process.

The received CSS signal $\tilde{r}(t)$ is sampled at $f_s = \text{BW}$ as discussed in **Remark 3**. Before performing synchronization, the receiver processes the samples of two consecutive

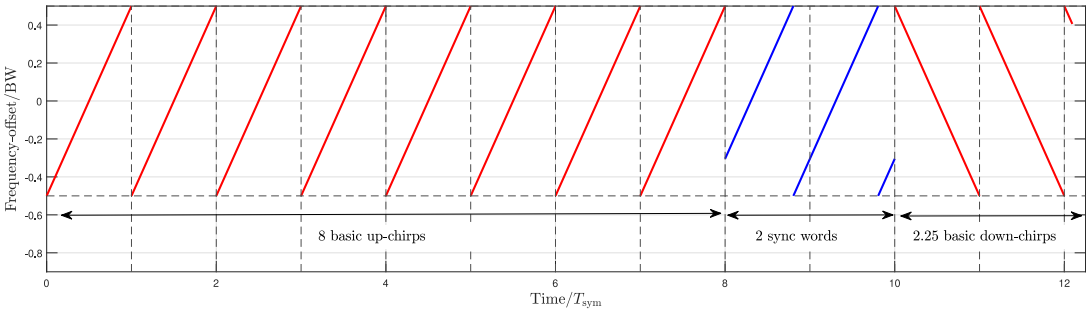

FIGURE 25. LoRa frame preamble format for SF = 8, BW = 125 kHz, and $s_{sync} = 50$.

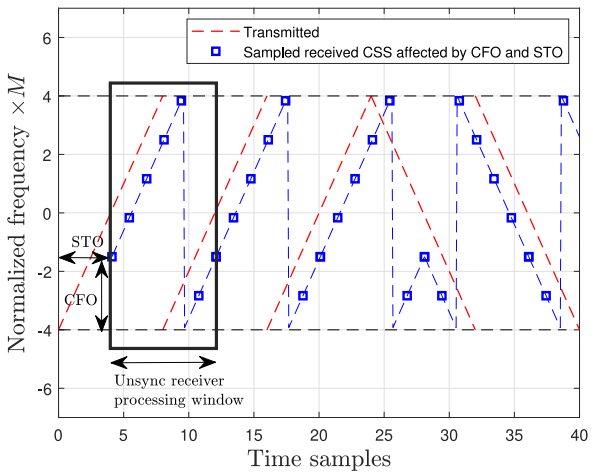

FIGURE 26. Receiver processing window after sampling and before synchronization for $M = 8$.

CSS symbols for which the first $N_{\text{off},1} = M - \lfloor \text{I}_{\text{STO}} + \text{F}_{\text{STO}} \rfloor$ samples belong to the first symbol, and the next $N_{\text{off},2} = \lfloor \text{I}_{\text{STO}} + \text{F}_{\text{STO}} \rfloor$ samples belong to the second symbol. To further illustrate this, Figure 26 is provided for three consecutive basic up-chirps and two consecutive basic down-chirps using $M = 8$. The offset is applied using the parameters $\text{I}_{\text{CFO}} = 2$, $\text{F}_{\text{CFO}} = 0.5$, $\text{I}_{\text{STO}} = 4$, and $\text{F}_{\text{STO}} = 0.1$.

As mathematically derived in [89], the received signal $\tilde{r(t)}$ after sampling and dechirping depends on all of the introduced offset elements as:

$$\tilde{r}^{(\text{dech.})}[k] = \exp\left(j2\pi k \frac{\text{I}_{\text{CFO}} + \text{F}_{\text{CFO}} + \text{I}_{\text{STO}}}{M}\right) \times < \exp\left(j2\pi k \frac{\text{F}_{\text{STO}}}{M}\right) >_{N_{\text{off},1}}, \quad (86)$$

where $< \Omega[k] >_{\kappa}$ represent a circular shift of κ samples on the signal $\Omega[k]$. By taking the M-point DFT of $\tilde{r}^{(\text{dech.})}[k]$, we obtain [89]:

$$\tilde{V}[u] = \left[M \frac{1 - e^{-j2\pi(\text{F}_{\text{CFO}}+\text{I}_{\text{CFO}}+\text{I}_{\text{STO}}-u)}}{1 - e^{-\frac{j2\pi}{M}(\text{F}_{\text{CFO}}+\text{I}_{\text{CFO}}+\text{I}_{\text{STO}}-u)}}\right] \circledast \left[e^{-j2\pi \frac{uN_{\text{off},1}}{M}} \frac{1 - e^{-j2\pi(\text{F}_{\text{STO}}-u)}}{1 - e^{-\frac{j2\pi}{M}(\text{F}_{\text{STO}}-u)}}\right], \quad (87)$$

where $\circledast$ is the circular convolution operator.

As mentioned before, the LoRa frame consists of multiple basic up-chirps followed by two basic down-chirps. All of the above derivations can be carried out for two consecutive basic down-chirps which results in the following sampled and dechirped CSS signal at the receiver [89]:

$$\tilde{r}_{\text{D}}^{(\text{dech.})}[k] = \exp\left(j2\pi k \frac{\text{I}_{\text{CFO}} + \text{F}_{\text{CFO}} - \text{I}_{\text{STO}}}{M}\right) \times < \exp\left(-j2\pi k \frac{\text{F}_{\text{STO}}}{M}\right) >_{N_{\text{off},1}}. \quad (88)$$

Similar to the up-chirp case, the M-point DFT operation on $\tilde{r}_{\text{D}}^{(\text{dech.})}[k]$ yields:

$$\tilde{V}_{\text{D}}[u] = \left[M \frac{1 - e^{-j2\pi(\text{F}_{\text{CFO}}+\text{I}_{\text{CFO}}-\text{I}_{\text{STO}}-u)}}{1 - e^{-\frac{j2\pi}{M}(\text{F}_{\text{CFO}}+\text{I}_{\text{CFO}}-\text{I}_{\text{STO}}-u)}}\right] \circledast \left[e^{-j2\pi \frac{uN_{\text{off},1}}{M}} \frac{1 - e^{-j2\pi(-\text{F}_{\text{STO}}-u)}}{1 - e^{-\frac{j2\pi}{M}(-\text{F}_{\text{STO}}-u)}}\right]. \quad (89)$$

A. LORA SYNCHRONIZATION ALGORITHM

Based on the presented equations, we summarize the LoRa frame synchronization algorithm in the following steps:

1) *Estimation of* F_{CFO}*:* As shown in [89], estimation of F_{CFO} can be performed independently of other offset elements. However, the estimation of I_{CFO}, I_{STO}, and F_{STO} are twined together. To estimate F_{CFO}, consider the received signal at the wth receiver processing window as $\tilde{r}_w[k]$. It has been shown that there is a relation between $\tilde{r}_{w-1}^{(\text{dech.})}[k]$ and $\tilde{r}_w^{(\text{dech.})}[k]$ for two consecutive basic up-chirps as follows [58], [89]:

$$\tilde{r}_w^{(\text{dech.})}[k] = \tilde{r}_{w-1}^{(\text{dech.})}[k] \times \exp(j2\pi \text{F}_{\text{CFO}}). \quad (90)$$

The same relation also exists between the M-point DFT outputs of the two signals because of the DFT linearity. Based on this, the estimate of F_{CFO} can be obtained as [58]:

$$\hat{\text{F}}_{\text{CFO}} = \frac{1}{2\pi} \angle \left[\sum_{w=2}^{N_{\text{P}}} \sum_{n_p=-2}^{2} \tilde{V}_{i+n_p}^{w}[u] \left(\tilde{V}_{i+n_p}^{w}[u]\right)^*\right] \quad (91)$$

where $i = arg\,max_u |\tilde{V}^w[u]|$ and $\angle(x)$ outputs the angle of x. Moreover, the inner DFT output product is calculated over N_{P} consecutive up-chirps and summation of the results is exploited for estimation of F_{CFO}.

2) *Estimation of* $\mathrm{I_{CFO}}$ *and* $\mathrm{I_{STO}}$*:* After the correction of $\mathrm{F_{CFO}}$, using equations (91) and (92), and also the non-coherent detection of CSS symbol in (36), we can write the following symbol detection for CSS up-chirp and down-chirp signals [58], [88], [89]:

$$\hat{s}_{\mathrm{up}} = \underset{u=0,1,\ldots,M-1}{\arg\max} \left|\tilde{V}[u]\right| = (\mathrm{I_{CFO}} + \mathrm{I_{STO}}) \mod M, \tag{92}$$

$$\hat{s}_{\mathrm{down}} = \underset{u=0,1,\ldots,M-1}{\arg\max} \left|\tilde{V}_{\mathrm{D}}[u]\right| = (\mathrm{I_{CFO}} - \mathrm{I_{STO}}) \mod M. \tag{93}$$

Therefore, the estimation of $\mathrm{I_{CFO}}$ can be obtained using an up-chirp and a down-chirp CSS signal as:

$$\hat{\mathrm{I}}_{\mathrm{CFO}} = \frac{1}{2}\mathcal{A}_M\big[(\hat{s}_{\mathrm{up}} + \hat{s}_{\mathrm{down}}) \mod M\big], \tag{94}$$

where $\mathcal{A}_M[k] = \begin{cases} k & \text{For } 0 \le k < M/2, \\ k - M & \text{For } M/2 \le k < M \end{cases}$.
Then, the estimation of $\mathrm{I_{STO}}$ can be simply obtained as:

$$\hat{\mathrm{I}}_{\mathrm{STO}} = (\hat{s}_{\mathrm{up}} - \hat{\mathrm{I}}_{\mathrm{CFO}}) \mod M. \tag{95}$$

3) *Estimation of* $\mathrm{F_{STO}}$*:* The estimation of $\mathrm{F_{STO}}$ is based on an intermediate function as follows [58], [89]:

$$T(\mathrm{F_{STO}}) = \frac{\left|\frac{1-e^{-j2\pi(\mathrm{F_{STO}}-1)}}{1-e^{-j2\frac{\pi}{M}(\mathrm{F_{STO}}-1)}}\right| - \left|\frac{1-e^{-j2\pi(\mathrm{F_{STO}}+1)}}{1-e^{-j2\frac{\pi}{M}(\mathrm{F_{STO}}+1)}}\right|}{\left|\frac{1-e^{-j2\pi(\mathrm{F_{STO}})}}{1-e^{-j2\frac{\pi}{M}(\mathrm{F_{STO}})}}\right|}. \tag{96}$$

Using the function $T(\mathrm{F_{STO}})$, the estimation can be performed as [58], [89]:

$$\hat{\mathrm{F}}_{\mathrm{STO}} = T^{-1}\left(\frac{|\hat{V}_{i+1}[u]| - |\hat{V}_{i-1}[u]|}{|\hat{V}_i[u]|}\right), \tag{97}$$

where $T^{-1}(.)$ is the inverse of the function $T(.)$. Note that averaging the magnitudes of $|\hat{V}[u]|$ over consecutive basic up-chirps improves the error performance of this estimator.

After becoming familiar with the practical synchronization procedure for LoRa communication, we investigate the literature corresponding to the improvement of LoRa synchronization [66], [89], [91], [92], [93], [94], [95], [96], [97] and discuss the provided solutions.

Seller and Sornin [91] investigate the BER performance of LoRa communication in mobile situations and develop a theoretical BER approximation using CFO. Experimental results show that higher SF values boost signal energy while also amplifying CFO interference, potentially reducing performance. Furthermore, proper estimation and remuneration of CFOs aid in increasing resilience to interference.

Kang et al. [66] propose a novel optimal detection algorithm for the preamble part of CSS modulation. Every frame is started with a preamble in many CSS modulation implementations, which is known a priori at the transceiver. The authors assume that N repetition of a specific CSS signal is adopted as the preamble according to LoRaWAN specification. The purpose of this work is to come up with the best preamble detection strategy for CSS modulation in terms of maximizing detection probability with the false alarm rate constraint. The optimization problem presented in this work is non-convex in general. As can be seen in Figure 18, the first branch corresponds to the general case when SF is not large and also the interference from other devices is correlated (the interference covariance matrix is not diagonal). The weighted average refers to calculating the mean sample of the received signal and left-multiplying it by the inverse of the interference covariance matrix. The rest of the operations are similar to the common CSS signal detection procedure explained in previous sections. For a special scenario of uncorrelated interference, the weighted averaging step reduces to only computing the sample mean of the received signal. However, since SF values in practice are large, the $M \times M$ interference covariance matrix has a large size making its inverse calculation very complex. To handle this issue, the authors propose a simplified version of their detection algorithm (third branch of Figure 18) which does not include the weighted averaging and dechirping steps. The proposed method is resulted from wide-sense stationary (WSS) random process assumption for the interference and can be accomplished using non-heavy and basic operations like FFT, addition, and multiplication, which reduces the computing complexity of preamble detection dramatically. This outcome is desirable in many real-world CSS-modulated IoT applications. Finally, by means of simulation, it has been shown that the proposed method outperforms the state-of-the-art techniques in terms of detection probability and complexity.

Bernier et al. in [58] state that the $\mathrm{F_{CFO}}$ can be estimated using the preamble part of the frame via a successive estimate averaging approach. Moreover, a low-complexity algorithm is also proposed for resolving the start of data block ambiguity. The authors suggest that after the estimation of $\mathrm{F_{CFO}}$, it becomes straightforward to calculate the expected number of down-chirp samples in a sequence of blocks suspected to contain SFD samples. These expected values are stored in a vector (vector 1). Additionally, another vector (vector 2) is created by extracting the FFT magnitude outputs at the index s_{sync} for each block. In high SNR scenarios, it is expected that this vector reflects the proportion of down-chirp samples in each block. Finally, by convolving Vector 1 with Vector 2, the maximum value of the convolution result can be used to determine the index of the block that contains the start of the data symbols.

In the work of Huang et al. [92], a novel approach is proposed to improve the performance of LoRa synchronization. Based on this scheme, called differential CSS (DCSS), another version of the CSS signal is transmitted which does not encode directly the value of the CSS symbols but rather their cumulative sum so that, at the receiver, they can be retrieved by differentiation. Using this feature, the SFD part is no longer needed. Simulation results show that DCSS

performs well in the presence of large CFO values while having a negligible impact on the receiver sensitivity.

Ben Temim et al. [93] propose a novel algorithm to compensate for the synchronization errors in CSS-modulated signals. Based on this approach, the time offset can be estimated using the difference of the received CSS signal cross-correlations with up-chirp and down-chirp, which are generated locally at the receiver side. This is achieved based on the fact that the cross-correlation peak can move to the left or right in the time axis in the presence of positive or negative CFO, respectively. Based on simulation results, it is shown that the proposed algorithm can recover time offset in SNRs lower than -6.35 dB while the signal experiences a CFO of 30 kHz.

Ghanaatian et al. in [89] suggest that $\mathrm{F_{CFO}}$ and $\mathrm{F_{STO}}$ have different and separable effects on the DFT output of the received CSS signal based on which $\mathrm{F_{CFO}}$ results in a linear continues phase term across CSS symbols, while $\mathrm{F_{STO}}$ introduces a phase term which is periodic with the period of M. Accordingly, the authors propose a synchronization algorithm in which the $\mathrm{F_{STO}}$ is estimated without the timing error parameter introduced in step 3 of Section VII-A. In fact, in the proposed algorithm, the preamble part is exploited to initially estimate and compensate $\mathrm{F_{STO}}$. Results show that the synchronization algorithm suggested in this work allows a receiver to achieve a target packet error rate of 10^{-3} with only a 1 or 2 dB increase in SNR compared to a receiver that is perfectly synchronized while introducing a negligible additional complexity.

In [94], Vangelista and Cattapan propose a CSS receiver design to cope with timing, frequency, and phase synchronization taking into account the transmitter pulse shaping and receiver matched-filter. Based on this design, the authors have developed simple first-order and second-order phase-locked loop (PLL) circuits with dynamic gain control. The outcome of this design is a practical non-coherent receiver that can be utilized in conventional LoRa/CSS systems. This receiver surpasses existing designs, either by providing enhanced performance or by decreasing computational complexity. Moreover, the proposed coherent version of the designed receiver enables PSK-LoRa efficient signal detection in which the phase of the DFT output containing the peak can reveal the PSK modulated bits after the phase loop is locked.

Nguyen and Nguyen in [95] present a low complexity synchronization algorithm for CSS signal receivers. It is demonstrated that the synchronization problem of time and frequency can be transformed into an optimization problem. However, the cost function associated with it is not concave. The proposed approach involves a thorough analysis of the cost function and relies on a rapid search for a nearly optimal estimate of the time delay, avoiding local optima. Subsequently, a search for the optimum within the vicinity of the initial estimate is performed. This approach significantly reduces the complexity compared to an exhaustive search. Also, the results indicate that the ML estimation performance is achieved, accompanied by reduced computation time, enabling real-time software implementation of synchronization on standard hardware.

Savaux et al. in [96] propose a LoRa packet synchronization algorithm with a focus on BER and packet reception rate (PRR) performance. The synchronization process of [96] can be summarized in four steps. First, a coarse symbol synchronization is performed to align the start of the packet with the detected symbols. Then, the first symbol of the preamble is identified by analyzing the number of up-chirps and down-chirps before and after the detected symbol. Afterward, an additional synchronization step corrects any constant frequency mismatch between the detector and the received packet by considering the symbol levels of the up-chirps and down-chirps. Finally, sub-sample synchronization methods are applied to further improve synchronization by making timing corrections smaller than a certain threshold, ensuring accurate data detection without energy distribution between adjacent frequency bins.

In the work [97], Ameloot et al. propose a two-user detection scheme for CSS transmission along with an interference-resistant synchronization algorithm. The authors present a three-stage synchronization algorithm utilizing the recurring up-chirps and the near-orthogonal correlation between the 2.25 down-chirps in the preamble of the second user and the modulated symbols of the first user. The first stage is to estimate $\hat{s}_{\mathrm{up}}$ and $\mathrm{F_{CFO}}$ using up-chirps. The second stage is to estimate $\hat{s}_{\mathrm{down}}$ and $\mathrm{F_{STO}}$ using down-chirps. In the final stage, i.e., preamble detection, the algorithm uses the obtained symbols $\hat{s}_{\mathrm{up}}$ and $\hat{s}_{\mathrm{down}}$ to estimate $\mathrm{I_{CFO}}$ and $\mathrm{I_{STO}}$. The results show that there is a performance gap of 2 dB between the ideal synchronization (which is not possible in practical situations) and the proposed algorithm of [97] at the SER of 10^{-3}.

B. KEY INSIGHTS

In this section, we discussed the synchronization procedure for a LoRa frame and reviewed the existing works in the literature. The following are the key insights regarding the problem of LoRa synchronization and the potential solutions:

- The complexity of recovering CSS signaling at the receiver, considering the current synchronization procedure performed in practice, is relatively high [58], [88].
- The start of data symbols can be found using a low-complexity algorithm based on FFT operations. With the synchronization algorithms proposed in [58], LoRaWAN designers have access to multiple tunable parameters to establish a trade-off between protocol overheads, power consumption, and link reliability and obtain a tailor-made design to their own IoT application [58].
- Transmission of DCSS instead of CSS can be helpful to improve synchronization performance despite having negligible added complexity. As shown in the results of [92], the application of DCSS can be extended to the system models with CFOs higher than the value

of BW/4, which is the maximum CFO estimable in conventional CSS transmission.
- Timing error parameter which introduces high complexity to CSS signaling synchronization can be removed from the procedure by replacing the algorithm introduced in [89] for estimation and compensation of τ_{Frac}. This helps to implement CSS receivers more efficiently and with lower complexity.
- Exploiting PLL circuits at the receiver results in better synchronization performance for CSS and PSK-LoRa signaling [94].

VII. FUTURE RESEARCH DIRECTIONS

Here in this section, we discuss some potential future research directions based on the provided foundation on CSS transmission techniques in the context of LoRaWAN-based IoT networks.

A. DOPPLER EFFECT ON CSS MODULATION

In the case of direct-to-satellite (DtS) communications, the Doppler shift is much larger than the terrestrial networks. This can result in significant performance degradations in exploiting CSS modulation in DtS-based IoT scenarios. In fact, the Doppler shift resulting from satellite movements can change the frequency bin of the detected CSS symbol with a similar effect as the Δf_0 shown in Figure 24. There are only a few studies that explore the Doppler effect of high-speed orbiting of LEO satellites on CSS modulation all of which are based on experimental results [59], [98], [99], [100]. However, there is no work that provides a detailed system model for CSS application in DtS scenarios considering all of the existing factors, i.e., Doppler shift, Doppler rate, ground-to-satellite fading channel, and path-loss and their effects on error performance of CSS modulation. Such work can shed light on role-player parameters such as BW and SF and their effects to achieve an analytical-based performance evaluation for CSS modulation in DtS scenarios. Moreover, all of these analyses can also be applied to SCS and FCrSK to verify their compatibility for use in satellite-based IoT networks.

B. CSS COEXISTENCE WITH WIFI, BLUETOOTH, AND LR-FHSS

Since different wireless technologies are widely used in IoT applications, there is a huge possibility of coexistence between different LPWAN technologies such as LoRa, WiFi, Bluetooth, and long-range frequency hopping spread spectrum (LR-FHSS). This coexistence can result in severe interference at the LoRa gateway which degrades the CSS signal detection performance. These communication schemes are used for a variety of IoT applications, including smart buildings, smart cities, industrial automation, and agriculture, to facilitate communication between devices and sensors. There are a couple of application notes provided by Semtech on the immunity of CSS modulation in the presence of WiFi and Bluetooth networks [101], [102]. Based on the results provided, for different WiFi modulations, i.e., differential quadrature phase shift keying (DQPSK), QPSK, and 64-quadrature amplitude modulation (64-QAM), CSS modulation has co-channel WiFi signal rejection of 6, 19, and 33 dB for lowest SF, respectively. This means that the existing LoRa receivers can demodulate the CSS signal if the power difference between the transmitted CSS signal and the existing WiFi signal is greater than 6, 19, and 33 dB for DQPSK, QPSK, and 64-QAM, respectively. There are similar results for different Bluetooth modulations, i.e., Gaussian frequency shift keying (GFSK), $\pi/4$-DQPSK, and 8-DPSK as 7, 11, and 10 dB co-channel Bluetooth signal rejection, respectively. Last but not least, the newly introduced LoRaWAN technology, i.e., LR-FHSS [12], [103], [104] exploits Gaussian minimum shift keying (GMSK) as its underlying modulation. In the case of LR-FHSS, since the frequency bands and channels can overlap with LoRa transmission, there is an even higher chance of experiencing interference between CSS and GMSK. Despite having these results provided by Semtech, there are no works in the literature to investigate the interference model between CSS and different WiFi, Bluetooth, and LR-FHSS modulations. Moreover, proper joint detectors can be designed based on an analytical system model to improve the tested co-channel rejection results.

C. CSS MULTI-USER INTERFERENCE

With the fast-paced growth of IoT network implementations, the scalability of LoRaWAN became a central focus in the research and industry communities. In current implementations, LoRaWAN exploiting CSS modulation uses ALOHA time scheduling and 1% duty cycle to prevent interference at the GW. However, receiving simultaneous CSS signals is still inevitable. To address this issue, more advanced signal processing schemes in the GW or the network server are still required with the help of which one can increase the network capacity of LoRaWAN. As an example, the work of [105] aims at increasing the LoRaWAN capacity by exploiting multiple antennas at the GW with a single-input multiple-output (SIMO) configuration. However, by observing the results, we can see that a desirable performance is achievable for a large number of receiver antennas, e.g., 50 or 60. To further improve the capacity while mitigating the imposed hardware cost on the network, one can investigate the use of the MIMO configuration instead of the SIMO in LoRa communication and its effect on the network capacity as it provides spatial diversity which helps improve the error performance in the presence of multi-user interference.

VIII. CONCLUSION

Considering the lack of a foundation work discussing all the aspects of the CSS modulation application in LoRaWAN and investigating the recent key advances in this field, this paper presents the basic mathematical foundation of CSS signaling in LoRaWAN networks, exploring various aspects such as signal generation, detection, and error performance.

Moreover, an overview of the existing key recent works in the literature is presented to extract some key insights and possible research potentials that can help to further improve this newly introduced technology, i.e., CSS modulation.

REFERENCES

[1] M. Vaezi et al., "Cellular, wide-area, and non-terrestrial IoT: A survey on 5G advances and the road toward 6G," *IEEE Commun. Surveys Tuts.*, vol. 24, no. 2, pp. 1117–1174, 2nd Quart., 2022.

[2] M. Jouhari, N. Saeed, M.-S. Alouini, and E. M. Amhoud, "A survey on scalable LoRaWAN for massive IoT: Recent advances, potentials, and challenges," *IEEE Commun. Surveys Tuts.*, vol. 25, no. 3, pp. 1841–1876, 3rd Quart., 2023.

[3] C. Milarokostas, D. Tsolkas, N. Passas, and L. Merakos, "A comprehensive study on LPWANs with a focus on the potential of LoRa/LoRaWAN systems," *IEEE Commun. Surveys Tuts.*, vol. 25, no. 1, pp. 825–867, 1st Quart., 2023.

[4] K. L. Lueth. "State of the IoT 2020: 12 billion IoT connections, surpassing non-IoT for the first time." 2020. Accessed: Nov. 2022. [Online]. Available: https://iot-analytics.com/state-of-the-iot-2020-12-billion-iotconnections-surpassing-non_iot-for-the-first-time/

[5] "Market research report." Accessed: Nov. 2022. [Online]. Available: https://www.fortunebusinessinsights.com/industry-reports/internetof-things-iot-market-100307

[6] "What are LoRa and LoRaWAN?" 2024. The Things Network. Accessed: Apr. 2024. [Online]. Available: https://www.thethingsnetwork.org/docs/lorawan/what-is-lorawan/

[7] L. Vangelista, "Frequency shift chirp modulation: The LoRa modulation," *IEEE Signal Process. Lett.*, vol. 24, no. 12, pp. 1818–1821, Dec. 2017.

[8] R. S. Sinha, Y. Wei, and S. Hwang, "A survey on LPWA technology: LoRa and NB-IoT," *ICT Exp.*, vol. 3, no. 1, pp. 14–21, Dec. 2017.

[9] Z. Sun, H. Yang, K. Liu, Z. Yin, Z. Li, and W. Xu, "Recent advances in LoRa: A comprehensive survey," *ACM Trans. Sens. Netw.*, vol. 18, no. 4, pp. 1–44, Nov. 2022.

[10] A. Pagano, D. Croce, I. Tinnirello, and G. Vitale, "A survey on LoRa for smart agriculture: Current trends and future perspectives," *IEEE Internet Things J.*, vol. 10, no. 4, pp. 3664–3679, Feb. 2023.

[11] Semtech Corp., "A technical overview of LoRa and LoRaWAN," LoRa Alliance Inc., San Ramon, CA, USA, Semtech Corp., Camarillo, CA, USA, White paper, 2015.

[12] N. Sornin, M. Luis, T. Eirich, T. Kramp, and O. Hersent, *RP2-1.0.2 LoRaWAN Regional Parameters*, LoRa Alliance Inc., San Ramon, CA, USA, 2020.

[13] F. Sforza, "Communication system," U.S. Patent 8 406 275 B2, Mar. 2013.

[14] C. Goursaud and J. M. Gorce, "Dedicated networks for IoT: PHY/MAC state of the art and challenges," *EAI Endors. Trans. Internet Things*, vol. 1, no. 1, pp. 1–11, 2015.

[15] B. Reynders, W. Meert, and S. Pollin, "Range and coexistence analysis of long range unlicensed communication," in *Proc. 23rd Int. Conf. Telecomm.*, 2016, pp. 1–6.

[16] B. Reynders and S. Pollin, "Chirp spread spectrum as a modulation technique for long range communication," in *Proc. Symp. Commun. Veh. Technol.*, 2016, pp. 1–5.

[17] G. Pasolini, "On the LoRa chirp spread spectrum modulation: Signal properties and their impact on transmitter and receiver architectures," *IEEE Trans. Wireless Commun.*, vol. 21, no. 1, pp. 357–369, Jan. 2022.

[18] M. Chiani and A. Elzanaty, "On the LoRa modulation for IoT: Waveform properties and spectral analysis," *IEEE Internet Things J.*, vol. 6, no. 5, pp. 8463–8470, Oct. 2019.

[19] T. Elshabrawy and J. Robert, "Analysis of BER and coverage performance of LoRa modulation under same spreading factor interference," in *Proc. IEEE Annu. Int. Symp. Pers., Indoor, Mobile Radio Commun. (PIMRC)*, 2018, pp. 1–6.

[20] F. Benkhelifa, Y. Bouazizi, and J. A. McCann, "How orthogonal is LoRa modulation?" *IEEE Internet Things J.*, vol. 9, no. 20, pp. 19928–19944, Oct. 2022.

[21] T. T. Nguyen, H. H. Nguyen, R. Barton, and P. Grossetete, "Efficient design of chirp spread spectrum modulation for low-power wide-area networks," *IEEE Internet Things J.*, vol. 6, no. 6, pp. 9503–9515, Dec. 2019.

[22] A. W. Azim, R. Shubair, and M. Chafii, "Chirp spread spectrum-based waveform design and detection mechanisms for LPWAN-based IoT—A survey," *IEEE Access*, vol. 12, pp. 24949–25017, 2024.

[23] A. J. Berni and W. D. Gregg, "On the utility of chirp modulation for digital signaling," *IEEE Trans. Commun.*, vol. COM-21, no. 6, pp. 748–751, Jun. 1973.

[24] D. S. Dayton, "FM "chirp" communications: Multiple access to dispersive channels," *IEEE Trans. Electromagn. Compat.*, vol. EMC-10, no. 2, pp. 296–297, Jun. 1968.

[25] M. Hanif and H. H. Nguyen, "Slope-shift keying LoRa-based modulation," *IEEE Internet Things J.*, vol. 8, no. 1, pp. 211–221, Jan. 2021.

[26] M. Hanif and H. H. Nguyen, "Frequency-shift chirp spread spectrum communications with index modulation," *IEEE Internet Things J.*, vol. 8, no. 24, pp. 17611–17621, Dec. 2021.

[27] J. R. Klauder, A. C. Price, S. Darlington, and W. J. Albersheim, "The theory and design of chirp radars," *Bell Syst. Tech. J.*, vol. 39, no. 4, pp. 745–808, Jul. 1960.

[28] E. C. Cook and M. Bernfeld, *Radar Signals: An Introduction to Theory and Application*. New York, NY, USA: Academic, 1967.

[29] A. Barna, "Pseudorandom frequency modulation in range-Doppler radar," *IEEE Trans. Aerosp. Electron. Syst.*, vol. AES-5, no. 2, pp. 221–229, Mar. 1969.

[30] G. F. Gott and J. P. Newsome, "H.F. data transmission using chirp signals," in *Proc. Inst. Electr. Eng.*, vol. 118, pp. 1162–1166, Sep. 1971.

[31] M. Kowatsch and J. Lafferl, "A spread-spectrum concept combining chirp modulation and pseudonoise coding," *IEEE Trans. Commun.*, vol. 31, no. 10, pp. 1133–1142, Oct. 1983.

[32] M. R. Winkler, "Chirp signals for communications," in *Proc. IEEE WESCON Conv. Rec.*, 1962, p. 14.2.1–14.2.4.

[33] E. K. Holliind-Moritz, J. C. Dute, and D. R. Brundage, "Swept frequency modulation," in *Proc. Nut. Electron. Conj.*, vol. 22, 1966, pp. 469–474.

[34] A. S. Griffiths and W. H. Smith, "FM chirp communication: An easily instrumented, multiple-access modulation format for dispersive channels," in *Proc. IEEE Int. Conf. Commun. Dig.*, 1967.

[35] G. W. Barnes, D. Hirst, and D. J. James, "Chirp modulation system in aeronautical satellites," in *AGARD Conf. Proc. No. 87 Avionics Spacecraf.*, 1971, pp. 30.1–30.10.

[36] J. Burnsweig and J. Wooldridge, "Ranging and data transmission using digital encoded FM-"chirp" surface acoustic wave filters," *IEEE Trans. Sonics Ultrason.*, vol. SU-20, no. 4, pp. 190–197, Apr. 1973.

[37] D. L. Zaytsev and V. I. Zhuravlev, "Noise immunity of a digital data transmission system using linearly frequency-modulated signals," *Telecohmunications*, vol. 22, no. 4, pp. 13–17, 1968.

[38] W. Hirt and S. Pasupathy, "Continuous phase chirp (CPC) signals for binary data communication—Part II: Noncoherent detection," *IEEE Trans. Commun.*, vol. COM-29, no. 6, pp. 836–858, Jun. 1981.

[39] R. C. Dixon, *Spread Spectrum Systems*. New York, NY, USA: Wiley, 1976.

[40] "AN1200.22: LoRa modulation basics," SemTech Corp., Camarillo, CA, USA, Application Note, May 2015.

[41] I. B. F. de Almeida, M. Chafii, A. Nimr, and G. Fettweis, "In-phase and quadrature chirp spread spectrum for IoT communications," in *Proc. IEEE Glob. Telecommun. Conf.*, 2020, pp. 1–6.

[42] G. Baruffa and L. Rugini, "Performance of LoRa-based schemes and quadrature chirp index modulation," *IEEE Internet Things J.*, vol. 9, no. 10, pp. 7759–7772, May 2022.

[43] S. An, H. Wang, Y. Sun, Z. Lu, and Q. Yu, "Time domain multiplexed LoRa modulation waveform design for IoT communication," *IEEE Commun. Lett.*, vol. 26, no. 4, pp. 838–842, Apr. 2022.

[44] "Low power long range transmitter," U.S. Patent EP2 763 321 A1, 2020. Accessed: Sep. 2022. [Online]. Available: https://patents.google.com/patent/EP2763321A1

[45] "Communications system," U.S. Patent EP2 449 690 B1, 2020. Accessed: Jun. 2021. [Online]. Available: https://patents.google.com/patent/EP2449690B1/en

[46] G. Proakis and M. Salehi, *Digital Communications 5th Edition*. New York, NY, USA: McGraw Hill, 2007.

[47] G. Ferre and A. Giremus, "LoRa physical layer principle and performance analysis," in *Proc. IEEE Int. Conf. Electron. Circuits Syst. (ICECS)*, 2018, pp. 65–68.

[48] T. Elshabrawy and J. Robert, "Closed-form approximation of LoRa modulation BER performance," *IEEE Commun. Lett.*, vol. 22, no. 9, pp. 1778–1781, Sep. 2018.

[49] A. Marquet, N. Montavont, and G. Z. Papadopoulos, "Investigating theoretical performance and demodulation techniques for LoRa," in *Proc. 20th Int. Symp. "World Wireless, Mobile Multimedia Netw," (WoWMoM)*, 2019, pp. 1–6.

[50] H. Mroue, A. Nasser, B. Parrein, S. Hamrioui, E. Mona-Cruz, and G. Rouyer, "Analytical and simulation study for LoRa modulation," in *Proc. Int. Conf. Telecommun. (ICT)*, 2018, pp. 655–659.

[51] O. Afisiadis, M. Cotting, A. Burg, and A. Balatsoukas-Stimming, "On the error rate of the LoRa modulation with interference," *IEEE Trans. Wireless Commun.*, vol. 19, no. 2, pp. 1292–1304, Feb. 2020.

[52] T. K. Nguyen, H. H. Nguyen, and E. Bedeer, "Performance improvement of LoRa modulation with signal combining and semi-coherent detection," *IEEE Commun. Lett.*, vol. 25, no. 9, pp. 2889–2893, Sep. 2021.

[53] I. S. Gradshteyn and I. M. Ryzhik, *Table of Integrals, Series, and Products*, 8th ed. Amsterdam, The Netherlands: Academic, 2014.

[54] "Electromagnetic compatibility and radio spectrum matters (ERM); short range devices (SRD); radio equipment to be used in the 25 MHz to 1000 MHz frequency range with power levels ranging up to 500 mW; part 1: Technical characteristics and test methods," Eur. Telecommun. Stand. Inst., Sophia Antipolis, France, Rep. ETSI EN 300 220–1 V2.4.1, 2012.

[55] T. Elshabrawy and J. Robert, "Evaluation of the BER performance of LoRa communication using BICM decoding," in *Proc. IEEE 9th Int. Conf. Consum. Electron.*, 2019, pp. 162–167.

[56] "AN1200.13: SX1272/3/6/7/8: LoRa modem designer's guide," SemTech, Camarillo, CA, USA, Jul. 2013.

[57] O. Georgiou and U. Raza, "Low power wide area network analysis: Can LoRa scale?" *IEEE Wireless Commun. Lett.*, vol. 6, no. 2, pp. 162–165, Apr. 2017.

[58] C. Bernier, F. Dehmas, and N. Deparis, "Low complexity LoRa frame synchronization for ultra-low power software-defined radios," *IEEE Trans. Commun.*, vol. 68, no. 5, pp. 3140–3152, May 2020.

[59] A. A. Doroshkin, A. M. Zadorozhny, O. N. Kus, V. Y. Prokopyev, and Y. M. Prokopyev, "Experimental study of LoRa modulation immunity to Doppler effect in CubeSat radio communications," *IEEE Access*, vol. 7, pp. 75721–75731, 2019.

[60] Y. Qian, L. Ma, and X. Liang, "Symmetry chirp spread spectrum modulation used in LEO satellite Internet of Things," *IEEE Commun. Lett.*, vol. 22, no. 11, pp. 2230–2233, Nov. 2018.

[61] Y. Qian, L. Ma, and X. Liang, "The performance of chirp signal used in LEO satellite Internet of Things," *IEEE Commun. Lett.*, vol. 23, no. 8, pp. 1319–1322, Aug. 2019.

[62] A. Roy, H. B. Nemade, and R. Bhattacharjee, "Symmetry chirp modulation waveform design for LEO satellite IoT communication," *IEEE Commun. Lett.*, vol. 23, no. 10, pp. 1836–1839, Oct. 2019.

[63] C. Yang, M. Wang, L. Zheng, and G. Zhou, "Folded chirp-rate shift keying modulation for LEO satellite IoT," *IEEE Access*, vol. 7, pp. 99451–99461, 2019.

[64] H. Ma, G. Cai, Y. Fang, P. Chen, and G. Han, "Design and performance analysis of a new STBC-MIMO LoRa system," *IEEE Trans. Commun.*, vol. 69, no. 9, pp. 5744–5757, Sep. 2021.

[65] J.-M. Kang, "MIMO-LoRa for high-data-rate IoT: Concept and precoding design," *IEEE Internet Things J.*, vol. 9, no. 12, pp. 10368–10369, Jan. 2022.

[66] J.-M. Kang, D.-W. Lim, and K.-M. Kang, "On the LoRa modulation for IoT: Optimal preamble detection and its performance analysis," *IEEE Internet Things J.*, vol. 9, no. 7, pp. 4973–4986, Apr. 2022.

[67] J.-M. Kang and K. W. Choi, "Efficient demodulation algorithms for MIMO-LoRa," *IEEE Internet Things J.*, vol. 10, no. 23, pp. 21129–21130, Dec. 2023.

[68] T. Elshabrawy and J. Robert, "Interleaved chirp spreading LoRa-based modulation," *IEEE Internet Things J.*, vol. 6, no. 2, pp. 3855–3863, Apr. 2019.

[69] R. Bomfin, M. Chafii, and G. Fettweis, "A novel modulation for IoT: PSK-LoRa," in *Proc. IEEE Veh. Technol. Conf.*, 2019, pp. 1–5.

[70] I. Bizon Franco de Almeida, M. Chafii, A. Nimr, and G. Fettweis, "Alternative chirp spread spectrum techniques for LPWANs," *IEEE Trans. Green Commun. Netw.*, vol. 5, no. 4, pp. 1846–1855, Dec. 2021.

[71] H. Ma, Y. Fang, G. Cai, G. Han, and Y. Li, "A new frequency-bin-index LoRa system for high-data-rate transmission: Design and performance analysis," *IEEE Internet Things J.*, vol. 9, no. 14, pp. 12515–12528, Jul. 2022.

[72] A. W. Azim, J. L. G. Monsalve, and M. Chafii, "Enhanced PSK-LoRa," *IEEE Wireless Commun. Lett.*, vol. 11, no. 3, pp. 612–616, Mar. 2022.

[73] Q. Yu, H. Wang, Z. Lu, and S. An, "Group-based CSS modulation: A novel enhancement to LoRa physical layer," *IEEE Wireless Commun. Lett.*, vol. 11, no. 3, pp. 660–664, Mar. 2022.

[74] A. Mondal, M. Hanif, and H. H. Nguyen, "SSK-ICS LoRa: A LoRa-based modulation scheme with constant envelope and enhanced data rate," *IEEE Commun. Lett.*, vol. 26, no. 5, pp. 1185–1189, May 2022.

[75] Y. Shi, W. Xu, and L. Wang, "An enhanced interleaved chirp spreading LoRa modulation scheme for high data transmission," in *Proc. Wireless Telecommun. Symp.*, 2022, pp. 1–6.

[76] J. Liu, Y. Yan, P. Huang, B. Ma, and H. Yu, "Block interleaved chirp spreading LoRa modulation over multipath channels," *IEEE Trans. Veh. Technol.*, vol. 73, no. 7, pp. 10840–10844, Jul. 2024.

[77] G. Xie, Q. Liang, R. Li, and D. Li, "Dual chirps direction shift keying modulation," *IEEE Wireless Commun. Lett.*, vol. 13, no. 6, pp. 1735–1739, Jun. 2024.

[78] N. Ishikawa, S. Sugiura, and L. Hanzo, "50 years of permutation, spatial, and index modulation: From classic RF to visible light communications and data storage," *IEEE Commun. Surveys Tuts.*, vol. 20, no. 3, pp. 1905–1938, 3rd Quart., 2018.

[79] P. Zhang and H. Liu, "An ultra-wide band system with chirp spread spectrum transmission technique," in *Proc. Int. Conf. ITS Telecommun.*, 2006, pp. 294–297.

[80] T. Yoon, S. Ahn, S. Y. Kim, and S. Yoon, "Performance analysis of an overlap-based CSS system," in *Proc. Int. Conf. Adv. Commun. Technol.*, vol. 1, 2008, pp. 424–426.

[81] E. Başar, Ü. Aygölü, E. Panayırcı, and H. V. Poor, "Orthogonal frequency division multiplexing with index modulation," *IEEE Trans. Signal Process.*, vol. 61, no. 22, pp. 5536–5549, Nov. 2013.

[82] P. Edward, S. Elzeiny, M. Ashour, and T. Elshabrawy, "On the coexistence of LoRa- and interleaved chirp spreading LoRa-based modulations," in *Proc. Int. Conf. Wireless Mobile Comput. Netw. Commun. (WiMob)*, 2019, pp. 1–6.

[83] M. A. Ben Temim, G. Ferré, B. Laporte-Fauret, D. Dallet, B. Minger, and L. Fuché, "An enhanced receiver to decode superposed LoRa-like signals," *IEEE Internet Things J.*, vol. 7, no. 8, pp. 7419–7431, Aug. 2020.

[84] D. Garlisi, S. Mangione, F. Giuliano, D. Croce, G. Garbo, and I. Tinnirello, "Interference cancellation for LoRa gateways and impact on network capacity," *IEEE Access*, vol. 9, pp. 128133–128146, 2021.

[85] O. Afisiadis, S. Li, J. Tapparel, A. Burg, and A. Balatsoukas-Stimming, "On the advantage of coherent LoRa detection in the presence of interference," *IEEE Internet Things J.*, vol. 8, no. 14, pp. 11581–11593, Jul. 2021.

[86] C. Demeslay, P. Rostaing, and R. Gautier, "Theoretical performance of LoRa system in multipath and interference channels," *IEEE Internet Things J.*, vol. 9, no. 9, pp. 6830–6843, May 2022.

[87] C. Demeslay, P. Rostaing, and R. Gautier, "Simple and efficient LoRa receiver scheme for multipath channel," *IEEE Internet Things J.*, vol. 9, no. 17, pp. 15771–15785, Sep. 2022.

[88] D. Croce, M. Gucciardo, S. Mangione, G. Santaromita, and I. Tinnirello, "Impact of LoRa imperfect orthogonality: Analysis of link-level performance," *IEEE Commun. Lett.*, vol. 22, no. 4, pp. 796–799, Apr. 2018.

[89] R. Ghanaatian, O. Afisiadis, M. Cotting, and A. Burg, "LoRa digital receiver analysis and implementation," in *Proc. IEEE Int. Conf. Acoust., Speech, Signal Process.*, 2019, pp. 1498–1502.

[90] M. Xhonneux, O. Afisiadis, D. Bol, and J. Louveaux, "A low-complexity LoRa synchronization algorithm robust to sampling time offsets," *IEEE Internet Things J.*, vol. 9, no. 5, pp. 3756–3769, Mar. 2022.

[91] O. Seller and N. Sornin, "Low complexity, low power and long range radio receiver," Eur. Patent 3 264 622, Jul. 2016.

[92] P. Huang, J. Liu, and B. Ma, "Approximate BER performance of LoRa communication under carrier frequency offset," *IEEE Internet Things J.*, vol. 11, no. 15, pp. 26001–26004, Aug. 2024.

[93] M. A. Ben Temim, G. Ferré and R. Tajan, "A novel approach to enhance the robustness of LoRa-like PHY layer to synchronization errors," in *Proc. IEEE Glob. Telecommun. Conf.*, 2020, pp. 1–6.
[94] L. Vangelista and A. Cattapan, "Start of packet detection and Synchronization for LoRaWAN modulated signals," *IEEE Trans. Wireless Commun.*, vol. 21, no. 6, pp. 4608–4621, Jun. 2022.
[95] T. T. Nguyen and H. H. Nguyen, "Design of noncoherent and coherent receivers for chirp spread spectrum systems," *IEEE Internet Things J.*, vol. 9, no. 20, pp. 19988–20002, Oct. 2022.
[96] V. Savaux, C. Delacourt, and P. Savelli, "On time-frequency synchronization in LoRa system: From analysis to near-optimal algorithm," *IEEE Internet Things J.*, vol. 9, no. 12, pp. 10200–10211, Jun. 2022.
[97] T. Ameloot, H. Rogier, M. Moeneclaey, and P. Van Torre, "LoRa signal synchronization and detection at extremely low signal-to-noise ratios," *IEEE Internet Things J.*, vol. 9, no. 11, pp. 8869–8882, Jun. 2022.
[98] M. Xhonneux, J. Tapparel, A. Balatsoukas-Stimming, A. Burg, and O. Afisiadis, "A maximum-likelihood-based two-user receiver for LoRa chirp spread-spectrum modulation," *IEEE Internet Things J.*, vol. 9, no. 22, pp. 22993–23007, Nov. 2022.
[99] A. Doroshkin, A. Zadorozhny, O. Kus, V. Prokopyev, and Y. Prokopyev, "Laboratory testing of LoRa modulation for CubeSat radio communications," in *Proc. MATEC Web Conf.*, vol. 158, 2018, p. 1008.
[100] A. M. Zadorozhny et al., "First flight-testing of LoRa modulation in satellite radio communications in low-earth orbit," *IEEE Access*, vol. 10, pp. 100006–100023, 2022.
[101] M. Asad Ullah, G. Pasolini, K. Mikhaylov, and H. Alves, "Understanding the limits of LoRa direct-to-satellite: The Doppler perspectives," *IEEE Open J. Commun. Soc.*, vol. 5, pp. 51–63, 2024.
[102] *AN1200.30: WiFi Immunity of LoRa® at 2.4 GHz*, SemTech Corp., Camarillo, CA, USA, Jun. 2017.
[103] *AN1200.40: Bluetooth Immunity of LoRa® at 2.4 GHz*, SemTech Corp., Camarillo, CA, USA, Apr. 2018.
[104] G. Boquet, P. Tuset-Peiro, F. Adelantado, T. Watteyne, and X. Vilajosana, "LR-FHSS: Overview and performance analysis," *IEEE Commun. Mag.*, vol. 59, no. 3, pp. 30–36, Mar. 2021.
[105] A. Maleki, H. H. Nguyen, and R. Barton, "Outage probability analysis of LR-FHSS in satellite IoT networks," *IEEE Commun. Lett.*, vol. 27, no. 3, pp. 946–950, Mar. 2023.
[106] T. K. Nguyen, H. H. Nguyen, and E. Bedeer, "Concurrent transmission and multiuser detection of LoRa signals," *IEEE Internet Things J.*, vol. 10, no. 1, pp. 774–786, Jan. 2023.

ALIREZA MALEKI received the B.Sc. and M.Sc. degrees in communication systems from the K. N. Toosi University of Technology, Tehran, Iran, in 2013 and 2017, respectively. He is currently pursuing the Ph.D. degree in electrical engineering (telecommunication systems) with the University of Saskatchewan, Saskatoon, SK, Canada. His research is focused on IoT transmission techniques, LoRaWAN MAC, and PHY protocols.

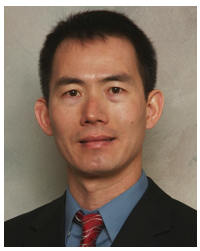

HA H. NGUYEN received the bachelor's degree in electrical engineering from the Hanoi University of Technology, Hanoi, Vietnam, in 1995, the master's degree in electrical engineering from the Asian Institute of Technology, Bangkok, Thailand, in 1997, and the Ph.D. degree in electrical engineering from the University of Manitoba, Winnipeg, MB, Canada, in 2001.

He joined the Department of Electrical and Computer Engineering, University of Saskatchewan, Saskatoon, SK, Canada, in 2001, and became a Full Professor in 2007. He held the position of NSERC/Cisco Industrial Research Chair in Low-Power Wireless Access for Sensor Networks. He was a coauthor, with Ed Shwedyk, of the textbook *A First Course in Digital Communications* (Cambridge University Press). His research interests spanned broad areas of communication theory, wireless communications, and statistical signal processing.

Dr. Nguyen was an Associate Editor of the IEEE TRANSACTIONS ON WIRELESS COMMUNICATIONS, the IEEE TRANSACTIONS ON COMMUNICATIONS, the IEEE TRANSACTIONS ON VEHICULAR TECHNOLOGY, and IEEE WIRELESS COMMUNICATIONS LETTERS. He served as a Technical Program Chair for numerous IEEE events and was the General Chair for the 30th Biennial Symposium on Communications 2021. He was a Fellow of the Engineering Institute of Canada and a Registered Member of the Association of Professional Engineers and Geoscientists of Saskatchewan.

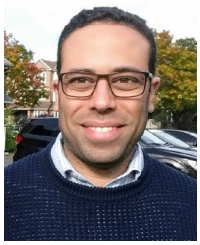

EBRAHIM BEDEER (Member, IEEE) received the B.Sc. (Hons.) and M.Sc. degrees in electrical engineering from Tanta University, Tanta, Egypt, in 2002 and 2008, respectively, and the Ph.D. degree in electrical engineering from Memorial University, St. Johns, NL, Canada, in 2014.

He joined as an Assistant Professor with the Department of Electrical and Computer Engineering, University of Saskatchewan, Saskatoon, SK, Canada, in 2019. Before that, he was an Assistant Professor (Lecturer) with Ulster University, Coleraine, U.K., and a Postdoctoral Fellow with Carleton University, Ottawa, ON, Canada, and the University of British Columbia, Kelowna, BC, Canada. His research interests span broad areas of communication theory, wireless communications, and statistical signal processing. He is a Registered Member of the Association of Professional Engineers and Geoscientists of Saskatchewan.

ROBERT BARTON received the graduation degree in engineering physics from The University of British Columbia, Vancouver, BC, Canada, in 1997.

He is the CTO of Cisco Canada, Vancouver, and also holds the role of the Distinguished Engineer. He is an accomplished author with books published on the subjects of quality of service, wireless communications, and Internet of Things. He has also coauthored peer-reviewed academic papers and leads Cisco's academic research partnership program. He holds numerous patents in the areas of wireless communications, network security, cloud networking, IoT, and machine learning. His current areas of work include all manner of wireless communications, IT/OT convergence, network automation, and AI/ML in networking systems.